# Numerical investigation of microstructure effects on the mechanical behaviour of coarse grained granular assemblies with respect to particle breakage

**PROJECT REPORT**

OMFB-00226/2010, AT-11/09

01 April 2010 – 30 Sept 2012

**Imre Laufer – Katalin Bagi**
Budapest University of Technology and Economics
**Erich Bauer**
Graz University of Technology

# CONTENT

Imre Laufer – Katalin Bagi
Budapest University of Technology and Economics
Erich Bauer
Graz University of Technology

## Summary

Crushing of mineral grains is a complex phenomenon encountered in many fields of engineering. It is influenced by effects on many levels: macroscopic stress state and void ratio; distribution of contact forces in the grain matrix on the meso-level, affected by grain size distribution and grain shape; the stress field inside the particles and their crushing strength on the micro-level. In turn, grain crushing leads to the evolution of the particle size distribution and leads to rearrangement of the grains. The Discrete Element Method offers new perspectives in modelling grain crushing. This report presents a model with macrograins consisting of randomly placed smaller micrograins. Single grain crushing tests are preformed to characterize the crushing strength of individual particles, and a parameter analysis is conducted to evaluate the effects of the most important model parameters. Then simulated high-pressure oedometer tests are carried out investigate the response of the assembly, especially the evolution of grain breakage and the connection between the macroscopic stress and void ratio.

# 1 Introduction

## 1.1 Overview of grain crushing

The crushing of mineral grains is a complex phenomenon, encountered in many fields of engineering. To list a few: in material processing, the aim is mainly the comminution of larger grains to produce e.g. finer aggregates, cement, etc. In geotechnical engineering, it may be responsible for settlements and the reduction of shear resistance by suppressing dilatancy (e.g. under foundations or in railway track ballast), and measures are taken to prevent it. In petroleum engineering, it may cause densification and consequently the reduction of reservoir permeability. In this paper, the grain crushing will be examined from the geotechnical engineers' point of view, through the behaviour in one-dimensional, oedometric compression tests.

Since grain crushing has many different aspects, it has been studied by a large number of researchers, from many different points of view. (Nakata, Kato, Hyodo, Hyde, & Murata, 2001) give an overview of the main influence factors on grain crushing, as a result of thorough laboratory investigations on sands. According to them, grain crushing in one-dimensional compression – often also termed yielding – is affected by:

- particle size and particle size distribution
- particle shape and angularity
- mineral composition and particle strength
- initial void ratio

The complexity of the problem lies in the interaction of these aspects, as will be outlined below.

It was shown e.g. by (Chuhan, Kjeldstad, Bjørlykke, & Høeg, 2002) and (Guimaraes, Valdes, Palomino, & Santamarina, 2007) that the mineral composition strongly influences the grain's strength against crushing, as well as the shape and type of fragments: if a grain contains crystals or inclusions with different stiffnesses, then these may lead to stress concentration, and their boundaries represent

inner flaws for crack initiation. This implies that fracture mechanical approaches could be justified for this level. A few steps have already been taken into this direction, e.g. (Silvani, Bonelli, & Désoyer, 2007) , (McDowell & Bolton, 1998) and (Oldecop & Alonso, 2007). Furthermore, time-dependent processes, such as weathering and stress corrosion are also at play at this level.

To calculate the internal stresses inside the grain is quite difficult: it is known that the grain shape influences the stress field (Nakata, Kato, Hyodo, Hyde, & Murata, 2001), (McDowell, Bolton, & Robertson, 1996). Usually, if the grains are not too elongated, the simplification as a sphere can be justified, and the corresponding analytical solutions may be applied. Such methods are presented e.g. in (Gundepudi, Sankar, Mecholsky, & Clupper, 1997), (Chau, Wei, Wong, & Yu, 2000),H (Russell, Wood, & Kikumoto, 2009), and (Russell & Wood, 2009). However, these methods also need some material properties, mainly Young's modulus and Poisson's ratio as input, and are very often sensitive to these values. A more precise analysis of the internal stresses may be achieved by the finite element method (FEM) for the grains, but requires substantially more computational effort.

After the stress calculation, a failure criterion must be defined for the grains. Usually, the crushing strength is expressed in stress units, back-calculated from a simplified force-stress-relation given in Eq. (1). This approach will be presented below; however it neglects the effect of coordination number (as shown by (Gundepudi, Sankar, Mecholsky, & Clupper, 1997)), which has to be incorporated separately. Furthermore, the crushing strength of real grains was shown to be a probabilistic value and also shows a size effect. (McDowell & Bolton, 1998), (Nakata, Hyde, Hyodo, & Murata, 1999). Nevertheless, if the probabilistic nature of grain strength, the effect of multiple forces and the size effects are addressed, and assigned strength is consistent with the stress calculation method, the resulting failure criterion may be suitable for modelling grain breakage under complex conditions. To sum up the two opposite tendencies, larger grains exhibit a lower strength, but since their coordination number is usually higher – on the other hand, smaller grains are stronger, but their loading conditions facilitates breakage. The situation gets even more complicated if reversals occur: (Uygar & Doven, 2006) presented test result from cyclic triaxial tests on sand. They inferred that contact forces accumulate during load cycles even at lower stress levels.

If a suitable failure criterion is set up, the forces acting on the grains have to be determined. It is well known that the forces in granular assemblies are transferred through so-called force chains, where some grains carry large contact forces, whereas others – even in close vicinity – may even be completely unloaded. Based on DEM simulations, (Marketos & Bolton, 2007) have shown that the distribution of contact forces related to the mean contact force is independent of the macroscopic stress level, and they observed a linearly increasing tendency for the contact force magnitudes with grain diameter, consistent with other researchers' results. This implies that larger grains form the main skeleton for the force chains, and experience higher contact forces, but also carry more contacts than smaller grains. The ratio of "active" and "passive" grains was shown to depend on the range of void ratios $e_{max}$-$e_{min}$ (Nakata, Kato, Hyodo, Hyde, & Murata, 2001), a property related to the grain size distribution and to particle shape. The initial void ratio also plays a significant role, since at higher void ratios the same macroscopic stress is carried by fewer grains, leading to higher contact forces.

As fragments are produced during grain breakage, the grain size distribution evolves, and it was found by many researchers that the finer fractions increase at the fastest rate (Chuhan, Kjeldstad, Bjørlykke, & Høeg, 2002). (Nakata, Hyodo, Hyde, Kato, & Murata, 2001) also found that different

initial curves approach a common limiting grading curve, where no crushing occurs anymore. (McDowell, Bolton, & Robertson, 1996) and (McDowell & Bolton, 1998) suggested that the evolution shifts the grading curve towards a self-similar, fractal distribution. Accordingly, if a comminution limit exists for the considered material, then a limiting grading curve also exists.
A useful tool for treating grading curves is the so-called grading entropy concept, where similar grading curves can be treated together. It was successfully applied in various grading-related problems, such as minimal and maximal void ratio, stability of granular filters and the grain skeleton, etc. Using this, (Lőrincz, Gálos, Trang, Rajkai, Fityus, & Telekes, 2005) and (Lőrincz, Kárpáti, Trang, Imre, & Fityus, 2011) have shown that sands with various initial grading curves converge towards a common point in the entropy diagram, with the most stable grading and a maximal grain size diversity (called relative base entropy and entropy increment). The speed of convergence depends on the strength of the individual grains comprising the hardness of the grain skeleton.

As can be seen from the above, the crushing of grains in an ensemble is a truly multi-level problem. At macro-level, there is the macroscopic stress state, the void ratio, and the (evolving) grading curve. On the meso-level, they influence the distribution of contact forces as force chains, the coordination numbers, and the breakage of individual grains. The breakage of single grains depends on micro-level properties such as grain shape, mineral composition, inner stress state and fracture toughness.

## 1.2 DEM approaches to particle crushing

The Discrete Element Method (DEM) has become an established tool to investigate multiple-body and contact problems, which are discontinuous in their nature, and cannot be treated analytically. In particular, it can be used to examine phenomena which are difficult or impossible to analyze in physical experiments, such as force chains in granular media. Since most DEM codes use basic elements which are rigid, in the context of grain crushing, they are suitable to model the relations between the macro- and meso-levels described above, but can also be applied to simulate the micro-level behaviour of single grains. An overview of grain crushing concepts in DEM is be given below.

Modelling the crushing of particles in DEM involves numerous aspects, which cannot be fulfilled equally well with today's computational resources and available programs. Because of this, three basically different concepts have been established by now, each containing different benefits and drawbacks. An overview of these three approaches is given in Table 1. Of course, the list of pros and contras is not complete; it only reflects the most important aspects in the view of the authors.
The aspects to be considered can be classified roughly in 2 groups: physical considerations and computational aspects.

The first approach uses a smaller number of elementary units (e.g. spheres) for the grain ensemble, usually one sphere stands for one grain, or the grain is made up of heavily overlapping spheres forming a rigid body (clump). First, a previously defined failure criterion is checked, which determines if the particle breaks under the current arrangement of contact forces. The failure criterion usually involves the largest contact force $F_{max}$, and sets up an analytical connection between contact force and the inner stress field. Other variables may be the coordination number, quantities relating to particle shape; a random strength may also be defined for each particle. If the failure criterion is met, the grain is erased and subsequently replaced by fragments, i.e. smaller, but similar grains. The number and position of the fragments is pre-defined. This is one of the critical aspects in this approach, since the fragments should fit into the volume occupied by the broken grain without a large volume loss, and without inducing large stresses due to overlap. An "artificial" size limit may be

imposed on the crushing process. This approach was put to use e.g. in (Lobo-Guerrero, Vallejo, & Vesga, 2006), (Lobo-Guerrero & Vallejo, Discrete element method analysis of railtrack ballast degradation during cyclic loading, 2006), and (Marketos & Bolton, Compaction bands simulated in Discrete Element Models, 2009).

The second approach makes use of crushable macrograins, built up from a large number of elementary units (called micrograins in this paper) connected by breakable bonds. The failure criterion is checked implicitly, since it is "included" in the stress check of the bonds. Similarly, no rule has to be defined for the fracture process, since the fragments develop with the breakage of the bonds. The size of the macrograins inherently sets a limit on the comminution process. This approach was used e.g. by (Whittles, Kingman, Lowndes, & Jackson, 2006), (Refahi, Mohandesi, & Rezai, 2010)(Oquendo, Muñoz, & Lizcano, 2009), (McDowell & Harireche, 2002), (McDowell & Harireche, 2002), (Cheng, Nakata, & Bolton, Discrete element simulation of crushable soil, 2003), (Cheng, Bolton, & Nakata, 2004). A more detailed overview of these models will be given in Section 1.4.

The third approach may be considered the most advanced, but computationally the most demanding one. It comprises a coupled DEM-FEM model, where the contact problem between the grains is calculated using DEM, and the internal stresses inside the particles are calculated using a continuum mechanical approach (Finite Element Method – FEM). Here, the connection between contact forces and internal stresses is no longer analytical, and the fracture may develop along "yielding" points inside the grain. Investigations based on this approach were presented e.g. by (Liu, Kou, & Lindqvist, 2005), (Kou, Liu, Lindqvist, Tang, & Xu, 2001), and (Bagherzadeh, Mirghasemi, & Mohammadi, 2011). A common feature of these models is that they are all 2D, showing the high complexity of such models.

**1. Table: Overview of grain crushing concepts in DEM**

| **Approach** | **Replacement of broken grains** | **Fracturing of macrograins** | **Coupled DEM + FEM** |
|---|---|---|---|
| *Internal stresses* | omitted/analytical | as contact and bond forces | FEM stress field analysis |
| *Failure criterion* | defined in advance, with considerable simplifications, crushing sensitive to its choice | inherent, defined by bond properties | defined as a general, stress-state based failure criterion |
| *Parameters controlling breakage* | defined "externally", e.g. max. contact force, coordination number | micromechanical parameters, e.g. contact stiffness, bond stiffness and strength | usual "continuum-mechanical" parameters, e.g. compressive and tensile strength |
| *Issues in the fracture process* | large volume loss and implosion, or high contact stresses | - | - |
| *Fractured shapes* | usually rounded, following given rule | realistic | realistic |
| *Comminution limit* | none, may be set | size of the micrograins | size of finite elements |
| *Void ratio, voids* | realistic, only between grains | very high, between and inside the grains | realistic, only between grains |
| *Element number* | initially low, increasing | high, steady | very high, steady |

From the 3 approaches presented, the replacement requires the most assumptions to be made about the stress state and failure criterion. The other two do not require such assumptions to be made, and the failure criterion is inherent as bond strength (macrograin concept), or may be defined in terms of stresses. Furthermore, they also allow damaged states prior to fracture.
Similarly, no rule has to be set for the fracture process; the fragments assume realistic shapes and fit smoothly into their surroundings. In contrast, a replacement rule has to be defined for the first approach, and a balance between volume loss and contact stresses caused by the fragments has to be found. This trade-off arises due to the following geometrical problem. If the rounded fragments had the same volume as the broken grain, they could only be arranged in a greater volume, causing high contact stresses. If they are to fit into the original space, this is only possible if some volume loss is allowed, but this introduces unrealistic voids which affect the compression when grain rearrangement occurs. It has to be considered though, that the macrograins made up of micrograins already contain a large internal void volume (see 2. Table 2).
Beside the above drawbacks, the replacement approach imposes no limit on the comminution of the grains, which is a significant limitation for the macrograin approach.
Furthermore, due to the small number of elements used, the replacement approach enables larger models to be run, and offers faster calculation at the start. However, as grain crushing commences, the element number can increase rapidly without a comminution limit. As for the macrograin approach, the element number is high already at the start, but stays constant during the calculation, which enables the optimization of memory allocation and other computational aspects. The coupled DEM-FEM model is the most resources-intensive, since each grain is divided into a large number of finite elements, with the FEM calculation for each grain conducted separately.
A general shortcoming of all of these approaches is that they cannot handle the formation of fine dust, as observed in reality. Since these very fine particles do not influence the behaviour of the ensemble significantly, they may be neglected as separate particles, but up to ≈4% of the grain volume may be turned into dust (Guimaraes, Valdes, Palomino, & Santamarina, 2007), which is still a significant quantity. On the other hand, to use micrograins at the comminution limit – for silica sands lying in the µm-range (Kendall, 1978) – is out of the scope of possibilities given today's computational power.

## 1.3 Short overview of PFC3D

The program used for the simulations is PFC3D v.3.10 from Itasca Consulting Group Inc. The main features – with respect to the current research – are summarized below.
PFC3D is a discrete element method (DEM) based computer code, which is able to simulate the mechanical interaction of several discrete bodies in 3 dimensions. The elementary "bodies" used in the program are spheres, which can be combined to complex shapes using deformable bonds in the contact zones, or via "clumping", which means a perfectly rigid composition of the (usually overlapping) spheres forming the desired particle shape.

The interaction is simulated by solving the Newtonian motion equations in 3D, both translation and rotation are possible. The solution of the motion equations is calculated with the method of central differences, an explicit time integration scheme. A single calculation cycle consists of two main phases: the first, motion calculation phase is followed by the force-displacement calculation phase.
In the motion calculation phase, the initial configuration at the beginning of the current timestep contains the positions and velocities of the bodies, as well as the forces acting on them. The forces may be body forces (e.g. gravity), prescribed forces/moments, and contact forces resulting from the

previous calculation cycle. The configuration at the end of the timestep is then calculated from the motion equations, this concludes the motion calculation phase.

In the following force/displacement calculation phase, new contacts are detected, as well as existing contacts are updated. The calculation of the contact forces is done by the so-called “soft contact” model. Here, the spheres themselves are considered rigid, and their deformation is “localized” into the contacts as overlap, tangential relative translation and relative rotation. The contact forces and stiffness are calculated from the assigned contact constitutive model, depending on the actual deformation of the contact. In the force/displacement calculation phase, the overlap increment is calculated for each contact, and the contact forces are updated, based on the (tangent) stiffness modulus of the contact. For each contact, the deformation increment is divided into normal and shear components, and the contact force increment is calculated from the corresponding (normal or shear) stiffness modulus. (The conceptual contact model is shown below, see 1. Fig.)
In the current research, the nonlinear, stiffening Hertz-Mindlin contact model was used. (Itasca, 2003) The Hertz-Mindlin contact is only active in compression, and the resulting contact stiffnesses (both normal and shear) are a function of the two spheres’ shear moduli and Poisson’s ratios, the radii, and the actual overlap. The shear force in a contact without a parallel bond is limited by Coulomb’s law of friction.

Complex bodies can be created by bonding the spheres together. In the current project, so-called parallel bonds were used. These parallel bonds may be imagined as cementation between sandgrains. They provide additional stiffness to the contact (i.e. act “parallel” to the Hertz-Mindlin contact – hence the name), as well as normal (both tensile and compressive), bending, shear and torsional strength. The “cross-section” of a parallel bond is circular, with the radius $R_{pb}$ determined by the radius ratio $\alpha_{rad}$, and the radius of the smaller sphere: $R_{pb}=\alpha_{rad}\cdot\min(R_1,R_2)$ – with $R_1$ and $R_2$ being the radii of the joined spheres. The bond’s length is equal to the distance between the centres of the joined spheres. The shear and normal stresses are calculated according to the elastic beam theory, and they are compared with the defined shear and normal strengths. (The failure criteria are uncoupled; the failure surface is a rectangle in the σ-τ-coordinate system.) If any stress in the parallel bond reaches the corresponding strength, the bond fails, it is erased, and the connected spheres subsequently act as unbonded. Another important feature of parallel bonds is that they carry zero stress in the configuration they are generated – i.e. a Hertz contact force may already be present in the contact.
Another bond type may also be used, the contact bond. A contact bond can only transmit normal and shear force, but no moments, and it’s stiffness cannot be adjusted in the program.

Combining groups of spheres into clumps means that their relative positions are fixed, and the group acts as a single rigid body with deformations limited to the outer boundaries. This feature is especially helpful to protect the macrograins during sedimentation or other temporary phases.

An important feature of the Hertz-Mindlin contact model in PFC3D 3.1 is that the walls are treated unlimitedly stiff (i.e. only the ball properties are considered for the stiffness of the ball-wall contact).

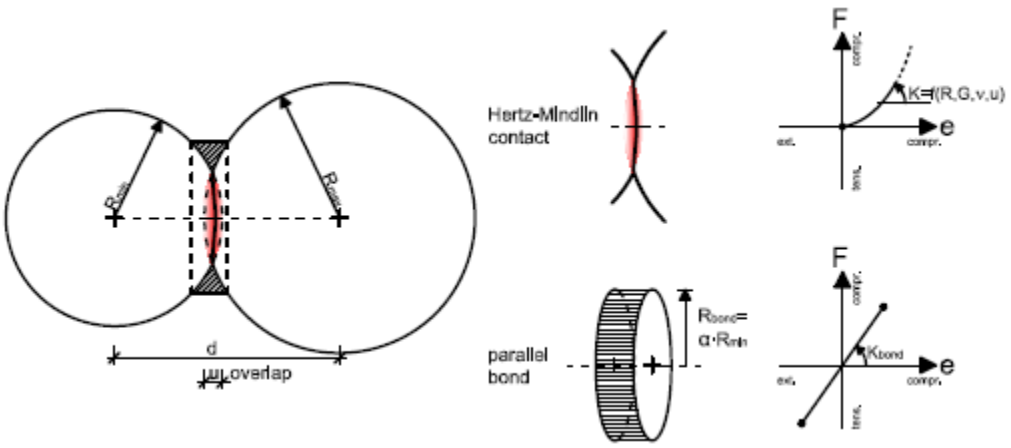


1. Fig.: Conceptual model of the grain contacts in this research

## 1.4 Recent developments and relations to the current model

After a short overview of the DEM program adopted in the current research, some recent developments and results regarding DEM simulation of oedometric compression tests and grain crushing based on the fracturing macrograins approach will be presented.

(Oquendo, Muñoz, & Lizcano, 2009) presented a simulated oedometric test on dry Guamo sand. They used their own DEM code which involved Hertz contacts between the grains. By varying the microparameters, they found a power-law connection between these and Bauer's macroscopic compression law (Bauer, 1995) for the investigated granulometry. Although no grain crushing was involved, they were able to reproduce the first part of the normal compression line for sand.

(Whittles, Kingman, Lowndes, & Jackson, 2006) investigated the crushing process of cylindrical rock specimen, focusing on the strain rate and crack propagation in the DEM simulations with parallel-bonded specimen. They used the linear contact model, and applied a normal distribution to the bond strengths.

(Refahi, Mohandesi, & Rezai, 2010) modelled the particle crushing process in a crusher. In connection with laboratory experiments, DEM and FLAC calculations were carried out on the spherical and cubic specimen. The parallel-bonded specimen in PFC3D contained more than 30000 micrograins, with a linear contact force-displacement law.

In their 2 papers, (McDowell & Harireche, 2002), (McDowell & Harireche, 2002) presented a single macrograin crushing test, and used these macrograins in a model for oedometric compression. They composed macrograins from uniform spheres in a regular (hexagonal close) packing, by bonding them together with contact bonds, and applied a linear contact force-displacement rule. To simulate inner flaws of the material, they randomly removed 0-25% of the micrograins, creating holes inside the macrograin. They showed that these macrograins exhibit a direction-dependent crushing strength, but the size effect is opposite than physically observed: larger grains tend to be stronger. By creating an ensemble of these macrograins, they are able to reproduce the typical e-lgσ plot with grain crushing, and find that the yielding point is proportional to the crushing strength of the grains.

(Cheng, Nakata, & Bolton, 2003) and (Cheng, Bolton, & Nakata, 2004) used similar macrograins to those by McDowell & Harireche: hexagonal packing and subsequently deleting a certain percentage of the micrograins. The preliminary results showed that no dynamic effects are likely to occur until very high strain rates. They simulated triaxial tests with different stress paths, starting from isotropic

compression. The results were evaluated in the framework of the Modified Cam Clay model, emphasising that the normality assumption for plastic strains was found not to hold.

In the current research, the Hertz-Mindlin contact model was adopted, which exhibits a nonlinear, stiffening character. This is perceived to be superior to the linear contact model for high contact forces.

Furthermore, the inner texture and flaws of a grain are simulated by using a range of micrograin diameters and applying a normal distribution to the bond strengths. The macrograins of (McDowell & Harireche, 2002) and (Cheng, Nakata, & Bolton, 2003) nevertheless showed a proper range of crushing strengths, but this was achieved by deleting some micrograins, which add inner voids to the macrograins. Their hexagonal close packing – when undisturbed – exhibits void ratio of ≈0.35, which is the lowest achievable value for equal spheres. When these macrograins are crushed, the inner voids turn to outer voids, which is hard to account for. On the other hand, the regular packing is lost during relative movements, leading to an increase in achievable lowest void ratio. With the current approach, the eventual "crystallization" of the macrograin due to a regular packing and uniform diameters can be avoided. Since the packing is irregular, but still compact, it may serve to identify the point until the compression curve is valid.

## 1.5 Statistics of particle strength

The resistance of a single grain against crushing forces depends on a number of factors. From the material side, there are e.g. mineral composition, size and distribution of inner flaws, state of weathering, and other factors determining the fabric of a mineral grain. From the load side, the number of contacts and the orientation of the acting forces are most important. (Guimaraes, Valdes, Palomino, & Santamarina, 2007), (Chuhan, Kjeldstad, Bjørlykke, & Høeg, 2002), (Nakata, Hyodo, Hyde, Kato, & Murata, 2001)

For brittle mineral grains, the main failure mode is splitting, caused by the splitting tensile stresses in the contact zone reaching the tensile strength of the material. (Russell & Wood, 2009) Since the calculation of the stress state inside the particle holds considerable uncertainties and is rather hard to carry out , usually simplified forms are put to use.

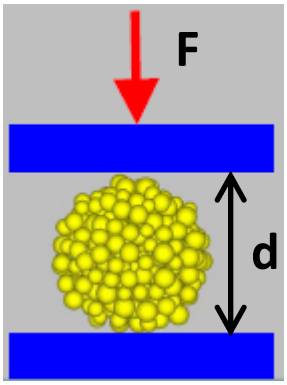


2. Fig.: Concept of a single grain crushing test

For calculating the tensile strength of a grain from a crushing test, (Jaeger, 1967) proposed the formula

$\sigma_t = F_{max}/d^2$ (1)

It is very similar to the tensile strength measurement by the Brazilian test, which also measures the tensile strength of rock indirectly. A single grain crushing test arrangement is shown in 2. Fig.

(Weibull, 1951) proposed a function for the survival probability of a beam in tension – based on the "weakest link"-theory –, depending on material strength variability and member volume:

$$P_s(V) = exp\left[-\frac{V}{V_0}\left(\frac{\sigma}{\sigma_0}\right)^m\right] = exp\left[-\left(\frac{d}{d_0}\right)^3\left(\frac{\sigma}{\sigma_0}\right)^m\right] \quad (2)$$

Since splitting occurs due to tensile material failure in the contact zone, the Weibull distribution was shown to apply also for the crushing strength of mineral grains. The right-hand side of Eq. (2) already contains the modification for the grain diameter *d*. For a grain with diameter *d*, Eq. (2) yields the probability that the grain remains intact (not crushed) when subjected to a force $F = \sigma \cdot d^2$. Similarly, in a uniform ensemble of grains with diameter *d*, all subjected uniformly to contact forces $F = \sigma \cdot d^2$, the percentage of surviving grains is predicted by Eq. (2).

The material constants in Eq. (2) are the characteristic strength $\sigma_0$ for a given reference diameter $d_0$, and the Weibull-modulus *m*. $\sigma_0$ is defined as the stress at which 37% of the grains with $d_0$ survive, and *m* describes the variability of the grain strength. A higher *m* means less variability with the individual grain strengths lying in a narrower range, and vice versa, see Fig. (next). The mean strength for an ensemble of grains with $d_0$ relates to $\sigma_0$ and *m* as follows: $\sigma_{mean}(d_0) = \sigma_0 \cdot \Gamma(1+1/m)$, where Γ is the Euler-gamma function. (McDowell, Statistics of soil particle strength, 2001) In the range of m=1.2-5.0, the function $\Gamma(1+1/m)$ assumes values between ≈0.88-0.94. Normalized plots (with $\sigma_0$=1) for the survival probability function are shown in 3. Fig., for different values of *m*.

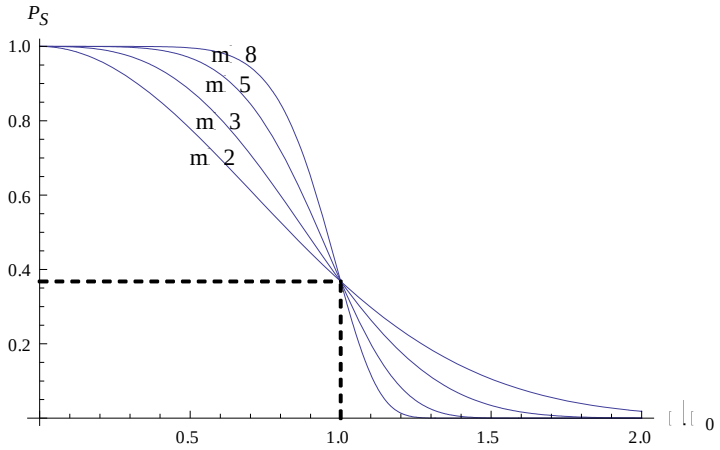


**3. Fig.: Normalized survival probability plots for different values of *m***

It shall be noted that Eq. (2) contains a pronounced size effect. The distribution of grain strengths for arbitrary grain sizes (the derivative of the survival probability function) becomes a surface:

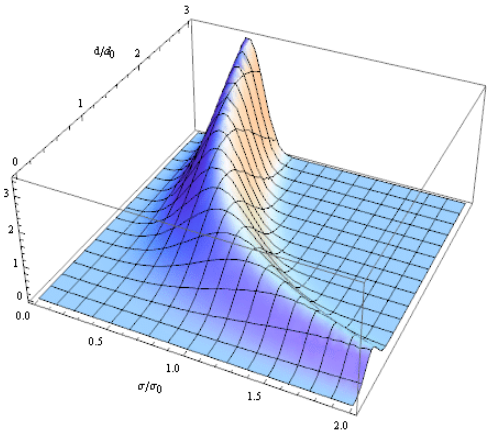


**4. Fig.: Distribution of grain strengths σ for arbitrary *d*, normalized with respect to $\sigma_0$ and $d_0$**

4. Fig.4. reflects that the larger grains are expected to be weaker, since they are more likely to contain larger inner flaws. In contrast, the size of inner flaws decreases with crushing; and the small grains exhibit a larger characteristic strength. However, it was shown(Nakata, Hyde, Hyodo, & Murata, 1999) that the size effect depends largely on the inner texture of the grain, and real grains do not always follow the "rule" given in (2). Also, as noted by (Duxbury, Kim, & Leath, 1994), the size effect is quite weak, and can be determined reliably only over a large sample size range.
The method for estimating the parameters of the Weibull distribution, along with the reliability of the results, are dealt with in (McDowell, Statistics of soil particle strength, 2001). Reported Weibull moduli range between $m$≈1.3-3.5 (McDowell, Statistics of soil particle strength, 2001) and $m$≈1.2-3.1 (Nakata, Kato, Hyodo, Hyde, & Murata, 2001). For $m$≈3-4, 30 tests suffice to estimate the mean strength to be within 10-15% of the true mean with a confidence level of 95%.

In a broader context, (Duxbury, Kim, & Leath, 1994) have presented that besides the Weibull-distribution, a modified form of the Gumbel-distribution can also be derived for the fracture statistics on sound micromechanical and mathematical foundations. If the flaws are "placed" into grains at random positions, e.g. by deleting bonds or micrograins – as is usual for DEM simulations based on the fracturing macrograins concept –, then the crack size distribution will exhibit an exponential tail (relating to the modified Gumbel-distribution of strength). On the other hand, dynamic crack growth models can predict both algebraic-tailed and exponential-tailed crack populations. Then an algebraic flaw population will lead to the Weibull-distribution of grain strength.
To choose between the two models would require simulations over several orders of magnitude in sample size, which is unfeasible with today's computational capacities. This means that the size effect is quite weak over small grain size ranges. Choosing the "wrong" model does not cause significant errors in the computations, which makes the use of the Weibull-distribution a valid choice in the practical cases.

# 2 Macrograin generation

This section contains an overview of the macrograin geometry used in the current research.

The macrograins are composed of many smaller micrograins, which are bonded together by parallel bonds. The macrograins are shaped to 3 different sizes for the oedometer tests: diameters of 2mm, 3mm and 4mm are generated. The procedure is based on the bonded specimen generation procedure available as a program module in PFC3D; it consists of the following steps:

1. A box container (cube) is filled with micrograins (spheres) in an irregular, dense packing, under zero friction. The diameters of the micrograins assume a predefined range: they uniformly cover a range of $d_{min}$ to $1{,}5 \cdot d_{min}$ (radius ratio = 1,5), with a mean diameter of $d_{mean}$=0,5mm. The micrograin-to-micrograin contacts have a stiffness modulus of 10 MPa.
   (The number of particles is determined such that the resulting void ratio should be 0.54 at their desired size. Then the particles are placed inside the container, at random positions, with half of their final size to facilitate placing them without overlaps. Then their size is increased to the final value and the ensemble is equilibrated. The resulting state is in an arbitrary – not isotropic – stress state, and the void ratio will be only approximately 0.54)
2. In order to ensure proper contacts, the micrograins are compressed to an isotropic stress of 1 kPa.
   (The container walls are moved until the stress in all 3 directions is the same. This ensures that there are no unloaded/loose regions, or no high stresses remain due to high confinement – i.e. a low locked-in stress is reached. If loose regions were present, then they could not be bonded together properly. Conversely, if high contact forces are present during bond installation, then a considerable amount of bond strength is "used up" to carry the

contact forces after the confinement is released – e.g. in the oedometer and in the single grain crushing tests.)

3. Prior to adding the parallel bonds, the so-called floaters are eliminated. Floaters are those "loose" micrograins which have less than 3 contacts. Their radii are increased until they reach a stable position.
   (In the practical cases, the increase in radius is not large, and the resulting radii will still show the initial uniform distribution – within the tolerance for a valid realization.)
4. Parallel bonds are added to the prepared specimen.
   (The parallel bonds don't carry forces in the position they are installed. Later, when the confining walls are removed, they keep the micrograins from falling apart. This imposes locked-in bond forces which result in a stress state opposite to the isotropic compression of step 2. This is the reason why the level of locked-in stress shall be low.)
5. The specimen is trimmed to the desired shape: with the diameter of the spherical macrograin prescribed (2-3-4 mm), the micrograins not contained completely inside this envelope are removed. (The sphere's centre coincides with the centre of the container box.)
6. The micrograin geometry data (centre coordinates, radii) are exported to an external file, for later use in the oedometer and in the single macrograin crushing tests.

Steps 1-4 are „Itasca standard", as delivered in the PFC3D module, while steps 5-6 are the addition of the authors. A detailed description of steps 1-4 can be found in (Itasca, 2003). The macrograin generation steps are shown in 5. Fig.:

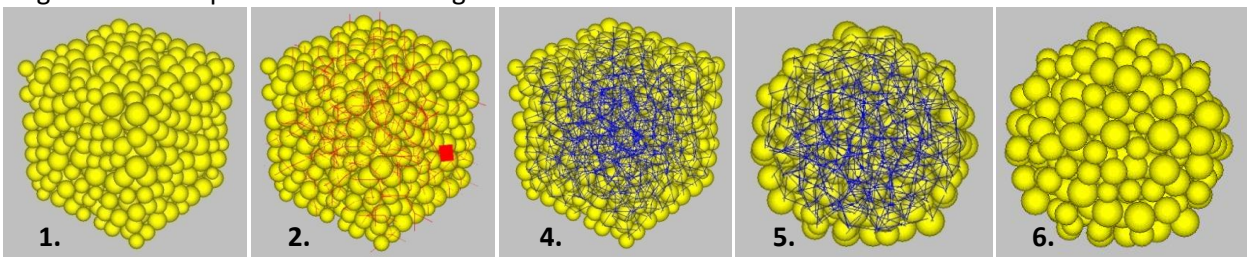


**5. Fig.: Macrograin generation steps**

It shall be noted that the micrograin stiffness in step 1 has only a small effect on the later grain behaviour; it only has to be high enough to keep the contact deformations sufficiently low at the induced isotropic stress level. Furthermore, the parallel bond properties (stiffness and strength) in step 4 are later of no importance in the oedometer model, since the bonds are stress-free in the last steps when the micrograin arrangement is saved.
The round envelope shape does not cause unrealistic behaviour, because the surface of the macrograin still remains rough. Furthermore, large rotations cannot develop within the oedometer without large relative displacements, which can occur only after grain breakage in the locked-in ensemble. The geometrical properties of the macrograins are summarized in Table A:

**2. Table: Geometrical properties of the macrograins**

| | normal resolution | | | | | |
|---|---|---|---|---|---|---|
| Macrograin diameter $D_{macro}$ (mm) | Micrograin diameter $d_{micro}$ (mm) | Mean micrograin diameter $d_{mean}$ (mm) | Number of micrograins | Total volume of micrograins $V_{micro}$ ($mm^3$) | Number of contacts/ bonds | Measured core void ratio $e_{core}$ (-) |
| 2.0 | 0.4 - 0.6 | 0.5 | 48 | 2.584 | 169/84 | 0.588 |
| 3.0 | 0.4 - 0.6 | 0.5 | 155 | 8.807 | 691/341 | 0.581 |
| 4.0 | 0.4 - 0.6 | 0.5 | 365 | 21.707 | 1782/881 | 0.556 |

| | 4x resolution | | | | | |
|---|---|---|---|---|---|---|
| Macrograin diameter $D_{macro}$ (mm) | Micrograin diameter $d_{micro}$ (mm) | Mean micrograin diameter $d_{mean}$ (mm) | Number of micrograins | Total volume of micrograins $V_{micro}$ ($mm^3$) | Number of contacts/ bonds | Measured core void ratio $e_{core}$ (-) |
| 2.0 | 0.252 - 0.378 | 0.315 | 120 | 1.631 | 523/252 | 0.611 |
| 3.0 | 0.252 - 0.378 | 0.315 | 468 | 7.032 | 2237/1136 | 0.553 |
| 4.0 | 0.252 - 0.378 | 0.315 | 1183 | 18.142 | 6261/3040 | 0.555 |

Compared to the normal resolution, the micrograin volume is 1/4, thus the diameter is multiplied by $(1/4)^{1/3}$

| | 2x resolution | | | | | |
|---|---|---|---|---|---|---|
| Macrograin diameter $D_{macro}$ (mm) | Micrograin diameter $d_{micro}$ (mm) | Mean micrograin diameter $d_{mean}$ (mm) | Number of micrograins | Total volume of micrograins $V_{micro}$ ($mm^3$) | Number of contacts/ bonds | Measured core void ratio $e_{core}$ (-) |
| 4.0 | 0.317 - 0.476 | 0.397 | 553 | 16.878 | 2796/1358 | 0.554 |

Compared to the normal resolution, the micrograin volume is 1/2, thus the diameter is multiplied by $(1/2)^{1/3}$

| | micrograin diameter - high : low = 1 : 1 | | | | | |
|---|---|---|---|---|---|---|
| Macrograin diameter $D_{macro}$ (mm) | Micrograin diameter $d_{micro}$ (mm) | Mean micrograin diameter $d_{mean}$ (mm) | Number of micrograins | Total volume of micrograins $V_{micro}$ ($mm^3$) | Number of contacts/ bonds | Measured core void ratio $e_{core}$ (-) |
| 4.0 | 0.50 - 0.50 | 0.50 | 283 | 16.706 | 1086/651 | 0.596 |

All micrograins have the same diameter.

| | micrograin diameter - high : low = 3 : 1 | | | | | |
|---|---|---|---|---|---|---|
| Macrograin diameter $D_{macro}$ (mm) | Micrograin diameter $d_{micro}$ (mm) | Mean micrograin diameter $d_{mean}$ (mm) | Number of micrograins | Total volume of micrograins $V_{micro}$ ($mm^3$) | Number of contacts/ bonds | Measured core void ratio $e_{core}$ (-) |
| 4.0 | 0.27 - 0.75 | 0.50 | 281 | 16.202 | 1023/636 | 0.529 |

# 3 Single macrograin crushing tests

## 3.1 Overview

In order to get an insight into the crushing behaviour of the single micrograins, parameter analysis test series were conducted for the most important grain parameters. The properties of the reference-configuration are given in 3. Table. (Apart from the geometrical properties already given in 2. Table)

3. Table: Summary of the reference macrograin's properties

| **Micrograins properties** | | | | |
|---|---|---|---|---|
| $d_{micro}$ [mm] | Density ρ [g/cm3] | Young's modulus E [GPa] | Poisson's ratio ν [-] | Friction coefficient [-] |
| 0.4-0.6 | 2.65 | 90 | 0.08 | $0.55 \approx 29^{o}$ |
| **Parallel bond properties** | | | | |
| Normal and shear stiffness $K_{pb}$ [GPa/mm] | | Normal and shear strength $\sigma_{pb}$ [MPa] | | Radius ratio $\alpha_{rad}$ [-] |
| 475 | | 465 | | 0.5 |

The micrograin contact constitutive model is the Hertz-Mindlin model, with the input parameters E and ν taken from (Russell, Wood, & Kikumoto, Crushing of particles in idealised granular assemblies). The friction coefficient was adopted after (Ni, Powrie, Zhang, & Harkness, 2000).

Since the load bearing capacity of a parallel bond is calculated as the elastic bearing capacity of a cylindrical beam, the strength $\sigma_{pb}$ and the radius ratio $\alpha_{rad}$ are interdependent. In the current model, the radius ratio was – somewhat arbitrarily – set to $\alpha_{rad}$=0.5.

A novel feature is the introduction of fracture mechanical aspects. The strain energy release rate G (the energy necessary to tear apart atomic bonds and create new crack surfaces in a material) can be incorporated such that it matches the energy stored in a parallel bond at its failure. (McDowell, Bolton, & Robertson, 1996) reported G≈50 J/m$^2$ for silicates. For tension (mode 1 failure), the bond stiffness $K_{pb}$ was approximated such that the potential energy of the parallel bond $\Pi_{pb}$ was equal to

$$\Pi_{pb}=\Gamma\cdot A_{new} \quad (3)$$

where $A_{new}$ is the sum of new surfaces created by breaking the parallel bond. This yields

$$K_{pb}=\frac{1}{2}\frac{\alpha_{rad}{}^2\cdot\pi\cdot\sigma_{pb}{}^2}{\Gamma\cdot A_{new}} \quad (4)$$

A single crushing test consisted of the following steps:

1. Applying a random spatial rotation to the macrograin, defined by 2 random rotation angles $\alpha_0$ and $\beta_0$. (The grain is first rotated around the vertical "z" axis by $\alpha_0$, and then around the already rotated, horizontal "x" axis by $\beta_0$. The rotation angles are picked randomly from the ranges $\alpha_0 \epsilon$ [-π, π], $\beta_0 \epsilon$ [-π, π])
2. Dropping the grain onto the base platen and let it reach a stable position. (The grain is treated like a rigid body – clump – in order to prevent premature bond failure.) The spatial direction, defined by the angles α and β is tracked until equilibrium. α and β relate to $\alpha_0$ and $\beta_0$, but their values are somewhat different, due to the grain rolling into its stable position.
3. Placing the top platen. The top platen is positioned such that it touches upon the uppermost micrograin.
4. Grain crushing process with the following parameters:
   $10^{-8}$ s timestep x $2\cdot10^6$ cycles = 0.02 s compression time;
   strain rates: $D_{macro}$=4mm → 10 mm/s
   $D_{macro}$=3mm → 7.5 mm/s
   $D_{macro}$=2mm → 5 mm/s
   compressive strain ≈ 5%

A crushing test was accepted to be valid if the following criteria were met:

- pronounced force peak present,
- prominent post-peak drop in compressive force
- ratio of broken bonds starting from 0, following the force diagram

A typical force-displacement diagram is presented in 6. Fig., with the force (black) and the ratio of broken bonds (red) plotted against the compressive strain:

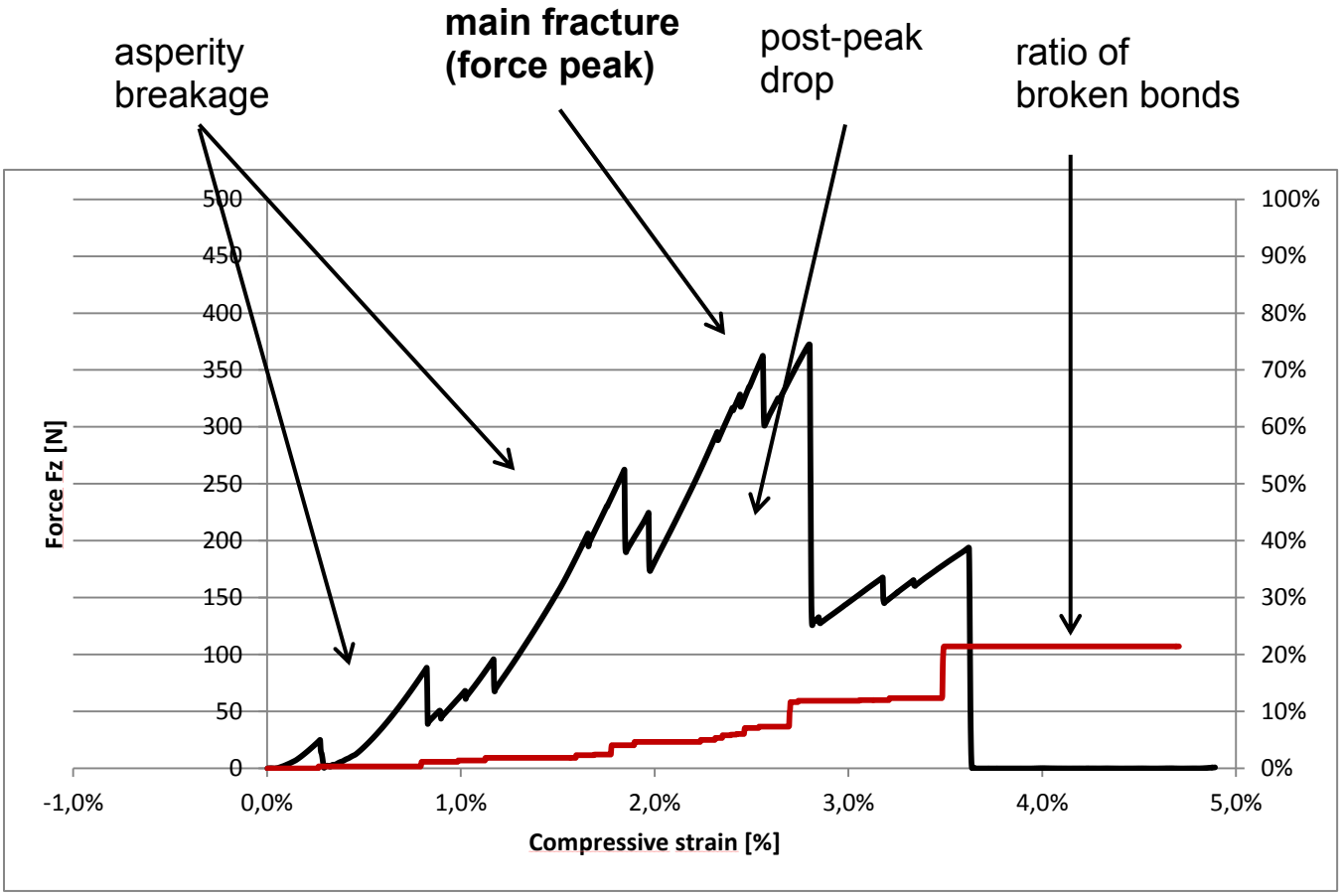


6. Fig.: Force-displacement diagram of a single macrograin crushing test, with ratio of broken bonds

At the beginning of crushing process, the "sawtooths" local peaks on the force diagram mark minor damage to the grain: asperity breakage, where outcropping edges and corners are broken. (The current model cannot reproduce the lightest, abrasion-type damage.) The main fracture appears at the force peak, where the microcracks coalesce into the larger main fracture, also visible as a jump in the ratio of broken bonds. The sudden drop after the peak force reflects a rather brittle, splitting-type failure. However, the remnants are also able to carry some load, this is visible as the slightly increasing part after the post-peak drop.

For evaluating the grain strengths and the survival probabilities (Section 1.5), the peak force was extracted for each valid test.

The stiffness of a grain may be approximated as a tangent to the force diagram's rising part. The results showed high variability of the stiffnesses, similarly to the variability of strengths described in Section 3.3.

## 3.2 Validation of the crushing process

In real grain crushing experiments, the displacement rate of the loading platen is much smaller than that used in the current simulations, approximately 0.01 mm/min (in: (Nakata, Hyde, Hyodo, & Murata, 1999)) to 0.01mm/s (in: (Arslan, Baykal, & Sture)). Also, the explicit time integration scheme of PFC3D requires smaller timesteps for more precise results.

In contrast, the vast amount of computational time required to run the test series makes a larger strain rate and longer timesteps more favourable.

Since the force-displacement laws for the micrograins and the parallel bonds are both rate-independent, only two factors may spoil the results: inertial forces due to high strain rates, and accumulating numerical integration errors due to overly large timesteps.

To validate the parameters for the crushing process, two control tests were run:

- one with a smaller strain rate of 0,1 mm/s; with the reference timestep of $10^{-8}$ s (referred to in the diagrams as “SmallStrainRate”)
- and another with a smaller timestep of $10^{-10}$ s; with the reference strain rate of 10 mm/s) (referred to as “SmallTimestep”)

The grain’s response to loading is best expressed through the force-displacement diagram. The damage to the grain may be described via the ratio of broken bonds (number of broken bonds against number of all bonds at the start of the test). Inertial forces or pressure waves may be caught by monitoring the difference of forces between the top and bottom platens (“force difference”, defined as $(F_{top}-F_{bottom})/F_{top}$).

The force-displacement diagrams, the evolution of the ratio of broken bonds, and the force difference are shown in 7. Fig., 8. Fig., and 9. Fig. respectively, all plotted against the compressive strain ε.

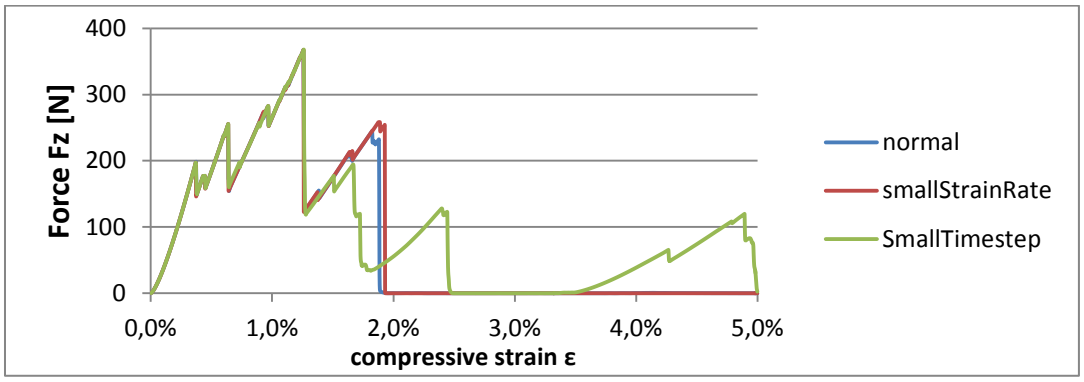


7. Fig.: Force-displacement diagrams for the validation tests

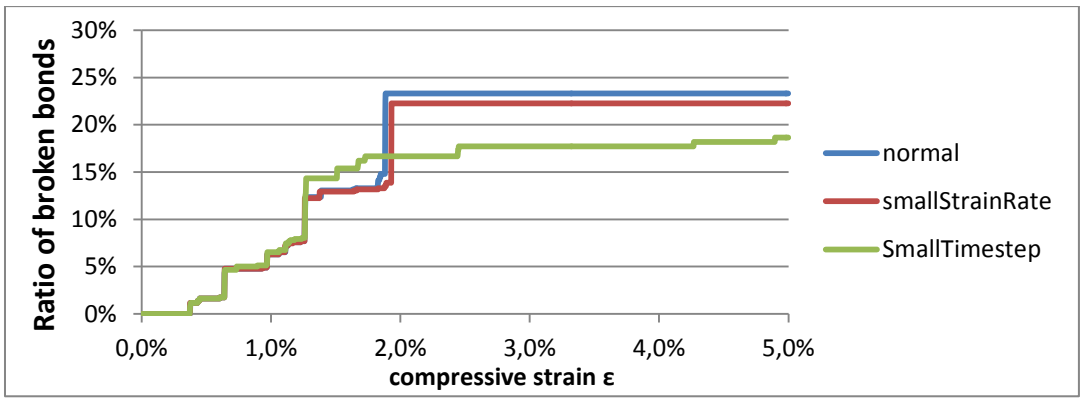


8. Fig.: Ratio of broken bonds in the validation tests

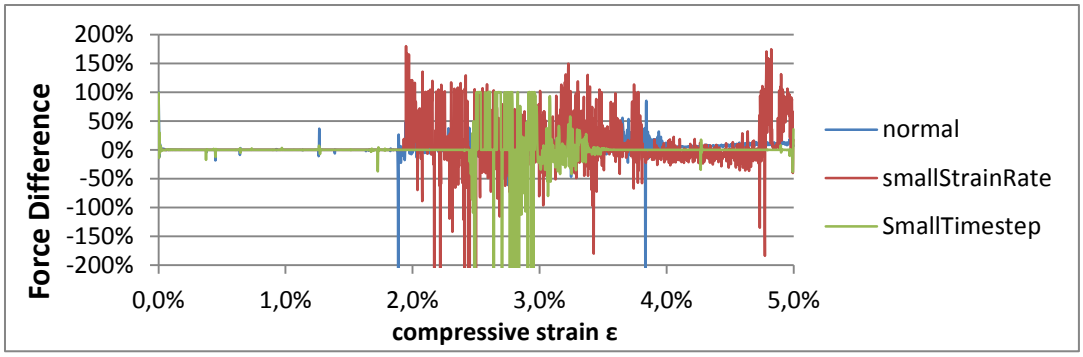


9. Fig.: Force difference between top and bottom platens in the validation tests

It can be seen that up to the force peak at approximately ε=1.3% compressive strain, both the force-displacement diagram (7. Fig.) and the ratio of broken bonds (8. Fig.) are identical in all 3 cases, with the force difference also being negligible (9. Fig.). The 3 cases start to differ after the post-peak drop around ε=1.3%, when the grain crushes into several parts and detaches from the loading platens. At this point, the fragments lose their stable positions and the grain disintegrates.
It is worth noting that the small and reference strain rates produce almost the same postcritical behaviour from ε=1.3% until ε=1.8%. Altogether, using the above parameters for the grain crushing process is justified, since they catch the main features of the grain crushing process correctly.
The above figures also show that the grains indeed behave rate-independent for the compression rates used in the simulations.

## 3.3 Suitability tests

The first objective of the single macrograin crushing tests was to prove that the idea of using the same macrograin multiple times in the oedometer can be justified. The main questions were:

- Does the simulated grain strength follow a proper distribution?
- Does the grain contain weak planes or directions?

The suitability tests comprised a series of $n$=96 single macrograin crushing test for the $D_{macro}$=4mm macrograin, with the grain properties given in 3. Table, and the procedure described in Section 3.1.

To answer the first questions, the survival probability was evaluated and the Weibull distribution parameters fitted. A description of the fitting procedure is given e.g. in (McDowell, Statistics of soil particle strength, 2001). Briefly, the crushing strengths (in this case, the forces, since $d$ from Eq. (1) is constant: $d$= $D_{macro}$=4mm) are put in ascending order, and a calculated survival probability $P_{s,cal}(i)=i/(n+1)$ is assigned to the i-th element F(i). These value pairs (F(i)- $P_{s,cal}$(i)) are represented in 10. Fig. as dots. The parameters of the Weibull distribution, $m$ and $F_0= \sigma_0 \cdot D_{macro}^2$, are found by linear regression from the Weibull plot. In the Weibull plot (not shown here, see e.g. (McDowell, Statistics of soil particle strength, 2001)), the values $\ln(\ln(1/P_{s,cal}(i)))$ are plotted against ln(F(i)). $m$ is then the slope of the linear regression line, while $F_0$ is found at the intersection of the regression line with the horizontal axis ln(F). The fitted survival probability after Eq. (2) is shown in 10. Fig. as the solid curve.

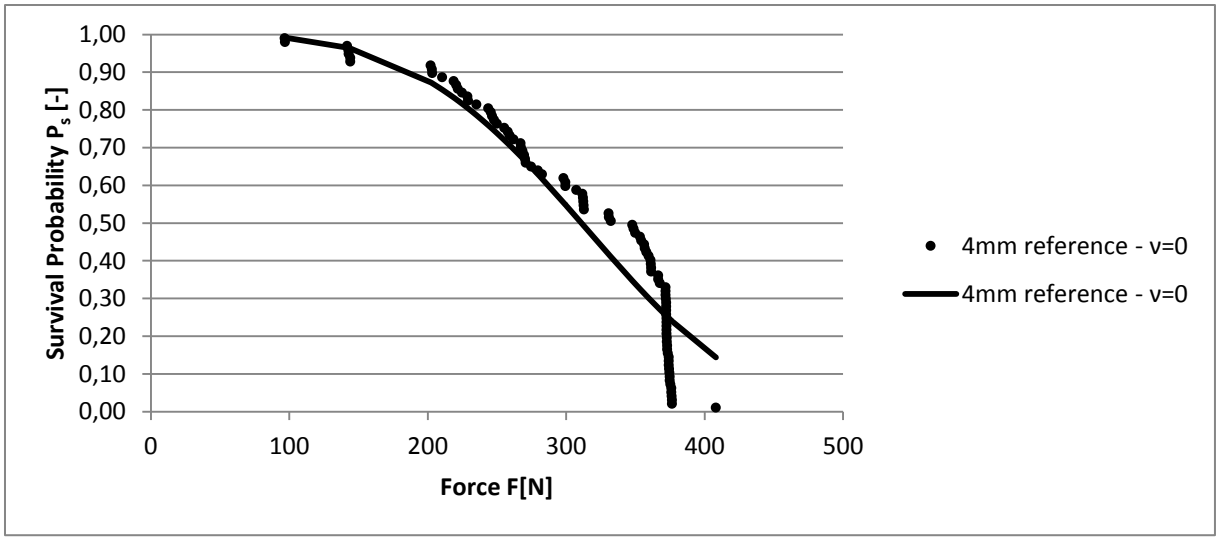


10. Fig.: Measured and predicted survival probabilities for the 4mm "reference" macrograins

The Weibull modulus evaluated to *m*=3.78, which is a realistic value for mineral grains according to (Nakata, Kato, Hyodo, Hyde, & Murata, 2001). The correlation coefficient of the linear regression in the Weibull plot was $R^2$=0.918, and $R^2$=0.907 was calculated for the fitted curve itself, but the curve shows a rather strong deviation in the upper range, it overestimates the measured survival probabilities. As will be seen later, each test series delivered similar results.

In each crushing test, the spatial orientation (given by the rotation angles α and β) of the grain was tracked until reaching a stable position. The crushing strengths are plotted against α and β in 11. Fig.11:

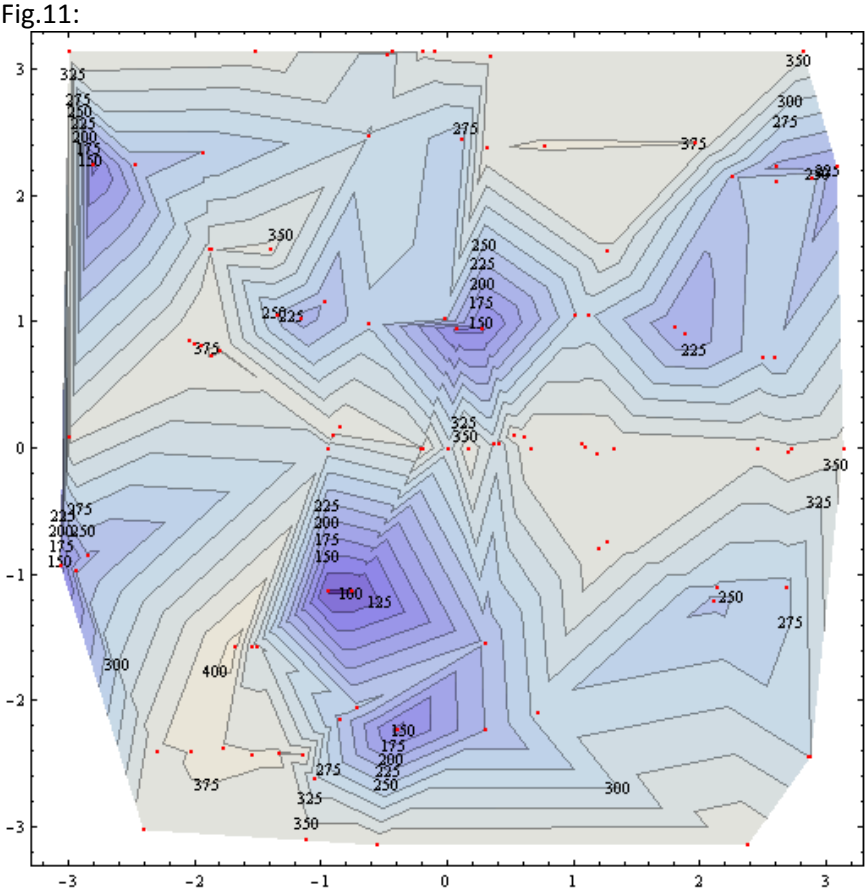

11. Fig.: Crushing strengths of the D=4mm "reference" macrograin; α on the horizontal axis, β on the vertical

The red points in 11. Fig. mark the (α, β)-pairs in the test series, and the contour plot's values are interpolated from the corresponding crushing strengths at each point. The plot shows a rather random pattern, while no weak plane or direction is apparent. The evaluation of other test series also delivered similar results.

The first conclusion that may be drawn from 10. Fig. and 11. Fig. is that a single macrograin exhibits a wide range of crushing strengths, depending on the direction of loading. Second, no weak planes are apparent, showing a proper inner structure resembling randomly distributed flaws. The latter observation is unlikely to be supported or refuted by real experiments due to the destructive testing method, but the DEM simulation allows the same grain to be tested in different conditions.

Altogether, using the same macrograin multiple times in the oedometer seems to be justified by the above results.

## 3.4 Parameter tests

A complete parameter analysis involving all the model parameters was not conducted due to the large number of possible parameters. Such complete analyses are possible with so-called "design-of-experiment" methods, presented e.g. in (Hanley, O'Sullivan, Oliveira, Cronin, & Byrne). Design-of-experiment methods also enable the identification of parameter interactions, and offer optimization possibilities for their calibration. Notwithstanding their merits in "fine-tuning" model parameters, they are time-consuming to carry out for a large number of parameters and possible parameter values.

In contrast, the influence of the selected main model parameters was investigated with a number of crushing test series, where only one of the parameters was changed at a time. Calibrating the macrograins to match some specified target values was out of the scope of the research, although it was required that the overall behaviour should resemble that of brittle mineral grains.

The investigated parameters can be grouped into 4 main categories, with a short description given below:

- **Parallel bond properties**
  - *Variability of bond strength*: normally distributed bond strengths; with ν=0.10, ν=0.25, ν=0.50, where ν=*s*/μ is the coefficient of variation (standard deviation/mean), and ν=0 in the reference case. The mean value μ was the same for the cases with different ν. These test series covered the $D_{macro}$=2mm, $D_{macro}$=3mm, and $D_{macro}$=4mm macrograins.
  - *Depleting bonds:* for 10% and 20% of the bonds, the bond strength was decreased to 1% of its original value. The rest of the bond strengths were left at their original, reference values. These test series covered the $D_{macro}$=2mm, $D_{macro}$=3mm, and $D_{macro}$=4mm macrograins.

    To examine the combined effect of depleted and "normally-distributed" bonds, 2 further test series were conducted on the $D_{macro}$=4mm macrograin, with 10%/20% of the bonds depleted, and a normal distribution with ν=0.25 for the rest.

    To investigate the effect of simultaneously decreasing the bond stiffness, a short test series was also carried out for $D_{macro}$=4mm, with both bond strength and stiffness reduced to 1% of the original value for 10% of all bonds. The intact bonds' strengths were chosen from a normal distribution with ν=0.25.
  - *Higher/lower bond strength*: the bond strengths were doubled and halved, to $2\cdot\sigma_{pb}$=930 MPa and $0.5\cdot\sigma_{pb}$=232.5 MPa. This was carried out on all macrograins, including $D_{macro}$=2mm, $D_{macro}$=3mm, and $D_{macro}$=4mm.

- *Higher/lower bond stiffness*: higher and lower bond stiffnesses were applied to the $D_{macro}$=4mm macrograin, 4· $K_{pb}$ =1900 GPa and 0.25· $K_{pb}$ =118.75 GPa were chosen instead the reference value of $K_{pb}$= 475 GPa.

- **Inner geometry of the macrograin**: (only on $D_{macro}$=4mm grain)
  - *Radius ratio of micrograins:* The ratio of the largest and smallest micrograins was 1:1 and 3:1. In the 1:1 case, all micrograins have the same diameter of $d_{mean}$=0,5mm. In the 3:1 case, the diameters are uniformly distributed between $d_{min}$ and 3·$d_{min}$, with $d_{mean}$=0,5mm.
  - *Macrograin resolution:* The macrograin is built up from smaller micrograins. In the case 2x (double resolution) the size range of the micrograins is scaled down such that their volume reduces to 1/2. In the 4x resolution case, the micrograin volume is scaled down to 1/4.

  For further details on the geometrical properties, see 2. Table.
- **Lateral constraint**:
  A box-shaped lateral confinement was added to prevent/reduce lateral expansion. The tests are conducted for v=0-0.10-0.25-0.50., but limited to the macrograin size $D_{macro}$=4mm.
- **Size effect**:
  Conducting the parameter tests on $D_{macro}$=2mm, $D_{macro}$=3mm, and $D_{macro}$=4mm enables to assess the size effect associated with the different parameters. For this end, the test series with the "reference" parameters, along with higher and lower bond strengths, "normally-distributed" and depleted bonds were carried out on all macrograin sizes, and the resulting strengths were compared on stress-basis, i.e. by calculating the grain strength according to Eq. (1).

The results of the parameter analysis series will be outlined below, along with the description of each series. The evaluation of the survival probability and the fitting procedure for the survival probability is identical to that described in Section 3.2. The relevant model parameter values are also given in each section, while the values belonging to the "reference" case are shown in 3. Table. In most cases, only 2 alternative values were tested against the reference configuration, and interactions may be present between certain parameters. Therefore, the interpretation of the results will be mainly qualitative, with the possible mechanisms described, but some tentative quantitative evaluation will also be provided.

The tables in each section contain the numerical results of the crushing series evaluations; with *n* being the number of valid results, $\sigma_{mean}$ the mean strength, $\sigma_0 = F_0/D_{macro}^2$ the characteristic strength, *m* the Weibull modulus, and $R^2$ the coefficients of determination for the survival probability $P_S$ and the Weibull plot regression.
As can be anticipated for the high values of $R^2$, the mean strength calculated from the Weibull-distribution for a given test series was always well within one standard deviation from the mean strength calculated from the raw results, calculated as $s_{mean} = s/\sqrt{n}$.

The results of the crushing test series are also shown in Fig. 11-20, with the actual crushing strengths displayed as dots and the fitted survival probabilities with continuous lines.

### 3.4.1 Normal distribution of bond strengths

Applying a normal distribution to the bond strengths is one possible way to simulate the inner flaws of the grain material. In the reference cases, each bond had the same strength $\sigma_{pb}$=465 MPa, and for

the cases with different v, these were overwritten by a random value drawn from a normal distribution. The mean value was fixed at $\mu=\sigma_{pb}=465$ MPa, and the standard deviation calculated as $s=v \cdot \mu$. A lower limit of $0.05 \cdot \sigma_{pb}$ was set for the random number, such that very low values were ruled out. All other parameter values were left unchanged, at their values shown in 3. Table.

For the normal distributions applied to the bond strengths, the increasing variability v results in decreasing grain strength. A plausible explanation for this may be that the cracks find their way through the weakest path. This is also visible in 13. Fig.

It is noteworthy that the decrease in $\sigma_0$ is practically equal to the coefficient of variation – i.e. v=0.10 results in approx. 10% drop in $\sigma_0$, while v=0.50 results in approx. 50% decrease. The Weibull modulus *m* increases slightly with increasing v.

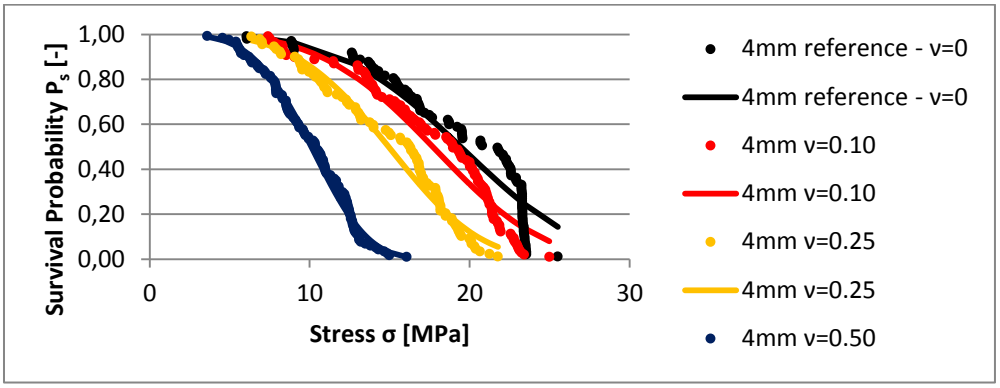


12. Fig.: Crushing test results for $D_{macro}$=4mm, normal distribution of bond strengths

4. Table: Crushing test results for $D_{macro}$=4mm, normal distribution of bond strengths

| $D_{macro}$ [mm] | Test series | test results | | fitted survival probability function | | | |
|---|---|---|---|---|---|---|---|
| | | n [-] | $\sigma_{mean}$ [MPa] | $\sigma_0$ [MPa] | m [-] | $R^2$ - $P_S$ | $R^2$ - Weib. pl. |
| 4 | v=0 (reference) | 96 | 19.22 | 21.42 | 3.78 | 0.907 | 0.918 |
| | v=0.10 | 106 | 17.54 | 19.51 | 3.75 | 0.956 | 0.941 |
| | v=0.25 | 88 | 14.84 | 16.45 | 3.80 | 0.969 | 0.969 |
| | v=0.50 | 117 | 10.03 | 11.05 | 4.09 | 0.990 | 0.988 |

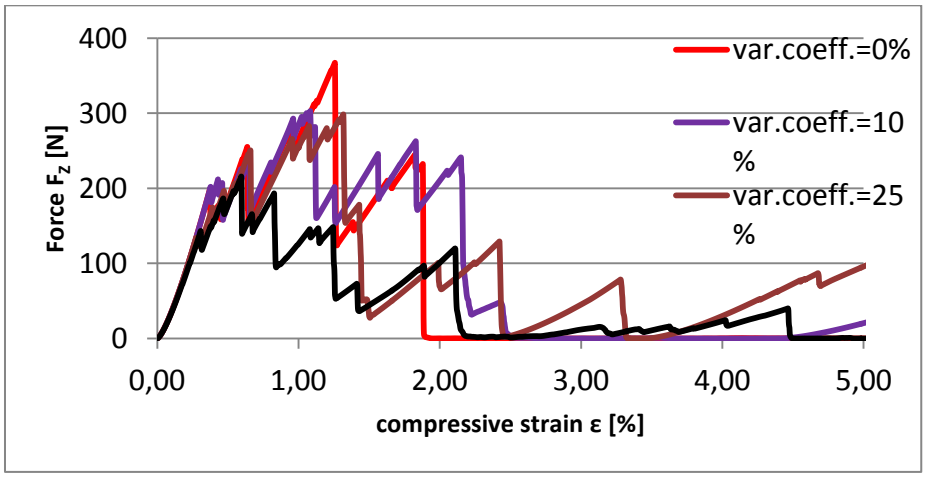


13. Fig.: Force-displacement plot for a crushing test with same initial conditions, but different v

### 3.4.2 Depleting bonds

Another possibility to include flaws in the grains is to “disconnect”, or deplete a certain number of bonds, as was shown by (Duxbury, Kim, & Leath, 1994). Due to numerical and programming considerations, the bond strength for the depleted bonds was not set to 0, but to 1% (4,65 MPa) of the original strength instead. It can be shown in a simple thought-experiment that this 1% (instead of 0) does not affect the grain’s strength in a significant manner.

To investigate the effect of depleted bonds, 10% and 20% of the bonds were depleted at random. To decide whether or not do decrease the bond strength, a random number between 0 and 1 was assigned to each bond, and if it was smaller than 0.1 or 0.2 respectively, the bond strength was decreased. All other parameter values were left unchanged, at their values shown in 3. Table.

The results are shown in the first lines of 5. Table, and visualized in 14. Fig.

The case with ν=0.25 and bonds depleted was chosen because the “flawless” parts of a mineral grain are also expected to show some variation and randomness in their texture. As the first step, the predefined amount of bonds (10% and 20% in the tests) was chosen at random, and their strength was decreased – as described previously. The second step consisted of randomizing the remaining 90% or 80% as described in the previous section. The limits for the random number generation was set such that the “not depleted” bonds should have a strength within $\pm 0.5 \cdot \mu$ around the mean (i.e. a deviation by +50% was allowed). This series enables to examine the joint effect of introducing flaws in two ways. 5. Table contains the numerical results, and Fig. 14. shows the corresponding plots.

It can be seen from the results that – as expected – a higher percentage of disconnected bonds leads to lower grain strength, and the Weibull-moduli m fall within the desired range for mineral grains. However, the bond strength decreases nonlinearly with increasing depleted bonds-ratio. The decrease is less and less with each increase: in the ν=0 case, the drop between 0% and 10% depleted is ≈31%, while between 10% and 20% it’s only ≈22%. The trend is similar in the ν=0.25 case: the decrease being ≈20% and ≈18%, respectively.

Cross-checking these results reveals that the flaws introduced by depleted bonds and the normal distribution on the intact ones “add up” in decreasing the ideal grain’s strength: in 14. Fig., the emerging curves show a lower strength for all ν=0- ν=0.25 pairs. However, the additional weakening by the normal distribution becomes less and less important with increasing ratio of depleted bonds: for 0% depleted the drop is ≈25%, for 10% depleted it reduces to ≈10%, while for 20% depleted it’s already only ≈7%.

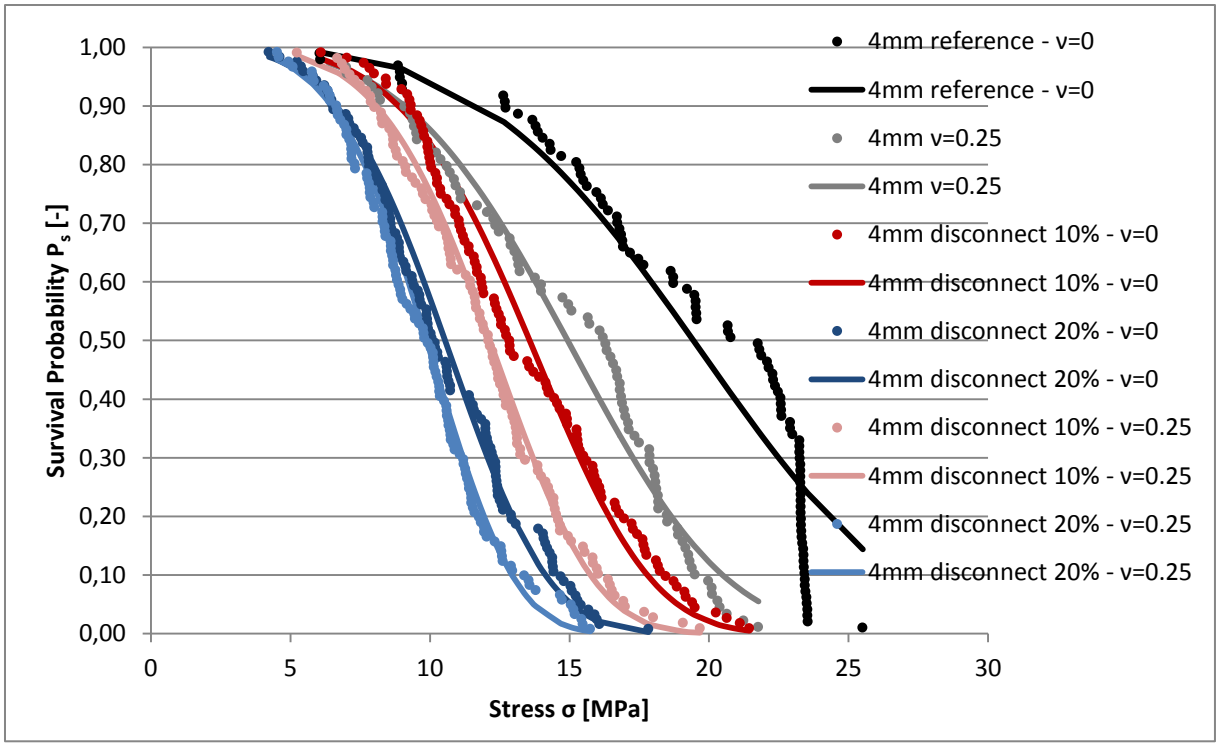


14. Fig.: Crushing test results for $D_{macro}$=4mm, bonds depleted (v=0, v=0.25)

5. Table: Crushing test results for $D_{macro}$=4mm, bonds depleted

| $D_{macro}$ [mm] | Test series | test results | | fitted survival probability function | | | |
|---|---|---|---|---|---|---|---|
| | | n [-] | $\sigma_{mean}$ [MPa] | $\sigma_0$ [MPa] | m [-] | $R^2$ - $P_S$ | $R^2$ - Weib. pl. |
| only bonds depleted | | | | | | | |
| 4 | 0% depleted, v=0 (reference) | 96 | 19.22 | 21.42 | 3.78 | 0.907 | 0.918 |
| | 10% depleted, v=0 | 111 | 13.45 | 14.74 | 4.43 | 0.974 | 0.962 |
| | 20% depleted, v=0 | 122 | 10.47 | 11.53 | 4.09 | 0.986 | 0.984 |
| bonds depleted + normal distribution | | | | | | | |
| 4 | 0% depleted, v=0.25 | 88 | 14.84 | 16.45 | 3.80 | 0.969 | 0.969 |
| | 10% depleted, v=0.25 | 107 | 12.03 | 13.15 | 4.61 | 0.995 | 0.983 |
| | 20% depleted, v=0.25 | 120 | 9.79 | 10.73 | 4.45 | 0.993 | 0.981 |
| bonds depleted: only strength vs. strength & stiffness | | | | | | | |
| 4 | 10% depleted, v=0.25 only strength decreased (*A*) | 21 | 11.84 | 12.84 | 5.23 | 0.932 | 0.945 |
| | 10% depleted, v=0.25 strength &stiffness decreased (*B*) | 21 | 11.63 | 12.58 | 5.46 | 0.947 | 0.923 |

Another issue is whether or not to decrease the depleted bond's stiffness along with the strength. We were not able to decide for one possibility over the other by reasoning alone – therefore we included a short comparison in the test series, with *n*=21 corresponding tests starting from the same initial conditions.

The comparison of the cases with only strength reduced (series *A*), and with both strength and stiffness reduced (series *B*) shows that the resulting average grain strength is practically the same: the mean and characteristic strengths $\sigma_{mean}$ and $\sigma_0$, as well as the Weibull-modulus *m* are almost

identical. To gain a deeper insight, we calculated the differences in the crushing strengths for each corresponding tests as $(F_B-F_A)/F_A$ and $F_B/F_A$; $F_A$ being the crushing force in series *A* and $F_B$ the crushing force in the corresponding test in series *B*. The mean strength $\underline{F_B}$ in series *B* evaluated to $\underline{F_B}=0.989\cdot\underline{F_A}$, with a standard deviation of $s$=0.101. Plotting the histograms for $(F_B-F_A)/F_A$ and $F_B/F_A$ shows that the differences between the series *A* and series *B* results are of random character (15. Fig. a and b). For the histogram of $(F_B-F_A)/F_A$ the fitted normal distribution is displayed, as is the fitted lognormal distribution for $F_B/F_A$. In our point of view, the ratio $F_B/F_A$ and the lognormal distribution are more appropriate to represent the differences, since a normal distribution may yield negative values, which is impossible for $F_B$. Another argument for the lognormal distribution is that the histograms show skewed datasets – however their skewness (0.766) is greater than for the lognormal distribution (0.305), and for the normal distribution (0). The kurtosis (6.102) is almost the double than for the lognormal distribution (3.166) and for the normal distribution (3), meaning that the values for $F_B$ are narrowly concentrated around $F_A$.

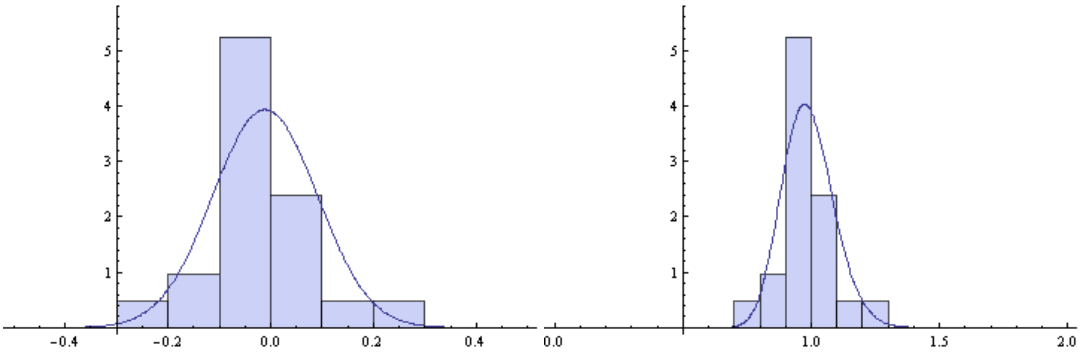


**15. Fig.: a) histogram for $(F_B-F_A)/F_A$, with fitted normal distribution; b) histogram for $F_B/F_A$, with fitted lognormal distribution**

Since the resulting strengths in series *A* and series *B* are very close to each other – as confirmed by the values in 5. Table and the histograms in 15. Fig. – only the bond strengths were decreased for the depleted bonds, and the stiffnesses were left unchanged.

### 3.4.3 High and low bond strengths and stiffnesses

To investigate the effect of the (average) bond strength on the grain strength, the parallel bond strengths were varies: one test series was run with the bond strength increased to $2\cdot\sigma_{pb}$=930 MPa and another test series with bond strength decreased to $0.5\cdot\sigma_{pb}$=232.5 MPa.

When doubling and halving the bond strengths, the corresponding characteristic and mean strength also doubled and halved, while the Weibull modulus *m* decreased moderately in both cases. Since crushing of the grains is mainly caused by splitting tensile stresses, which are carried predominantly by the parallel bonds, the nearly linear dependence of grain strength on bond strength seems appropriate.

The stiffness of a contact in PFC is the sum of the Hertz contact's and the parallel bond's stiffness (they act "parallel", see 1. Fig.), a larger variation was chosen for the parallel bond stiffness than for its strength. The two tested values were $4\cdot K_{pb}$=1900 GPa and $0.25\cdot K_{pb}$=118.75 GPa agains the reference value of $K_{pb}$= 475 GPa. The change in bond stiffness was found to be nearly linear, and inversely proportional to the change in $\sigma_{mean}$ and $\sigma_0$: the increase/decrease was approx. 11-14% when decreasing/increasing the bond stiffness to 0.25x / 4x of the reference value. This result may seem strange at first sight, but may be explained by the fact that in a contact, the contact force is divided between the Hertz-Mindlin contact and the parallel bond proportional to their stiffnesses. Increasing

the bond's stiffness causes a larger portion of the contact force to be carried by the bond, which consequently leads to higher stress and earlier failure. The Weibull modulus *m* decreased moderately in both cases. The results are presented in 6. Table and 16. Fig.

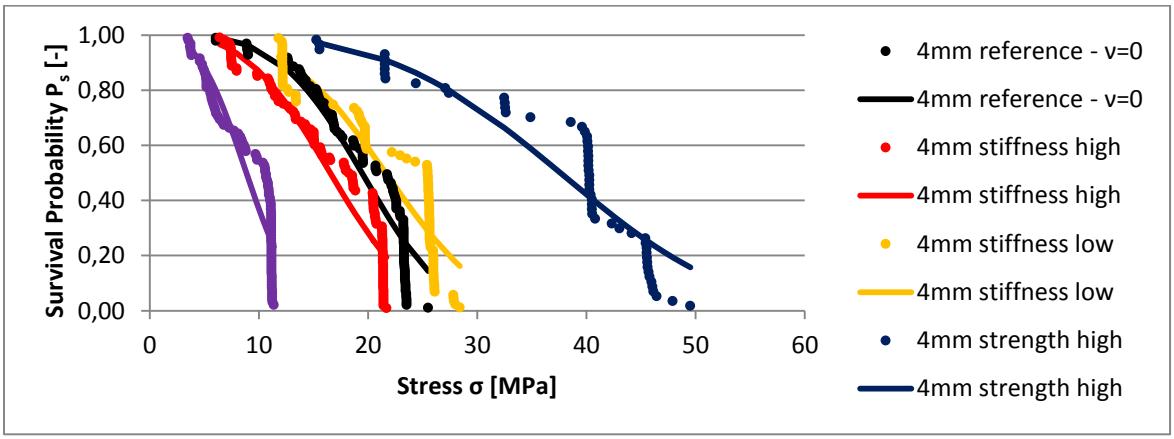


16. Fig.: Crushing test results for $D_{macro}$=4mm, high and low bond strengths and stiffnesses

6. Table: Crushing test results for $D_{macro}$=4mm, high and low bond strengths and stiffnesses

| $D_{macro}$ [mm] | Test series | test results | | fitted survival probability function | | | |
|---|---|---|---|---|---|---|---|
| | | n [-] | $\sigma_{mean}$ [MPa] | $\sigma_0$ [MPa] | m [-] | $R^2$ - $P_S$ | $R^2$ - Weib. pl. |
| **Parallel bond properties – strength and stiffness** | | | | | | | |
| 4 | reference | 96 | 19.22 | 21.42 | 3.78 | 0.907 | 0.918 |
| | High bond strength (930 MPa) | 56 | 37.24 | 41.69 | 3.57 | 0.862 | 0.890 |
| | Low bond strength (232.5 MPa) | 94 | 8.77 | 10.01 | 2.98 | 0.851 | 0.883 |
| | High bond stiffness (1900 GPa) | 107 | 16.49 | 18.56 | 3.17 | 0.920 | 0.911 |
| | Low bond stiffness (118.75 GPa) | 86 | 21.37 | 23.98 | 3.53 | 0.856 | 0.822 |

### 3.4.4 Inner geometry

In the parameter tests regarding the macrograins' inner geometry, two main aspects were examined. It's a general concept that with uniform particle sizes quasi-regular packings may appear, which can lead to "crystallization" of the grains – with certain directions acting as weak planes in the matrix. Conversely, a broader size-range can lead to tighter packings, but the (micro)grain size distribution for such cases is not uniform. For this end, the size range of the constituting micrograins was changed, with the mean value kept identical to the reference case, $d_{mean}$=0,5mm. The ratio of the largest and smallest micrograins was set to 1:1 and 3:1. In the 1:1 case (referred to in 17. Fig. as "hilo 1"), all micrograins have the same diameter of $d_{mean}$=0,5mm ($d_{max}/d_{min}$=1). In the 3:1 case (called "hilo 3" in 17. Fig.), the diameters are uniformly distributed between $d_{min}$=0.25mm and $d_{max}=3 \cdot d_{min}$=0.75mm, with $d_{mean}$=0.5mm.

Another common concept is that using more and more micrograins to build a macrograin– i.e. increasing its resolution – will lead to more realistic results in the crushing process. This may be true, but – as will be seen in Section 4.1 – this needs a rather large increase of the grains' resolution. On the other hand, the available computational power imposes a strong restraint on this approach. To investigate this effect, the macrograin was built up from smaller micrograins. In the case 2x (double resolution) the size range of the micrograins is scaled down such that their volume reduces to 1/2, i.e. the radius is decreased to $\sqrt[3]{1/2}$. In the 4x resolution case, the micrograin volume is scaled down to ¼, with the radius range is decreased to $\sqrt[3]{1/4}$. An overview of the geometrical properties is given in 2. Table.

The parameter tests on the geometrical properties delivered the least number of valid results, 35 to 36, which are still sufficient for a proper evaluation. Surprisingly, each variation resulted in significantly weaker grains. The changes in the size range of the micrograins do not show a consistent trend: both the radius ratios of 1:1 and 3:1 appear weaker than the reference case with 1.5:1. Increasing the resolution of the macrograins (using smaller micrograins) resulted in constantly decreasing grain strength. The Weibull modulus *m* varied strongly in these test series. In the light of these results, a more detailed analysis on the inner geometrical properties would eventually be appropriate.

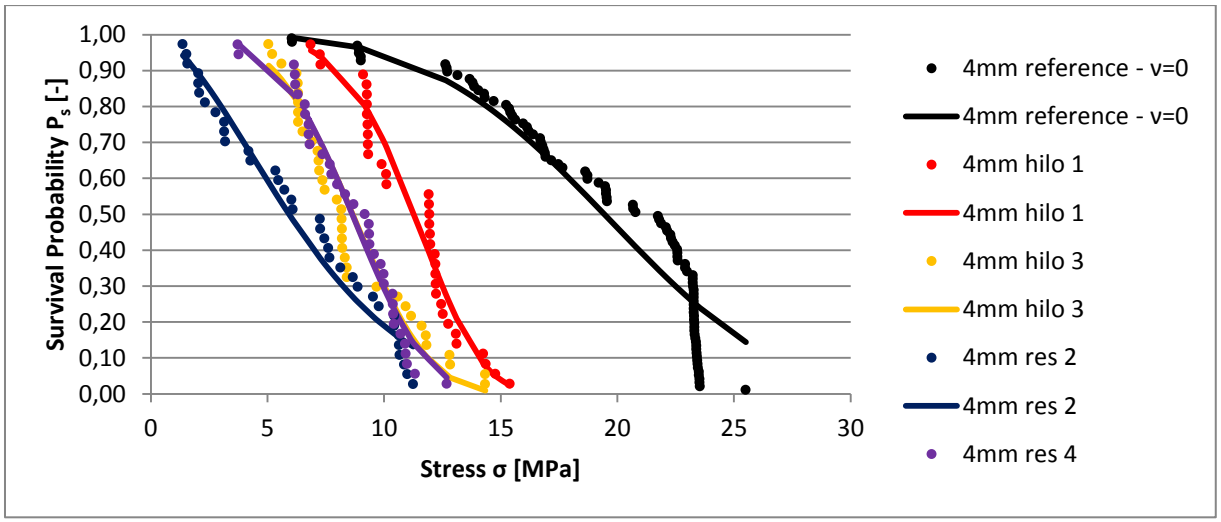


17. Fig.: Crushing test results for $D_{macro}$=4mm, different inner geometries

7. Table: Crushing test results for $D_{macro}$=4mm, different inner geometries

| $D_{macro}$ [mm] | Test series | test results | | fitted survival probability function | | | |
|---|---|---|---|---|---|---|---|
| | | n [-] | $\sigma_{mean}$ [MPa] | $\sigma_0$ [MPa] | m [-] | $R^2$ - $P_S$ | $R^2$ - Weib. pl. |
| Inner geometry properties | | | | | | | |
| 4 | reference | 96 | 19.22 | 21.42 | 3.78 | 0.907 | 0.918 |
| | Radius ratio 1:1 | 35 | 11.16 | 12.08 | 5.47 | 0.942 | 0.942 |
| | Radius ratio 3:1 | 36 | 8.60 | 9.53 | 3.80 | 0.908 | 0.887 |
| | 2x resolution | 36 | 6.41 | 7.37 | 1.68 | 0.965 | 0.949 |
| | 4x resolution | 35 | 8.56 | 9.49 | 3.89 | 0.974 | 0.952 |

### 3.4.5 Lateral constraint

To investigate the crushing resistance in a confined condition, lateral walls were added. After the grain has come to a rest, 4 lateral walls were placed along with the top platen. These lateral walls formed a rectangular box, touching upon the grain at 4 contact points. The crushing process then commenced as in the unconfined cases. The test series was repeated with lateral confinement for each case described in Section 3.4.1 (v=0-0.10-0.25-0.50). 18. Fig. and 8. Table present the results, with the dashed lines showing the fitted curves for the unconstrained cases. There's only a slight difference between the crushing strengths in the unconfined and confined cases:

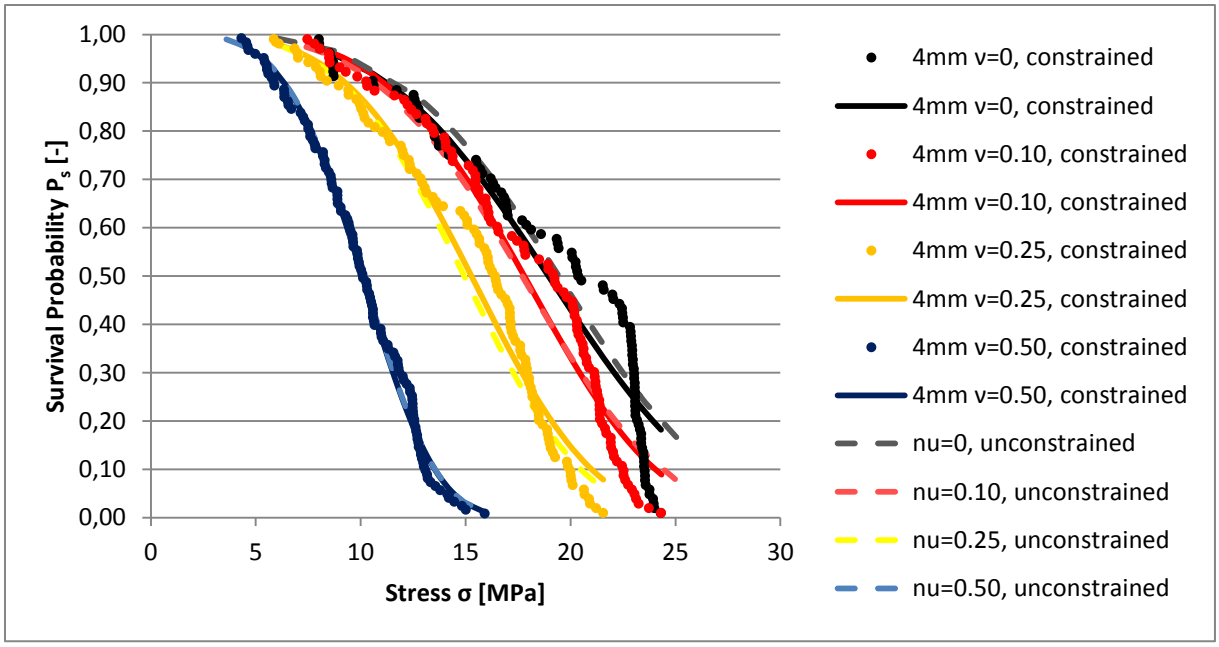


18. Fig.: Crushing test results for $D_{macro}$=4mm, laterally confined cases

8. Table: Crushing test results for $D_{macro}$=4mm, laterally confined cases

| $D_{macro}$ [mm] | Test series | test results | | fitted survival probability function | | | |
|---|---|---|---|---|---|---|---|
| | | n [-] | $\sigma_{mean}$ [MPa] | $\sigma_0$ [MPa] | m [-] | $R^2$ - $P_S$ | $R^2$ - Weib. pl. |
| **Reference cases** | | | | | | | |
| 4 | unconstrained, v=0 (reference) | 96 | 19.22 | 21.42 | 3.78 | 0.907 | 0.918 |
| | constrained, v=0 | 103 | 18.79 | 20.97 | 3.61 | 0.911 | 0.919 |
| | unconstrained, v=0.10 | 106 | 17.54 | 19.51 | 3.75 | 0.956 | 0.941 |
| | constrained, v=0.10 | 102 | 17.63 | 19.51 | 3.99 | 0.958 | 0.959 |
| | unconstrained, v=0.25 | 88 | 14.84 | 16.45 | 3.80 | 0.969 | 0.969 |
| | constrained, v=0.25 | 103 | 15.17 | 16.84 | 3.77 | 0.962 | 0.967 |
| | unconstrained, v=0.50 | 117 | 10.03 | 11.05 | 4.09 | 0.990 | 0.988 |
| | constrained, v=0.50 | 122 | 10.00 | 11.02 | 4.08 | 0.993 | 0.985 |

Examining the corresponding force-displacement diagrams (belonging to the same initial conditions, the only difference being the confinement) reveals that the confinement usually increases the resistance, but only slightly and not in a consistent way. In some cases, even reduced resistances were observed. Three examples for corresponding force-displacement diagrams are shown in 19. Fig.:

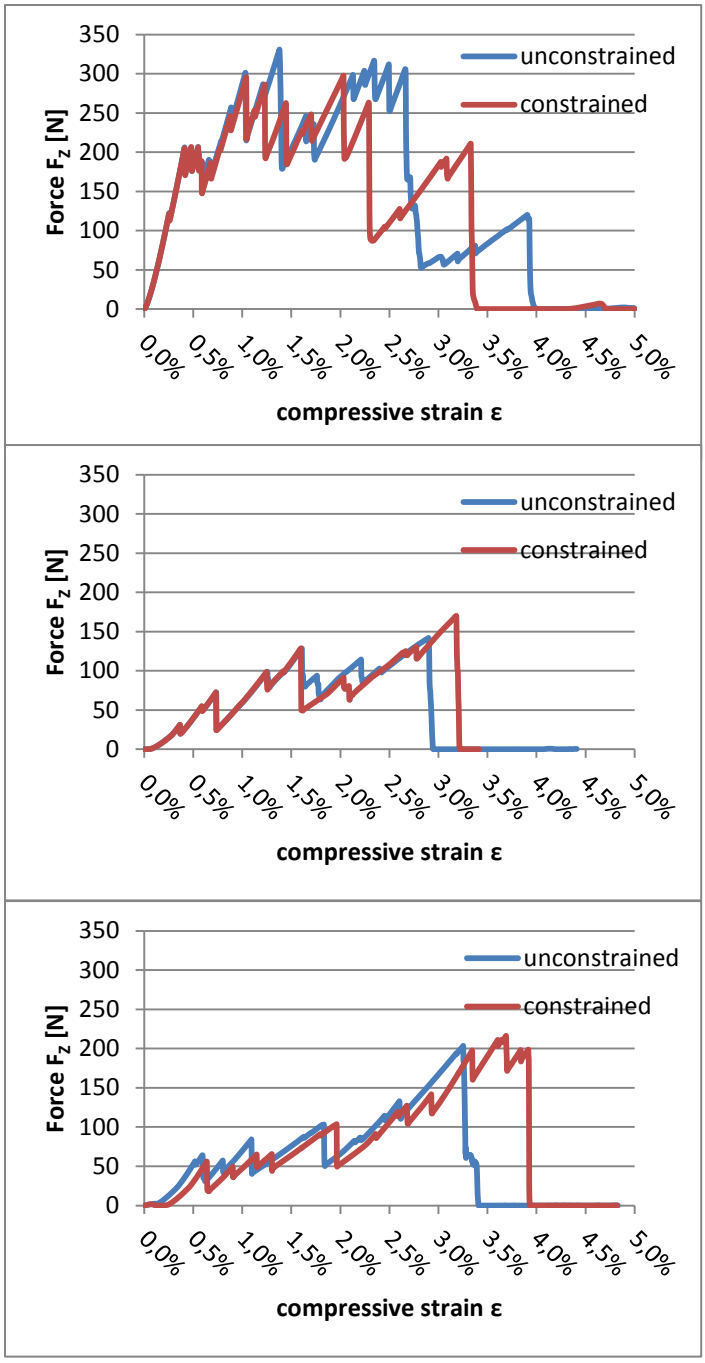


19. Fig.: Corresponding unconstrained and constrained force-displacement diagrams

A clear increase in the force-displacement diagrams was only achieved at higher compressions, see 20. Fig. This is due to the brittleness of the grains: they have to break first, so that the fragments can fill up the voids and develop additional resistance. However, the lateral walls in these tests were only touching the grain and prohibiting lateral extension. They may have a stronger effect when they also exhibit considerable contact forces – i.e. in multi-point loading.

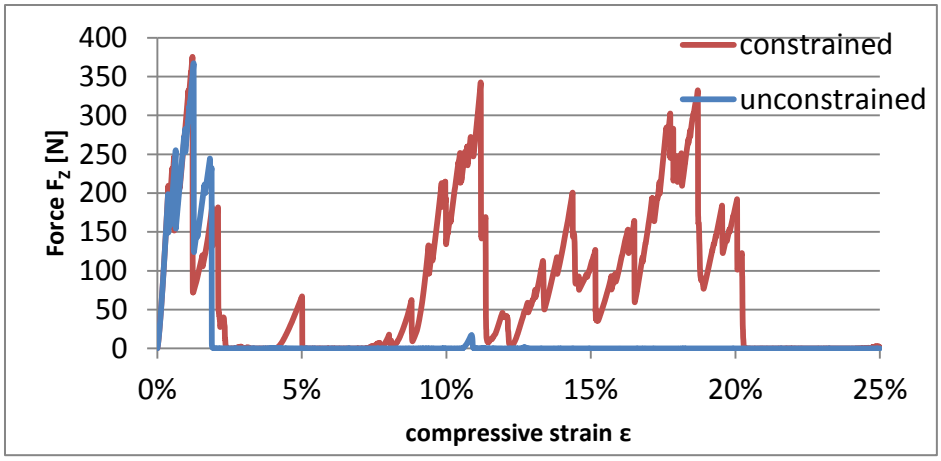


20. Fig.: Crushing tests until larger displacement (ε=25%)

Altogether, the lateral confinement seems to have only little effect on the crushing resistance of the grain, but is important in an ensemble, where the fragments fill the void space and provide additional resistance.

### 3.4.6 Size effect

To investigate the well-known size effect on grain strength, some of the above parameter tests – along with the reference case (3. Table) – were extended to $D_{macro}$=2mm and $D_{macro}$=3mm grains. The tested parameters were:

- normal distribution on bond strengths (Section 3.4.1)
- depleted bonds (Section 3.4.2)
- higher and lower bond strengths (Section 3.4.3)

Alongside the usual survival probability plots and the summary tables, the experienced and expected dependence of grain strength on grain size will be plotted for each case. Here, the expected size effect is assumed to be described by Eq. (2) and is shown in 4. Fig. However, the size effect depends mainly on the evolution of inner flaws in the material, i.e. the distribution of crack sizes and crack propagation. Not all materials follow the Weibull size effect, with experimental evidence presented in (Nakata, Hyde, Hyodo, & Murata, 1999), and theoretical explanation given in (Duxbury, Kim, & Leath, 1994).

The survival probability plots for the reference configurations are shown in 21. Fig., and the relevant parameters are summarized in 9. Table. It can be seen that the mean strengths $\sigma_{mean}$ increase slightly with increasing grain strength – an opposite tendency to what is expected. This tendency is presented in 22. Fig., with the red dots showing the crushing test results, and the Weibull prediction depicted as the blue curve. The Weibull prediction is calculated from $\sigma_0$(3mm) and the average *m* from 9. Table, according to Eq. (2). (It could also be plotted for $\sigma_0$(2mm) or $\sigma_0$(4mm), with similar results.)

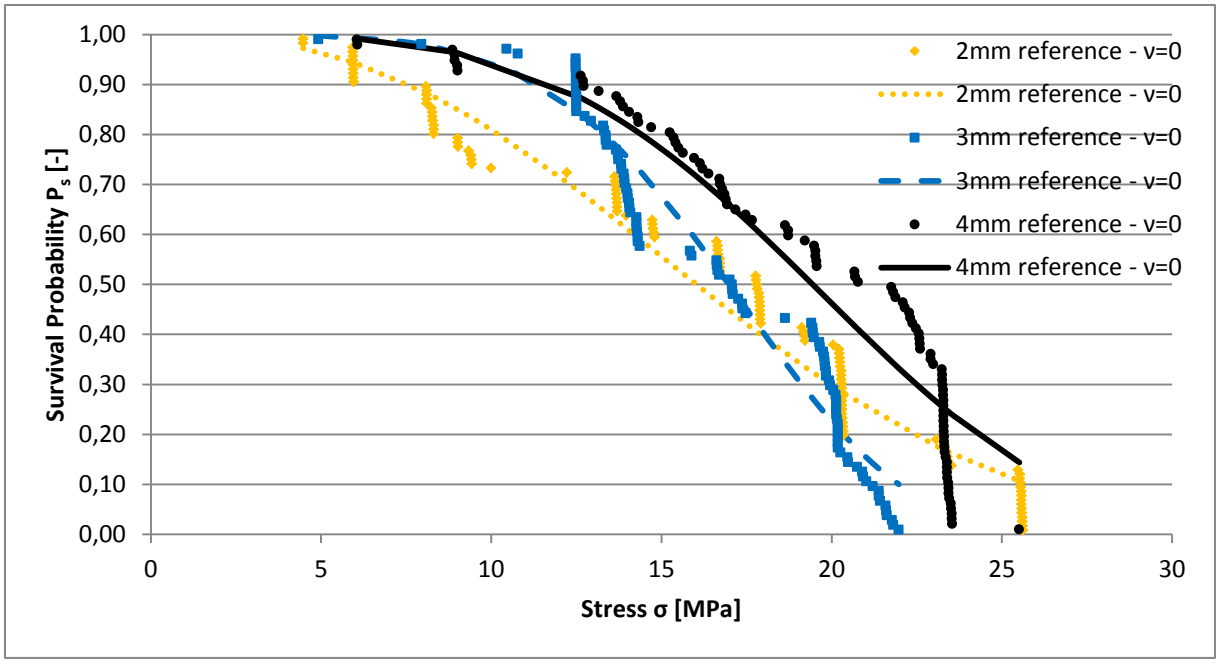


21. Fig.: Crushing test results for $D_{macro}$=2-3-4mm grains, reference cases

9. Table: Crushing test results for $D_{macro}$=2-3-4mm grains, reference cases

| $D_{macro}$ [mm] | Test series | test results | | fitted survival probability function | | | |
|---|---|---|---|---|---|---|---|
| | | n [-] | $\sigma_{mean}$ [MPa] | $\sigma_0$ [MPa] | m [-] | $R^2$ - $P_S$ | $R^2$ - Weib. pl. |
| 4 | reference (v=0) | 96 | 19.22 | 21.42 | 3.78 | 0.907 | 0.918 |
| 3 | | 103 | 16.74 | 18.37 | 4.66 | 0.942 | 0.905 |
| 2 | | 115 | 16.32 | 18.54 | 2.52 | 0.962 | 0.944 |

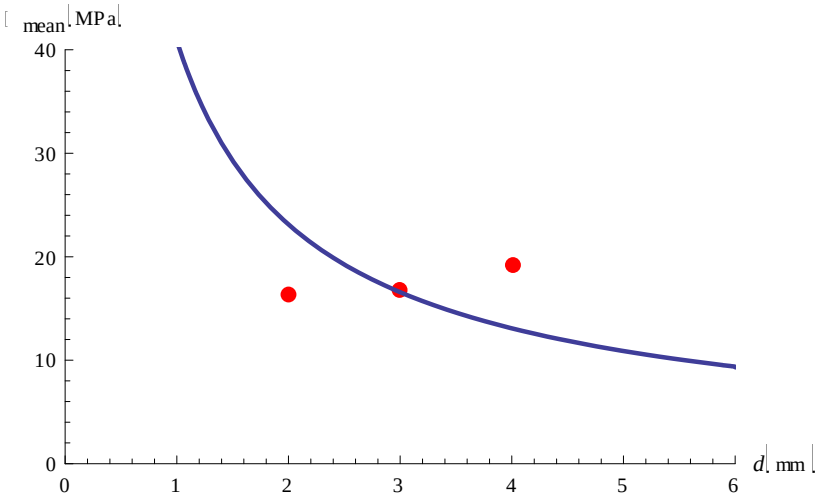


22. Fig.: Size effect in the reference case (red dots: test results, blue curve: Weibull prediction)

The same phenomenon can be observed in Fig. 22-24. for the cases with different normal distributions applied to the bond strengths. The survival probability plots are shown separately for (v=0.10-0.25-0.50), and the parameters are presented numerically in 10. Table. The trends in each case are similar to that observed for the reference case, with the size effect shown in 26. Fig.

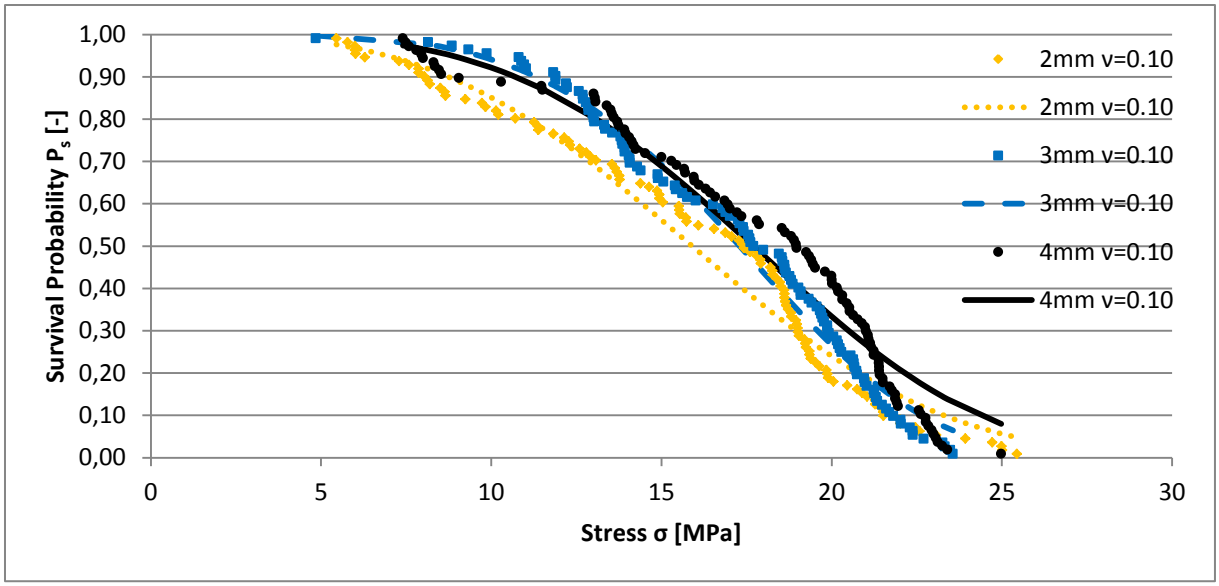


23. Fig.: Crushing test results for $D_{macro}$=2-3-4mm grains, v=0.10

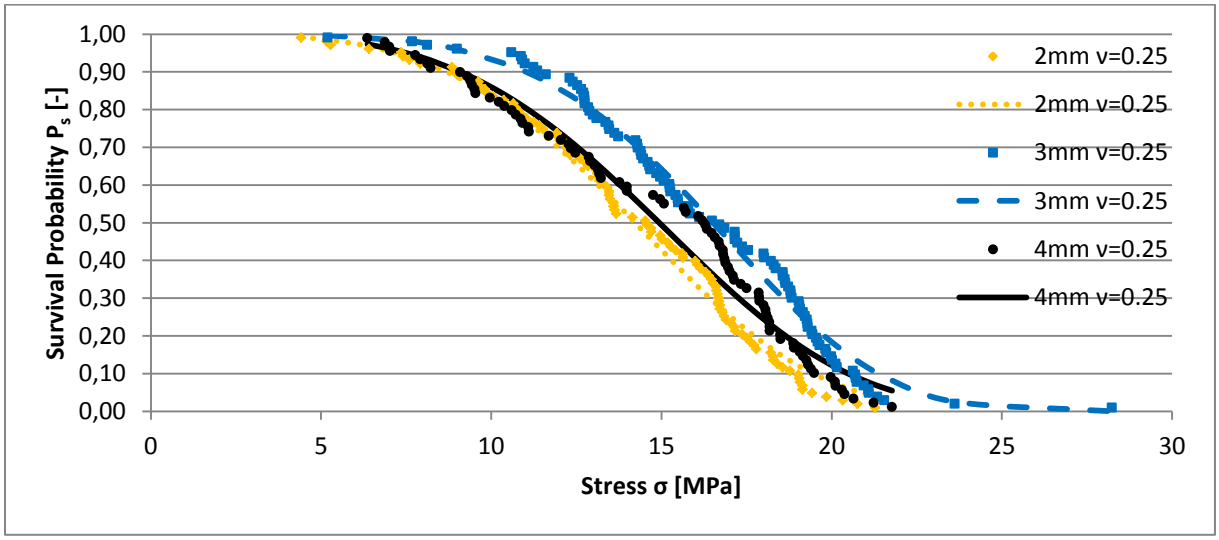


24. Fig.: Crushing test results for $D_{macro}$=2-3-4mm grains, v=0.25

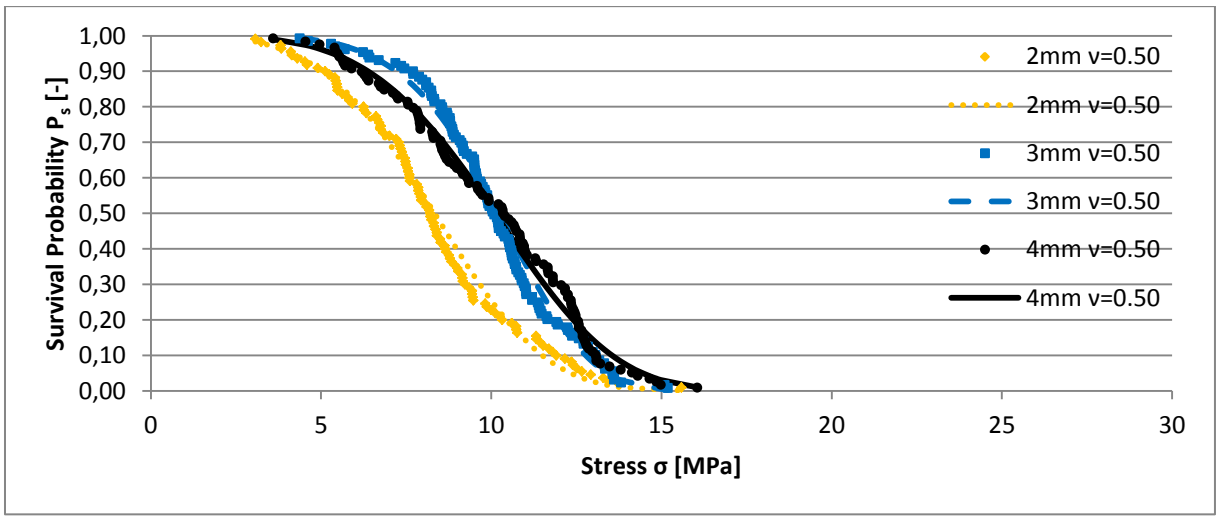


25. Fig.: Crushing test results for $D_{macro}$=2-3-4mm grains, v=0.50

10. Table: Crushing test results for $D_{macro}$=2-3-4mm grains, v=0.10 - 0.25 - 0.50

| $D_{macro}$ | Test series | test results | fitted survival probability function |
|---|---|---|---|

| [mm] | | n [-] | $\sigma_{mean}$ [MPa] | $\sigma_0$ [MPa] | m [-] | $R^2$ - $P_S$ | $R^2$ - Weib. pl. |
|---|---|---|---|---|---|---|---|
| 4 | v=0.10 | 106 | 17.54 | 19.51 | 3.75 | 0.956 | 0.941 |
| 3 | | 110 | 17.10 | 18.78 | 4.45 | 0.981 | 0.969 |
| 2 | | 110 | 15.92 | 17.87 | 3.14 | 0.968 | 0.966 |
| 4 | v=0.25 | 88 | 14.84 | 16.45 | 3.80 | 0.969 | 0.969 |
| 3 | | 102 | 16.32 | 17.86 | 4.66 | 0.986 | 0.971 |
| 2 | | 102 | 14.12 | 15.65 | 3.83 | 0.991 | 0.987 |
| 4 | v=0.50 | 117 | 10.03 | 11.05 | 4.09 | 0.990 | 0.988 |
| 3 | | 128 | 10.10 | 10.95 | 5.39 | 0.987 | 0.985 |
| 2 | | 109 | 8.31 | 9.19 | 3.74 | 0.988 | 0.988 |

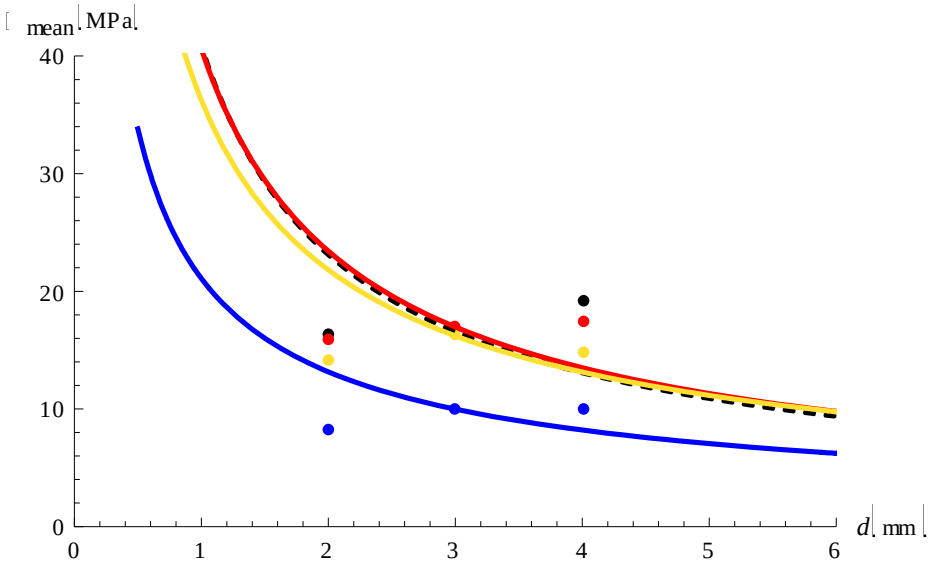


26. Fig.: Size effect in the v=0 - 0.10 - 0.25 - 0.50 cases (black: v=0; red: v=0.10; yellow: v=0.25; blue: v=0.50)

The results for the size effect investigations for the depleted bonds are given in 27. Fig., 28. Fig., 11. Table, and 29. Fig. Generally, the same trends apply as seen in the reference cases and the normal distributions on bond strength.

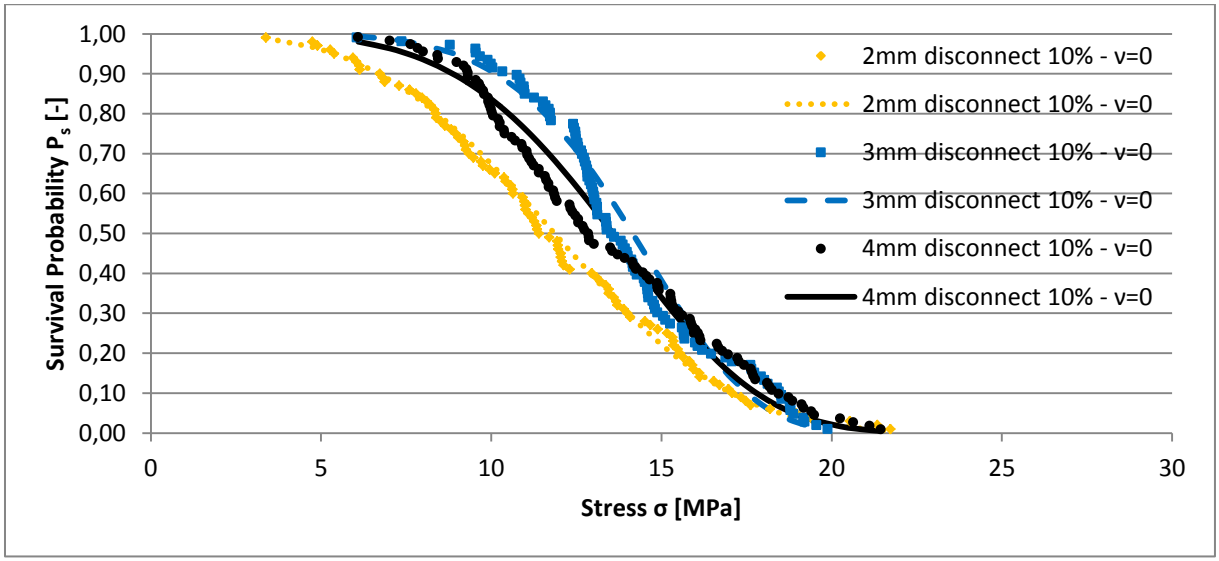


27. Fig.: Crushing test results for $D_{macro}$=2-3-4mm grains, 10% of bonds depleted

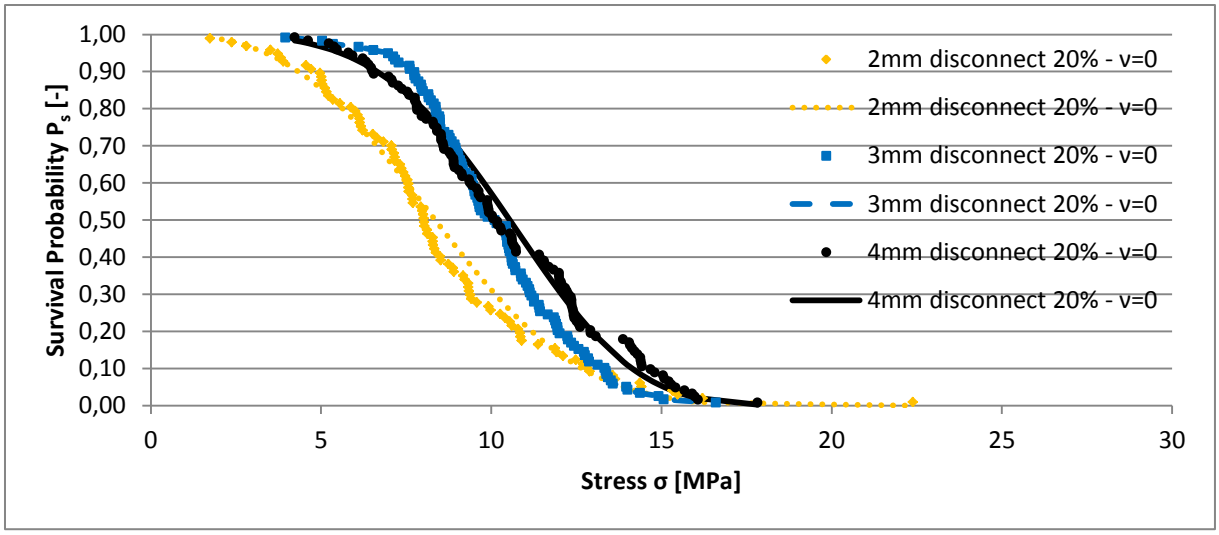


28. Fig. : Crushing test results for $D_{macro}$=2-3-4mm grains, 20% of bonds depleted

11. Table: Crushing test results for $D_{macro}$=2-3-4mm grains, 10% and 20% of bonds depleted

| $D_{macro}$ [mm] | Test series | test results | | fitted survival probability function | | | |
|---|---|---|---|---|---|---|---|
| | | n [-] | $\sigma_{mean}$ [MPa] | $\sigma_0$ [MPa] | m [-] | $R^2$ - $P_S$ | $R^2$ - Weib. pl. |
| 4 | 10% depleted, v=0 | 111 | 13.45 | 14.74 | 4.43 | 0.974 | 0.962 |
| 3 | | 105 | 13.97 | 15.10 | 5.63 | 0.965 | 0.967 |
| 2 | | 99 | 11.89 | 13.25 | 3.30 | 0.996 | 0.994 |
| 4 | 20% depleted, v=0 | 122 | 10.47 | 11.53 | 4.09 | 0.986 | 0.984 |
| 3 | | 117 | 10.16 | 11.03 | 5.24 | 0.987 | 0.977 |
| 2 | | 96 | 8.45 | 9.49 | 2.88 | 0.981 | 0.978 |

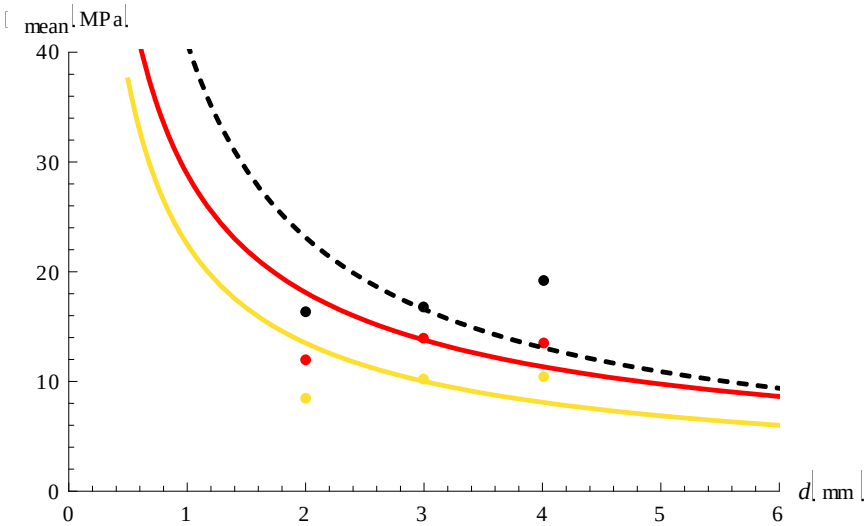


29. Fig.: Size effect in the "0% reference, 10% and 20% of bonds depleted" cases (black: 0% red: 10%; yellow: 20%)

It was seen in Section 3.4.3 that increasing or decreasing the bond strengths affects the grain's crushing strength in the same manner, i.e. doubling the bond strengths leads to a doubled crushing strength. From 30. Fig. it is apparent that the above statement applies for all tested macrograin sizes. The numerical results in 12. Table are in accordance with the observations made for all the other investigated cases: the mean strength of the grains increase slightly with grain size, and the Weibull moduli show the same trend.

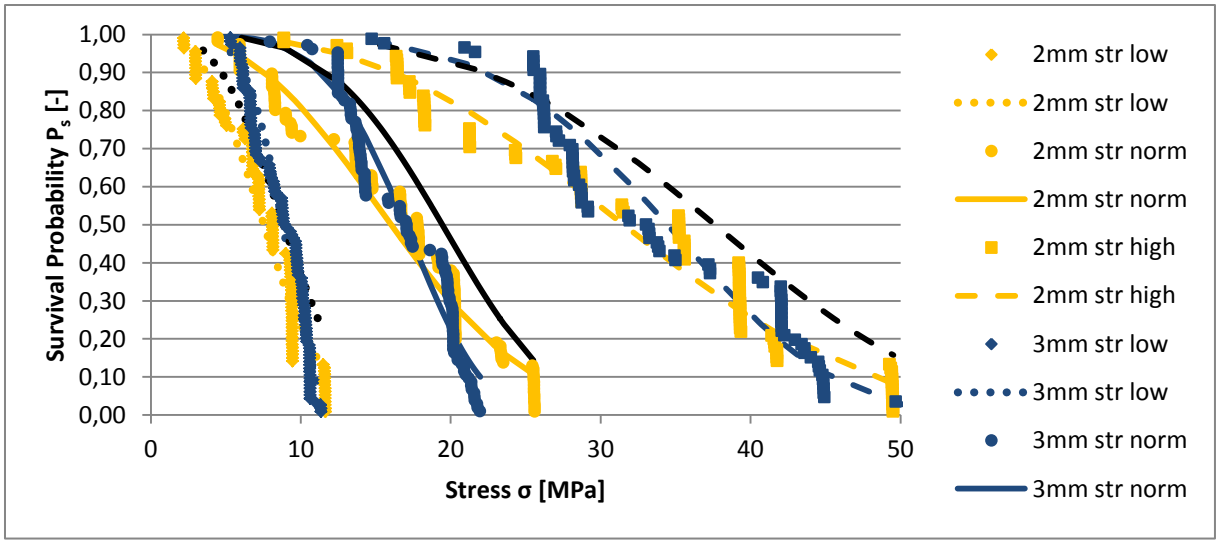


30. Fig.: Crushing test results for $D_{macro}$=2-3-4mm grains; reference, higher and lower bond strengths

12. Table: Crushing test results for $D_{macro}$=2-3-4mm grains; reference, higher and lower bond strengths

| $D_{macro}$ [mm] | Test series | test results | | fitted survival probability function | | | |
|---|---|---|---|---|---|---|---|
| 4 | Normal bond strength; $\sigma_{pb}$=465 MPa (reference) | 96 | 19.22 | 21.42 | 3.78 | 0.907 | 0.918 |
| 3 | | 103 | 16.74 | 18.37 | 4.66 | 0.942 | 0.905 |
| 2 | | 115 | 16.32 | 18.54 | 2.52 | 0.962 | 0.944 |
| 4 | High bond strength; $\sigma_{pb}$=930 MPa | 56 | 37.24 | 41.69 | 3.57 | 0.862 | 0.890 |
| 3 | | 85 | 34.09 | 37.48 | 4.36 | 0.923 | 0.906 |
| 2 | | 104 | 31.83 | 35.89 | 2.83 | 0.962 | 0.954 |
| 4 | Low bond strength; $\sigma_{pb}$=232.5 MPa | 94 | 8.77 | 10.01 | 2.98 | 0.851 | 0.883 |
| 3 | | 113 | 8.67 | 9.42 | 5.33 | 0.943 | 0.914 |
| 2 | | 112 | 7.61 | 8.64 | 2.68 | 0.952 | 0.947 |

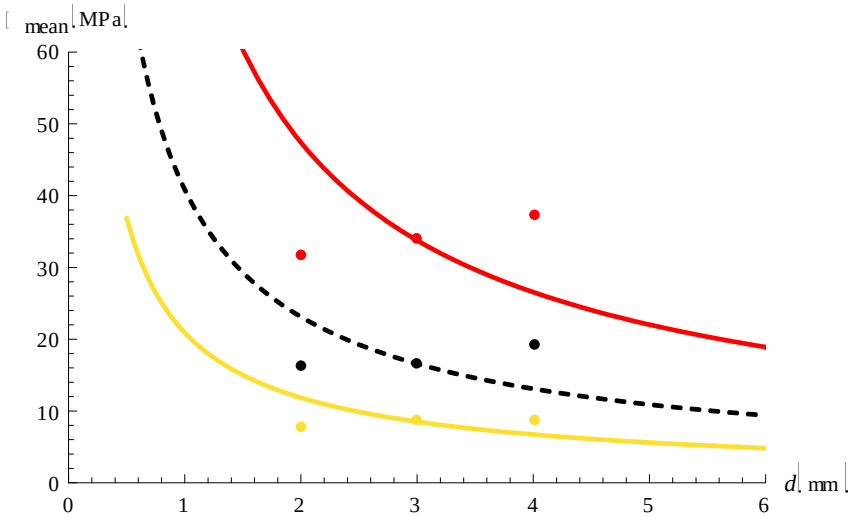


31. Fig. Size effect for normal, high and low bond strengths (black: normal; red: high; yellow: low)

Taking a closer look, a slightly increasing trend for $\sigma_0$ with increasing $D_{macro}$ can be discovered: when evaluating the trend as a power law, we get ≈0.2 for the exponent:

$\sigma_0(d) \approx \sigma_0(d_0)\cdot(d/d_0)^{0.2}$.

In contrast, the size effect included in the Weibull distribution can be expressed as

$$\sigma_0(d) = \sigma_0(d)\cdot\left(\frac{d}{d_0}\right)^{-3/m} \quad (5)$$

In Eq. (5), the exponent -3/m is always negative for any positive m, which leads to a decreasing $\sigma_0(d)$ for increasing d. This is consistent with laboratory evidence (Nakata, Hyde, Hyodo, & Murata, 1999) and theoretical considerations (Duxbury, Kim, & Leath, 1994). The exponent of ≈0.2, derived from the simulations contradicts the latter by predicting increasing grain strength with grain size. (McDowell & Harireche, 2002) found a similar, nonlinear trend in their simulations and proposed to scale the bond strength according to the grain size. Since a grain may undergo repeated crushing in an oedometer test, the scaling had to be applied many times in a crushing process, depending on the current size of the fragments.

Since the authors of this report do not know about a consistent approach for incorporating the proper size effect, and the increasing trend was rather weak for the current macrograins, a simplified approach will be investigated. For most of the oedometer simulations, the same "rule" was applied to the macrograins of all initial sizes, i.e. the same normal distribution, same inner geometry, etc.

The case with "reference" macrograins will then be compared to an oedometer test with the amount of bonds depleted depending on the macrograin's diameter. The following ratios were depleted: Dmacro=2mm – 0%; Dmacro=3mm – 10%; Dmacro=4mm – 2%. Although the evolution of the fragments' strengths will probably not follow Eq. (5), the onset of yielding may be caught more realistically. The mean strengths and the expected strengths after Eq. (5) are shown in 32. Fig.:

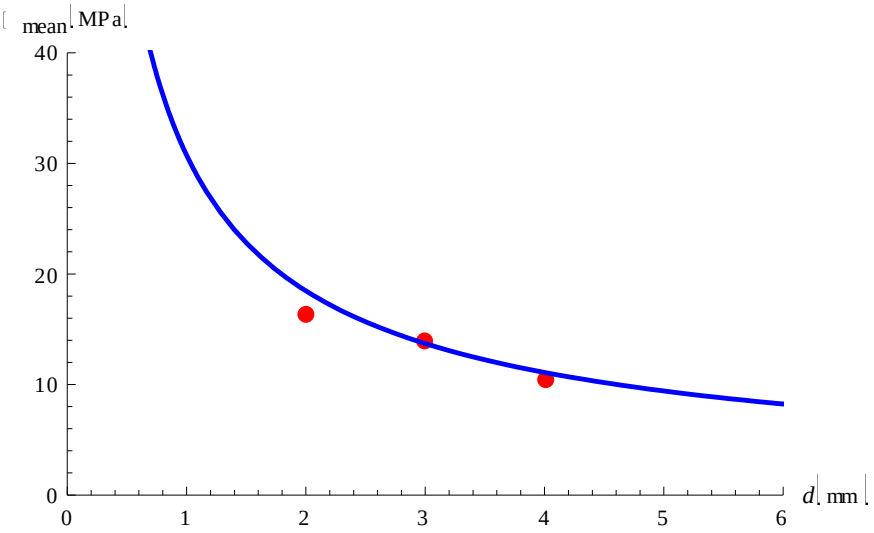


32. Fig.: Size effect for ratio of depleted bonds varying with $D_{macro}$

# 4 Oedometric compression tests

The grains described in the previous two sections were placed into an oedometer for simulating high-pressure compression tests. The aim of these was to investigate the grain crushing process and to study the behaviour of the ensemble at high pressures. The oedometer was box-shaped with a square base of 16mm length, and the starting height also being around 16mm. (The aspect of starting height will be discussed below in more detail.) The oedometric test comprises 2 main phases: the specimen preparation phase and the compression phase.

## 4.1 Specimen preparation phase

The aim of the preparation phase is to produce the starting configuration of the grain ensemble. First, a predefined number of macrograins is placed in a spatial grid above the oedometer base. The

grid ensures that the macrograins are not in contact with each other whilst installing the parallel bonds between the micrograins. The grid cells are cubes with side lengths equal to the maximal macrograin diameter (4mm). They are arranged such that one horizontal row contains the number of cells that fit completely into the base length of the oedometer. The columns extend vertically until the grid provides cells for at least every grain. (However, empty cells may remain at the end of the macrograin generation.) The grid's sketch and the filled cells are shown in33. Fig., parts *a* and *b*.

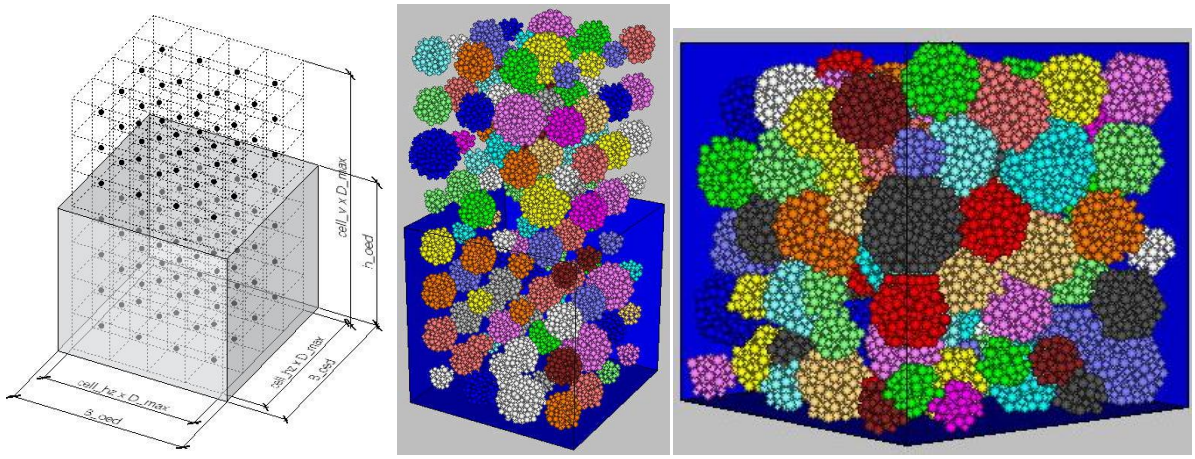


**33. Fig.: Cell grid in the oedometer *a*) cell arrangement; *b*) grid filled with macrograins; *c*) sedimentated specimen**

Once each of the macrograins is placed randomly in the cell centres, they are left to fall into the container. The macrograins are bundled as clumps during the sedimentation, to prevent undue bond failure in this phase. The sedimentation takes place under normal gravity of 9.81 m/s$^2$. However, PFC3D's default local damping ratio of 0.7 was used, which eliminates 70% of the unbalanced force acting on each particle, leaving only 30% of the gravity to act on a grain in free fall. To further smooth the landing of the grains, a viscous damping ratio of 0.9 was used for the contacts, both in compression and shear. The damping properties are computed for each contact such that it equals to 90% of the critical damping coefficient. A detailed description of local and viscous damping in PFC3D is given in (Itasca, 2003).

The sedimentation process ends if the ensemble reaches equilibrium. If either the ratio of maximal unbalanced force to the maximal contact force, or the average unbalanced force to average contact force drops below $10^{-4}$ during the calculation (i.e. the max./average unbalanced force in the system is smaller than 0,01% of the max./average contact force), it is considered as the equilibrium state. Here, a manual check is important in order to verify that the reached state is stable. (This is similar to the equilibrium point of a simple, harmonic oscillator, where the acceleration – and the force – is zero, but the state is not stable.) Since both gravity and damping are active during the sedimentation, a stable state is eventually reached, but – as was the case in some of the calculations – unstable states may also be attained before. (To avoid the system to be "trapped" in such a state, additional calculation cycles need to be carried out. If the ratio of max./average unbalanced force to max./average contact force further converges to 0, then the stable equilibrium state is reached. If it rises again above $10^{-4}$, then the reached equilibrium state was unstable, and the calculation must proceed.)

To ensure a good contact and zero stress, the top platen is placed such that it touches upon the uppermost micrograin. In this position, the top platen is stress-free, and the ensemble is only loaded by its self-weight. At this point, the surface of the specimen is rather uneven, with large voids

eventually present around the oedometer corners and edges. If so, there's a possibility to manually add macrograins to fill these voids and ensure a compact packing. In this case, the specimen is again stepped to equilibrium. A sedimentated specimen is shown in 33. Fig., part *c*.

As the last step of the preparation phase, the parallel bond properties may be modified. (E.g. by applying a normal distribution to the bond strengths, depleting some bonds, etc.) The bundling of the micrograins into clumps is lifted, and the viscous damping is set to 0. (For comparison, one compression test was conducted with the viscous damping set to 0.5 for the compression phase – the results will be discussed later.)

The grain size distribution of the specimen is shown in 34. Fig., with the diagram divided into fractions used in soil mechanics. The blue and purple curves show the initial grain size distributions: the manually-placed small grains ($D_{macro}$=2mm) account for the higher fine fraction of the purple curve. The shaded area to the right of the red curve shows the possible range of grain size distributions with the current micrograins, i.e. the red curve is the comminution limit. The initial curves are gap-graded, since they contain only 2mm, 3mm, and 4mm macrograins, each with exactly the same geometry. The number of macro- and micrograins in the different specimens tested are shown in 13. Table.

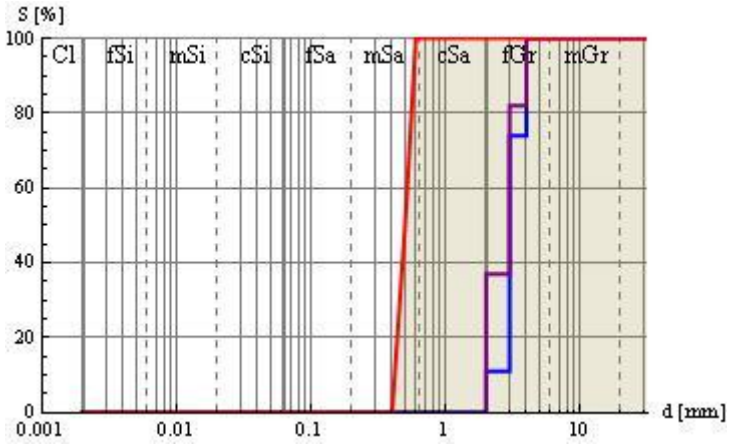


34. Fig.: Grain size distributions in the oedometer tests

13. Table: Overview of macro- and micrograin numbers, initial heights

| Specimen | Number of macrograins | | | | Overall nr. of micrograins | initial height $h_0$ [mm] | initial core void ratio $e_{core}$ [-] |
|---|---|---|---|---|---|---|---|
| | $D_{macro}$ = 2 mm | $D_{macro}$ = 3 mm | $D_{macro}$ = 4 mm | Overall | | | |
| Fric. 0.55 – dense | 196 | 70 | 12 | 278 | 24 638 | 20.5 | 2.05 |
| Fric. 0.55 – loose | 40 | 70 | 12 | 122 | 17 150 | 17.6 | 2.56 |
| Fric. 0.55 – 4x res. | 40 | 70 | 12 | 122 | 81 520 | 16.0 | |
| Fric. 0.4 | 40 | 70 | 12 | 122 | 17 150 | | |
| Fric. 0.3 | | | | | | | |
| Fric. 0.2 | | | | | | 17.2 | |
| Fric. 0.0 | | | | | | 17.9 | 2.49 |

## 4.2 Compression phase

When the specimen is prepared – equilibrium reached, bond properties set, clumps released and top platen being in position – the sequence of compression steps is started. A compression step

comprises 2 substeps: actual loading and subsequent equilibration, with the parameters given in 14. Table:

14. Table: parameters of a single compression step

| **I. loading substep** | | **II. equilibration substep** | |
|---|---|---|---|
| length of timesteps | $10^{-6}$ s | length of timesteps | $10^{-6}$ s |
| calculation cycles | 20 000 | calculation cycles | 2 000 |
| duration | 0,02 s | duration | 0,002 s |
| top platen velocity | 8 mm/s | top platen velocity | 0 mm/s |
| compression | 0,16 mm | | |

The compression steps are repeated until the specimen reaches a height of $0.375 \cdot h_0$ ($h_0$ being the specimen's initial height), requiring usually 70-90 steps, depending on $h_0$. This is sufficient to surpass the point where the initial macrograins are broken down almost completely into individual micrograins, and from where the densification of the ensemble is controlled by the elastic compression of the micrograins. It must be noted however that the model loses its validity at this point, since contact forces and stresses may increase unlimitedly – a feature that contradicts the behaviour of real grains. Although Eq. (5) predicts $\lim_{d \to 0} \sigma_0(d) = \infty$, very small particles are squashed plastically, instead of splitting. (Kendall, 1978)

The oedometer walls are considered completely stiff – as noted in Section 1.2 – and only the friction coefficient needs to be defined. In the current model, it was set to 0. The reason for this was prevent shear forces and – using continuum-mechanical terminology – shear strains to develop along the 16mm wide walls, which are rather narrow compared to the maximal macrograin diameter of 4mm. (As a minimum, $D_{oed}=10 \cdot D_{max}$, $h_{oed}=5 \cdot D_{max}$ are suggested for representative results.) This way the axis-symmetric, practically linear strain conditions in the core of a real oedometer are better reproduced. Nevertheless, friction also appears along the walls of a real oedometer, but with a boundary disturbance-character and has a rather low impact in the specimen's centre. The zero friction was also applied to the top and bottom platens.

During the compression phase, the following properties were recorded: actual specimen height; void ratio; stresses acting on the walls; ratio of broken bonds due to normal and shear stresses; number of micrograin contacts with the top platen; difference between vertical stresses on the lower and upper platen; energy and work quantities. The sampling frequency was 1000 steps, i.e. $10^{-3}$ s, resulting in ≈1800-2200 data points recorded during each compression test.
The void ratio was calculated in 2 ways:

- Overall void ratio: from the volume of all micrograins and the actual oedometer volume. It also contains the effect of larger void space along the oedometer's edges, and the inner voids of the macrograins.
- Core void ratio: using PFC3D's measurement functions, the void ratio in a "control volume" or core was recorded. The core was a sphere with a diameter half of the actual oedometer height (shrinking with decreasing specimen height), centred inside the oedometer. This allows the exclusion of disturbed boundary zones with high void volume. The core is shown in 35. Fig.:

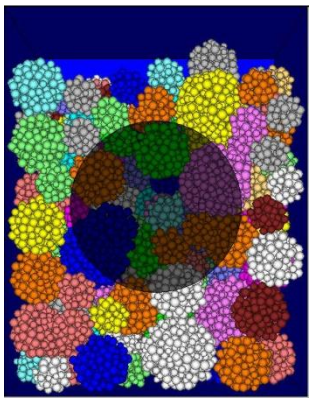

35. Fig.: Specimen's core (shaded, spherical)

The following energy and work quantities were traced:

- Boundary work (of the top platen)
- Kinetic energy of the ensemble
- Strain energy stored in the micrograins and in the parallel bonds
- Frictional work dissipated in the contacts

## 4.3 Evaluation of the compression phase results

The main aspects of the oedometric compression test in this research were the compression curve (e- lg$\sigma_z$ or e- lg(3$p_s$)) and the evolution of grain crushing, expressed as the ratio of broken bonds. These are shown in 36. Fig.for the dense specimen, with "reference" macrograin properties given in 3. Table.

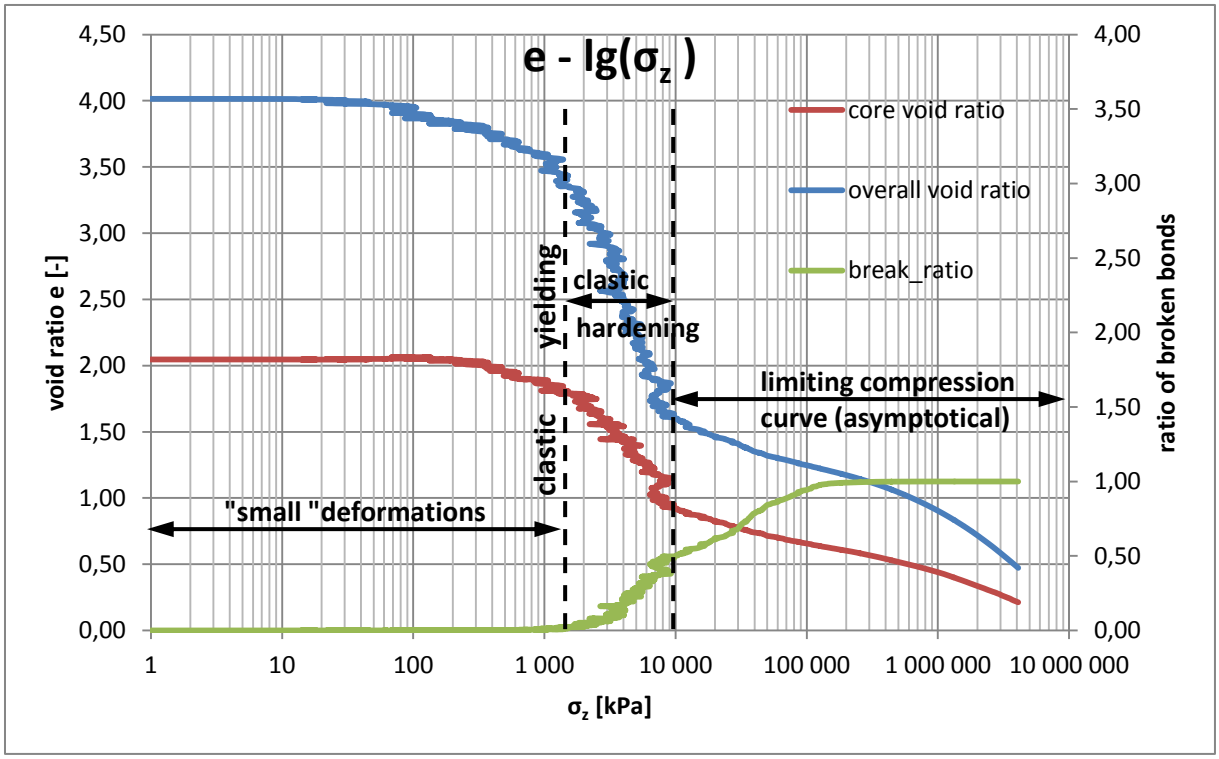


36. Fig.: void ratios and ratio of broken bonds against the vertical stress for the „reference" dense specimen

36. Fig. shows similar compression curves to those obtained from experiments by e.g. Bauer 1992, (Nakata, Hyodo, Hyde, Kato, & Murata, 2001), (Uygar & Doven, 2006), and (Guimaraes, Valdes, Palomino, & Santamarina, 2007). The curves for the overall and core void ratios are proportional, but

the overall void ratio is much higher due to the gaps along the specimen boundaries. (With a much larger specimen, the overall void ratio would lie closer to the core void ratio.) The compression curves can be divided into 3 distinct phases, as described in (Bolton & McDowell, 1997) or (Uygar & Doven, 2006):

- small deformation or “elastic stiffening” phase until clastic yielding
- clastic hardening or “normal compression”, after clastic yielding, and
- limiting compression curve (approached asymptotically)

The ratio of broken bonds shows a similar evolution to the compression curves: its gradients are proportional to the gradients of the compression curves. This indicates that grain crushing and the slope of the compression curve are closely related.

To validate the parameters of the crushing process and the loadsteps, a similar procedure was applied as described in Section 3.3, at the single macrograin crushing tests. Here, the “loose” specimen (13. Table) was compressed with a smaller timestep: instead of $10^{-6}$ s (14. Table) it was set to $10^{-7}$ s; the initial conditions and all other parameters were not changed. This test will be referred to as “small timestep” below.

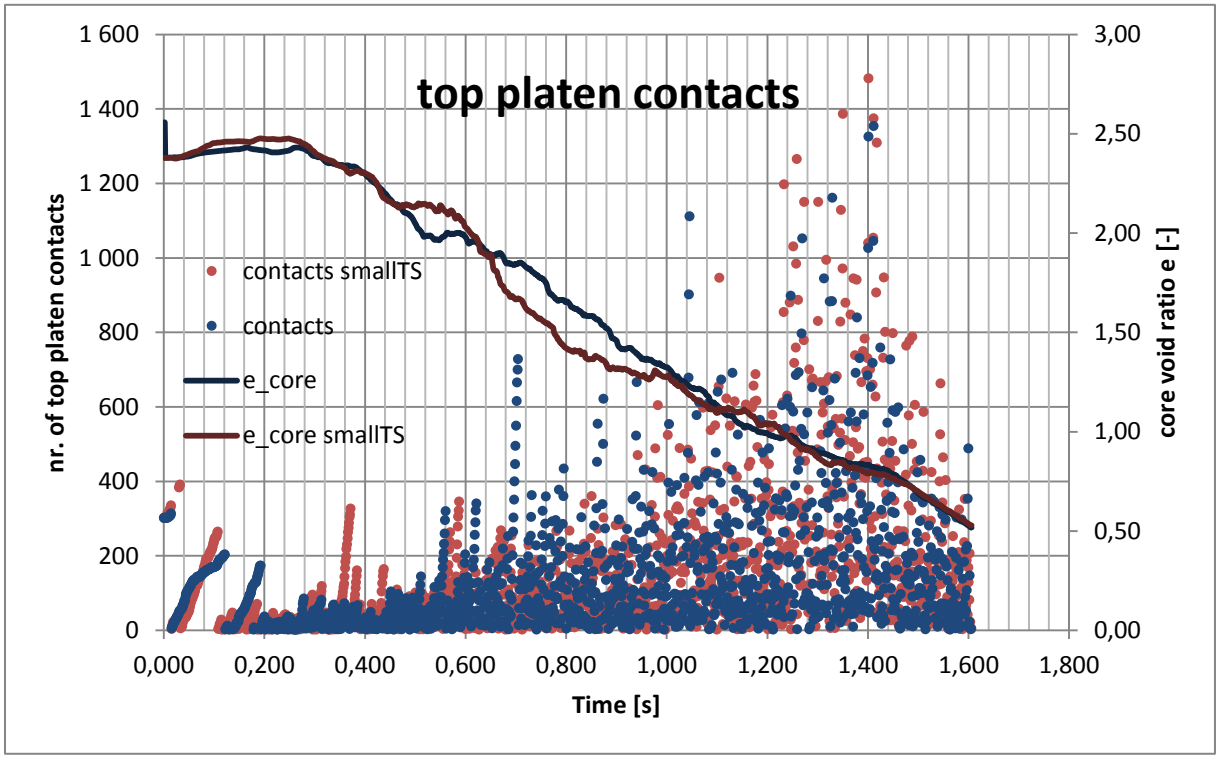


**37. Fig.: Number of particle contacts with the top platen (dots, left vertical axis), and core void ratio (line, right vertical axis) against time**

37. Fig. shows the number of particle contacts with the top platen, plotted against time elapsed since the start of the compression process. The evolution of the core is also indicated. Both the number of contacts and the evolution of the core void ratio show similar “trends” in each case. This means that the kinematics of the process is the same in both cases. First, when the densification is primarily governed by grain rearrangement, there are fewer contacts with the top platen. Later, when grain crushing becomes dominant, the number of contact increases and varies over a wide range. This is more pronounced in 38. Fig., when plotting the number of contacts against the mean vertical stress.

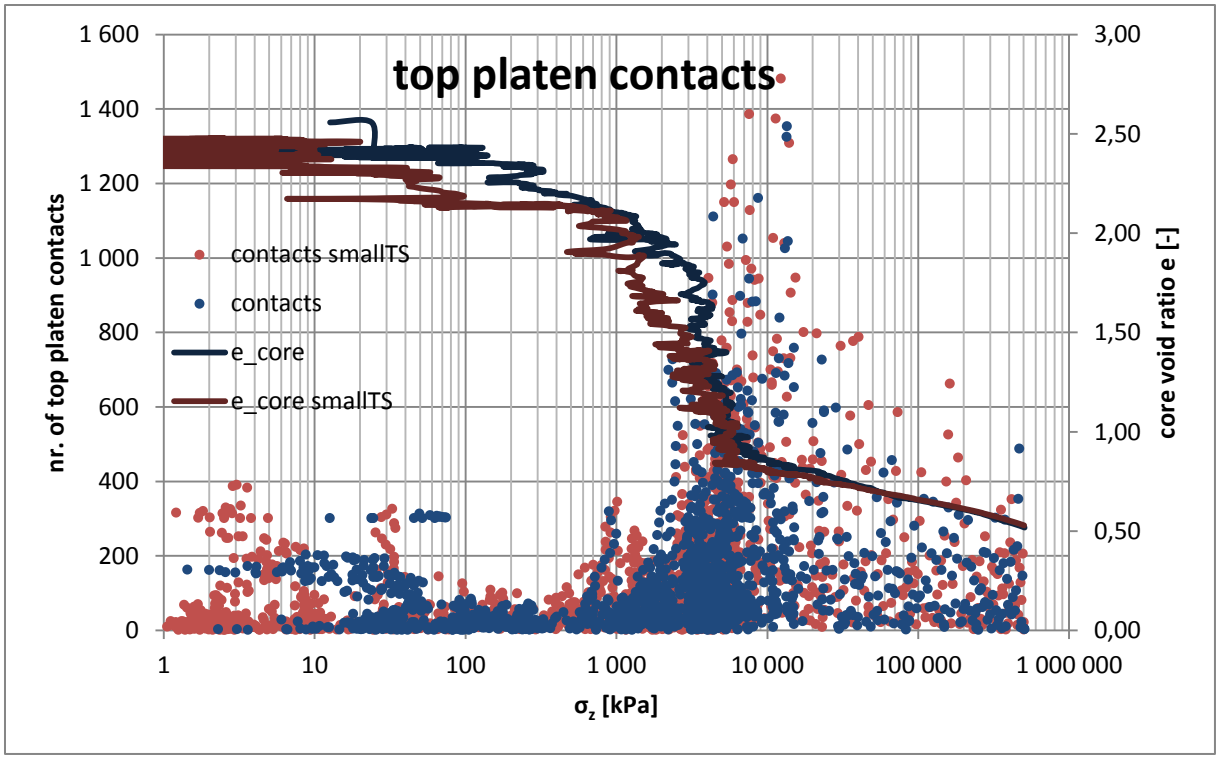


38. Fig.: Number of top platen contacts (left axis) and core void ratio (right axis) against vertical pressure

The (mean) vertical stress $\sigma_z$ is calculated as

$$\sigma_z = \frac{F_{top} + |F_{bottom}|}{2 \cdot A_{base}} \qquad (6)$$

where $F_{top}$ and $F_{bottom}$ are the vertical forces acting on the top and base platens. If the specimen is compressed, $F_{top}$ points towards the positive z-direction, and $F_{bottom}$ towards the negative, hence the absolute value. The compressive stress is taken to be positive. Since the micrograin-wall contact cannot sustain tension, $F_{bottom}$ will always be non-positive, and both $F_{top}$ and $|F_{bottom}|$ non-negative. Compressive stress is also taken to be positive.

One requirement of the quasi-static loading process is that the forces $F_{top}$ and $F_{bottom}$ should be almost identical in value (more precisely: $|F_{bottom}| = F_{top}$ + specimen weight). One way to introduce the "pressure difference" is

$$\Delta\sigma_z = \frac{|F_{bottom}| - F_{top}}{A_{base}} \qquad (7)$$

and the requirement for the quasi-static process may be formulated for high stresses ($\sigma_z \gg$ specimen weight ) more conveniently as the ratio of "pressure difference" to mean pressure:

$$\Delta\sigma_z/\sigma_z \to 0$$

The latter is shown in 39. Fig. for the reference and small timestep cases. It can be seen that in both cases, $\Delta\sigma_z/\sigma_z$ approaches zero from below. From the definition of $\Delta\sigma_z$ it follows that in such cases ($\Delta\sigma_z < 0$) the pressure is larger on the top platen than on the bottom of the oedometer. Unlike in the reference case, the difference in the small timestep case remains rather low throughout the whole loading process (although some scatter at the beginning is visible).

The scatter is very high in the reference case, especially in the "elastic stiffening" regime. Here, values for $\Delta\sigma_z/\sigma_z$ even reach -2, which is the lower limit, meaning that the grains detach from the

upper platen: $F_{top}$=0. During the “clastic hardening” phase, the scatter reduces, and on the “limiting compression curve” it converges to 0 from below.

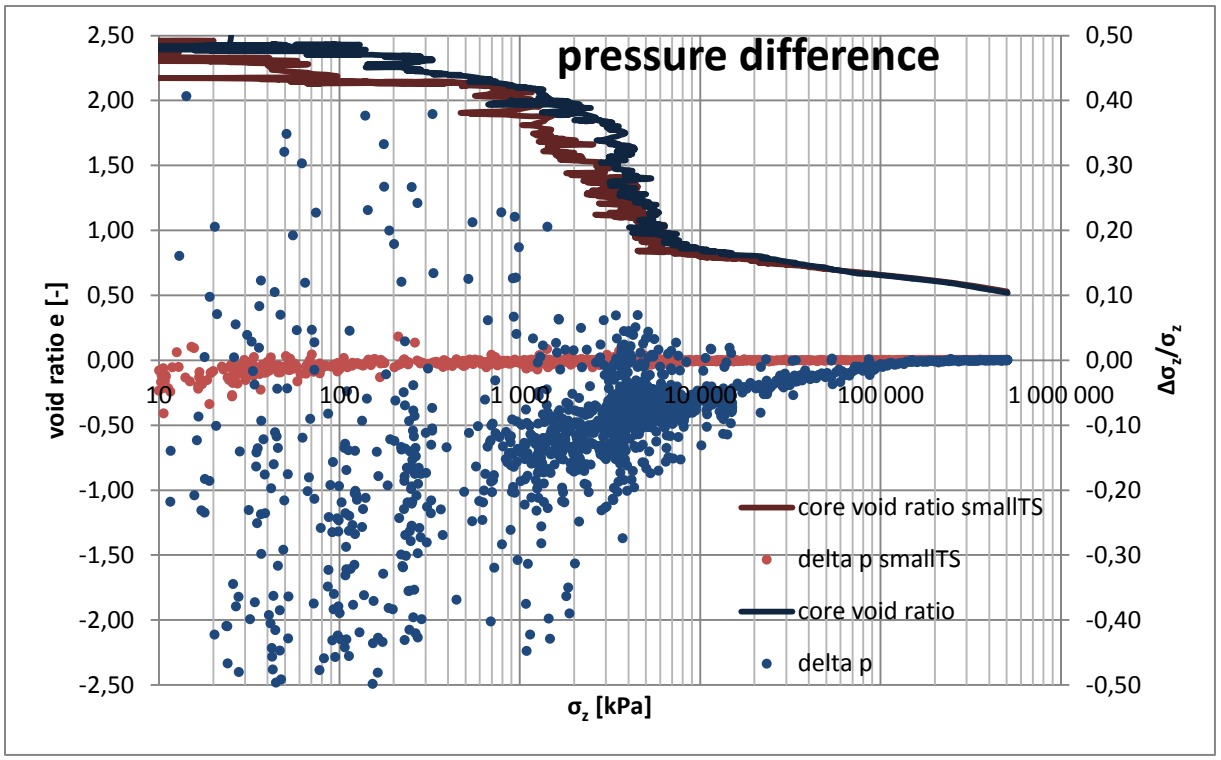


39. Fig.: "pressure difference" and core void ratios against lg($\sigma_z$), for reference and small timestep cases

In our opinion, the “pressure difference” between the top and bottom platens may be explained as follows. After the sedimentation of the specimen, the grain skeleton forms a stable structure, supported by the base platen and side walls. The number of contacts and the position of the grains is more or less stable, resulting in small variations due to grain rearrangement in the specimen. On the other hand, the top platen is placed such that it touches on the uppermost micrograin, without imposing contact forces. The surface of the sample is rather uneven. As the platen advances downward, it causes the adjacent grains to rearrange by a series of collisions and rebounds. This is reflected in the varying number of contacts, as well as in the “pressure difference” between the top and bottom platens. The higher “pressure difference” for the loading process with “reference” timesteps comes from the larger timestep itself: for the same advancement rate of the top platen, the displacement in a single timestep was 10x greater than in the “small timestep” case. When the downward-moving platen comes in contact with a steady or upward-moving particle, the overlap created in the contact is much greater than in the “small timestep” case. After (Itasca, 2003) the contact normal force is given by

$$F^n = \frac{2\bar{G}\sqrt{2\bar{R}}}{3(1-\bar{\nu})} \cdot U^{3/2} \qquad (8)$$

where U is the overlap in the contact. In a newly-formed contact, if for example $U=10 \cdot U_{small}$ ($U_{small}$ would be the overlap in the “small timestep” case), then $F^n \approx 31 \cdot F^n_{small}$, resulting in larger contact forces and consecutively larger vertical stress. This effect is important when there is significant grain rearrangement, i.e. before “limiting compression curve”. This may be the most plausible explanation for the shift between the compression curves in 37. Fig. - 39. Fig.

Another question to be addressed is the origin of the "oscillation" of the compression curves. It is understood that after impact, density waves travel not only in solid, but also in granular systems. On the other hand, the oscillation may also arise due to stress relaxation after grain rearrangement and crushing.

To investigate this, an additional test was conducted along the aforementioned "reference" test for the dense specimen. The additional test had the same parameters as the "reference" configuration, but the viscous (contact) damping was set to 0.5 to reduce the rebound effect after particle collisions. Since the outcome of a compression test is influenced by small perturbations of the ensemble – e.g. through numerical errors –, the "reference" test was re-run 3 times, which resulted rather in a "band" for the compression curve than in exactly the same curve. The compression curves for the reference tests nr. 1-3 and for the test with contact damping are shown in 40. Fig.

As it can be seen from 40. Fig., the "oscillation" of the compression curves did not change significantly after introducing the viscous damping into the system.

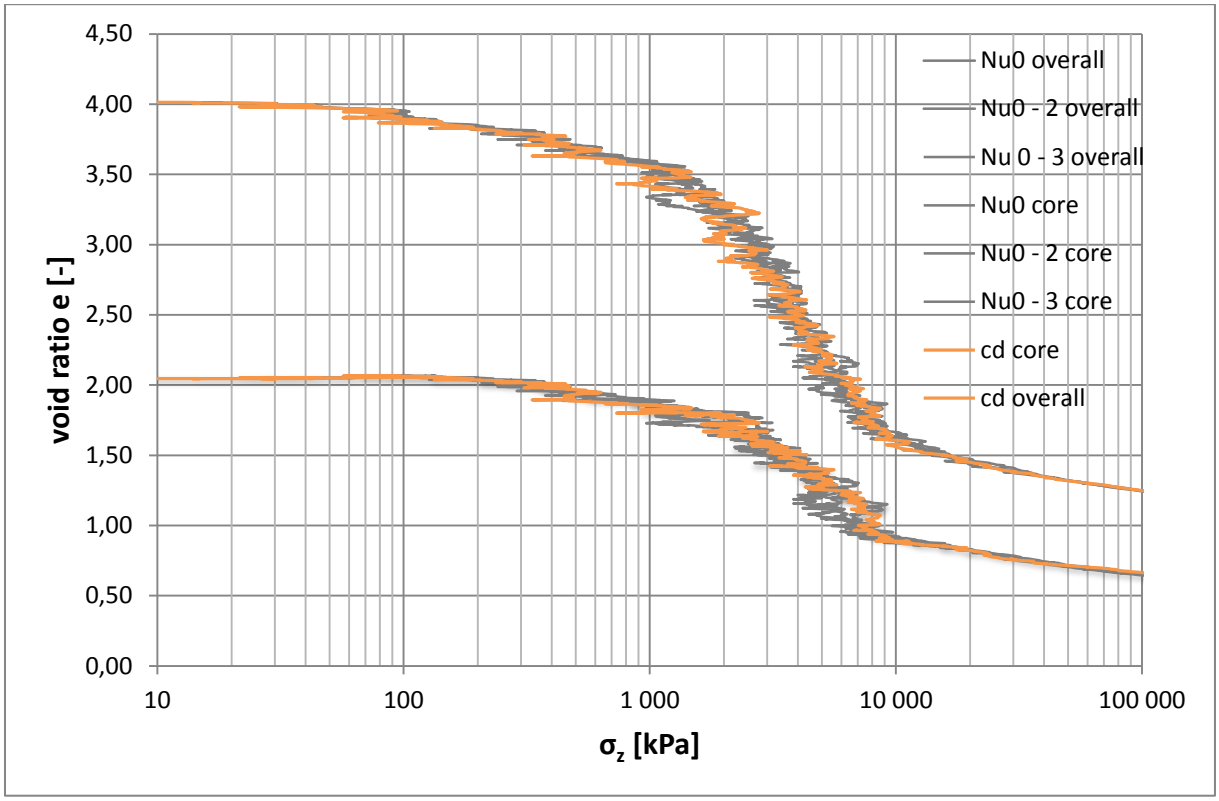


**40. Fig.: compression curves (overall and core void ratios) for the dense specimen: "reference" cases 1-3 and "contact damping" case, marked as 'cd'. (Grey: reference cases, orange: contact damping case)**

Observing the pressures on the top and bottom platens against time also shows strong oscillations: 41. Fig. and 42. Fig. show the aforementioned plots for the loose ensemble, "reference" and "small" timesteps. It can be seen that – as expected – the top pressure is higher almost every time in the "reference" timestep case, while the difference is vanishingly little in the "small timestep" case. The fine resolution in 42. Fig. shows that the curves for top and bottom pressures in the "reference" case are affine, but the bottom pressure curve does not exhibit the small local peaks seen on the top pressure curve, it follows the top curve rather smoothly. In accordance with the explanation given for the pressure differences above, the reason for this may be that the energy of small density waves – starting from the top platen – is easily dissipated by the friction between the grains, whereas larger waves – caused by larger rearrangement – are able to reach the bottom plate. Judged by the

corresponding curves for the “small timestep” simulation, the density wave takes less than $10^{-3}$ s (one sampling interval) to travel through the specimen. The pressure plots in 41. Fig. show rather stochastic than harmonic oscillations, which implies that these are caused primarily by grain rearrangement and breakage, rather than by reflected waves.

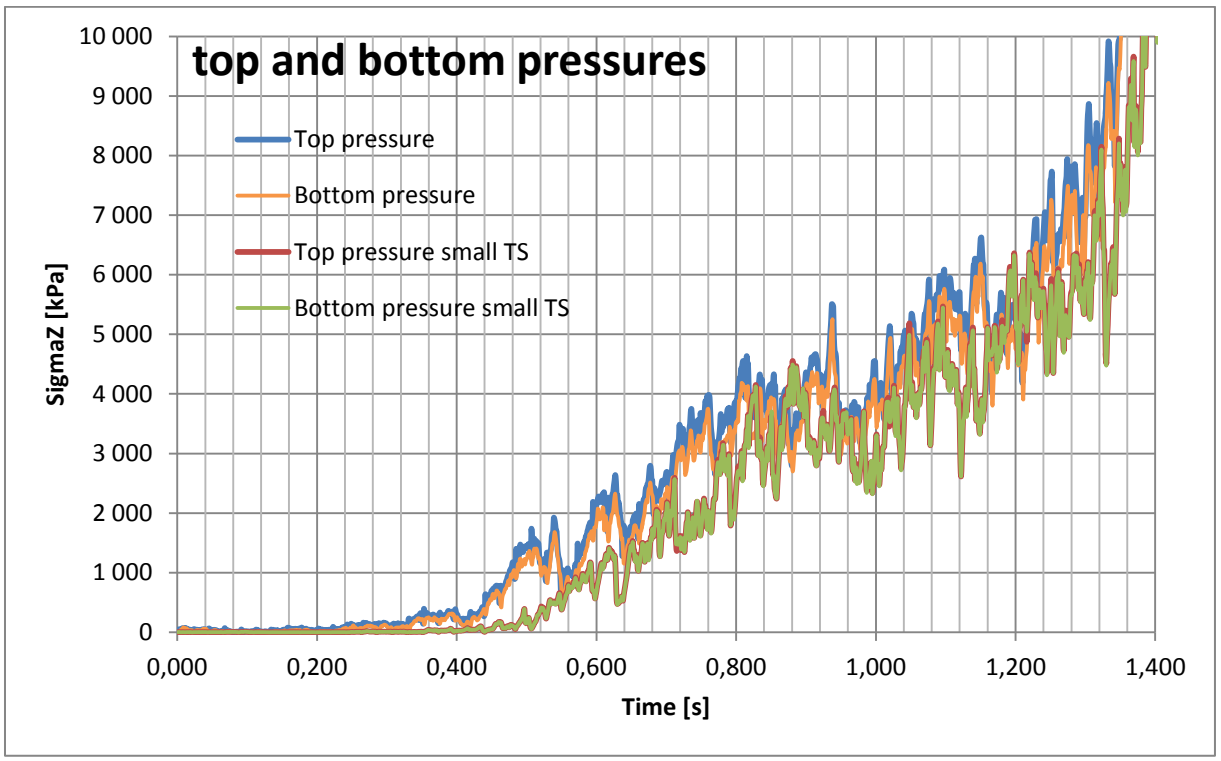


41. Fig.: top and bottom pressures against time for the loose ensemble, reference and small timesteps

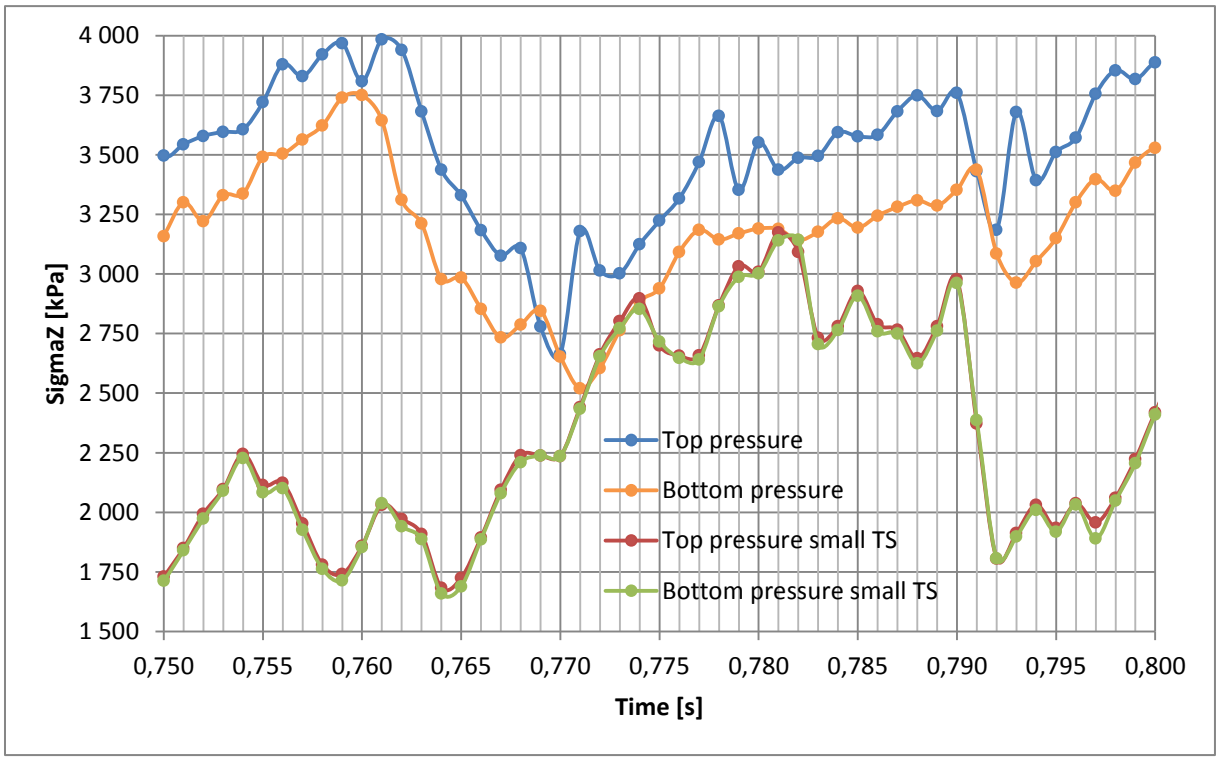


42. Fig.: magnification of the top and bottom pressures curves from 41. Fig.

The fact that such oscillations were not observed in real compression tests may be explained by a number of reasons:

- The number of grains in real samples is by orders of magnitude higher than in these simulations. The higher number of contacts would lead to a smoother overall pressure on a platen, since local extremes in the pressure distribution could bias the average pressure in a lesser extent.
- The pressure in real tests is not measured directly on the contact plane of the grains and the platen, but rather by different auxiliary measures (e.g. height of the water column in a triaxial test in displacement-controlled tests), which introduces significant damping to the measurements. This would "blend" such oscillations into a smooth average. Furthermore, oedometric compression tests are very often stress-controlled.
- The reading intervals of real tests are much longer, usually the reading is taken when the specimen has reached a steady state. This contrasts with the current model, where readings were taken at intervals of $10^{-3}$ s, throughout the whole loading process.

To summarize the main points from the above section, it can be stated that:

- The compression curves from the simulated tests qualitatively agree with those observed in real tests
- The 3 domains on the compression curves are closely related to grain crushing and rearrangement: the first domain, "elastic stiffening" is governed by rearrangement, while the "clastic hardening" domain is influenced both by crushing and rearrangement, whereas the "limiting compression curve" depends mainly on grain rearrangement and elastic compression of the grains
- The oscillations of the compression curve are caused by stress-relaxation of the specimen, and density waves do not play a significant role in this subject
- The resulting compression curve is also influenced by numerical issues: the selection of a sufficiently small timestep is essential to properly follow the compression process. It has to be selected (adjusted) corresponding to the compression rate (platen velocity), but also to the size of the particles, and their stiffness, as can be seen from Eq. (8).

By comparing the results of the tests with "reference" parameters and the "small timestep" case, it was found that the selected "reference" timestep of $\Delta t=10^{-6}$ s was too large. It produced significant differences between the pressures on the top and bottom platens, while these vanished for a smaller timestep of $\Delta t=10^{-7}$ s. It also shifted the compression curve to the right on the e-lg($\sigma_z$) plot, while retaining its main features. However, the choosing a timestep of $\Delta t=10^{-6}$ s was necessary due to the tremendous calculation time of the simulation series.

# 5 Results of the oedometer tests

## 5.1 Deformation and displacement patterns

In a relatively loose grain ensemble, densification happens mainly due to the rearrangement of the grains. (Oldecop & Alonso, 2007) This is also followed by formation and decay of force chains between the grains. The force chains decay due to "buckling" of the grains which form the grain skeleton. (Gudehus, 2011, old.: 19 (4))

If the ensemble gets denser, the force chains lose their stability less and less easily, and larger contact forces may develop. Eventually, the system gets "locked", with no further densification possible without the breakage of some grains. Then, if a grain on a force chain breaks, the force chain is transferred to another path, followed by the rearrangement of the grain skeleton.
On a microscopic level – for a volume smaller than the representative volume element – the displacements and rotations of the grains are highly heterogeneous.

The displacement of the macrograins was examined during the compression phase. Besides the well-known, heterogeneous displacement field, the following observation was made.

In the initial configuration, when the top platen is placed upon the uppermost micrograin without applying any force to the grains, the surface of the specimen is not even. Upon first loading, the uppermost macrograin penetrates the specimen below, and the other macrograins on the surface are pushed aside and upward. This continues until the penetrating macrograin gets immersed, and the top platen catches up with the other macrograins too.
In a case where a single macrograin got trapped on top of the rest of the ensemble, the penetration can be followed both visually (not presented here), and on the initial part of the core void ratio plot (43. Fig.).The latter confirms that some dilatancy happens in this first phase, and the actual compression starts later, from the "top" of the void ratio curve.

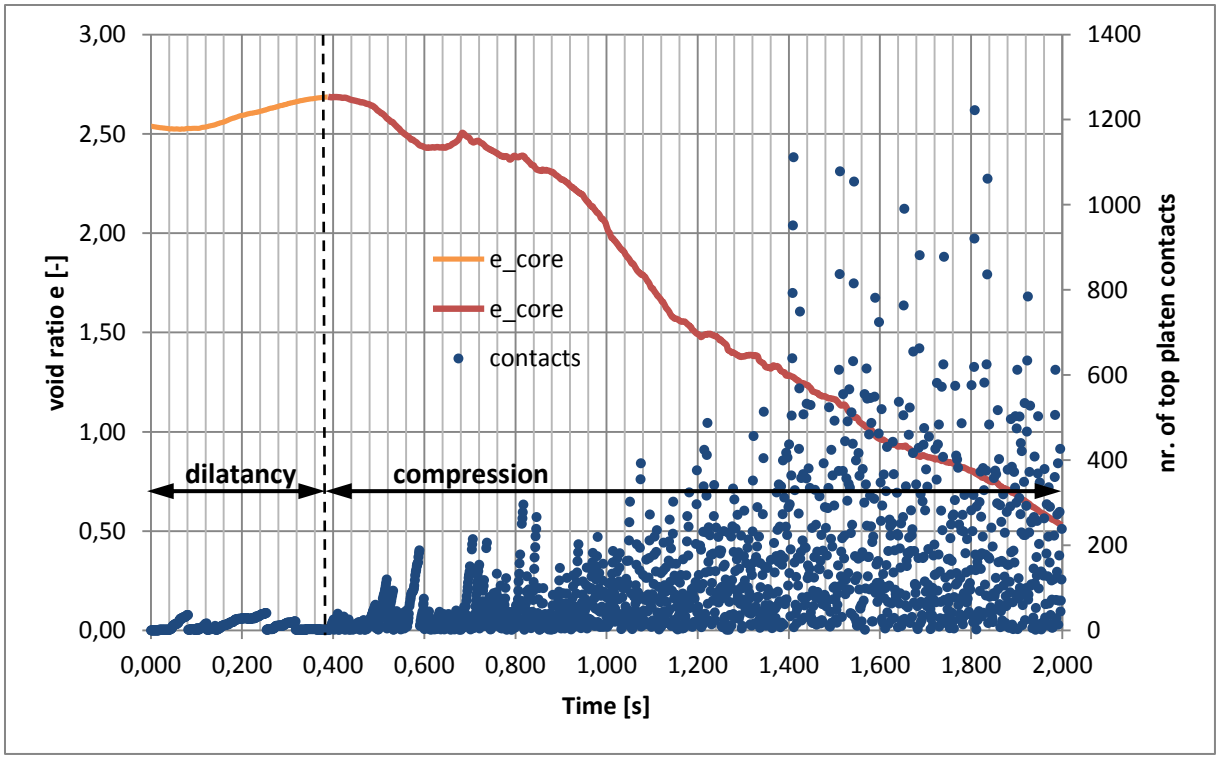


43. Fig. Core void ratio and top platen contacts of the loose specimen with a single grain trapped on top

It can be seen on 43. Fig. that before the transition from dilatancy to compression, the number of contacts stays very low, and shows a steady increase afterwards. 44. Fig. shows the compression curves for the same specimen. The parts of the void ratio plots on the dilatancy branch are shown in orange. This way, the spurious initial parts of the compression curves are distinguished from the regular parts.

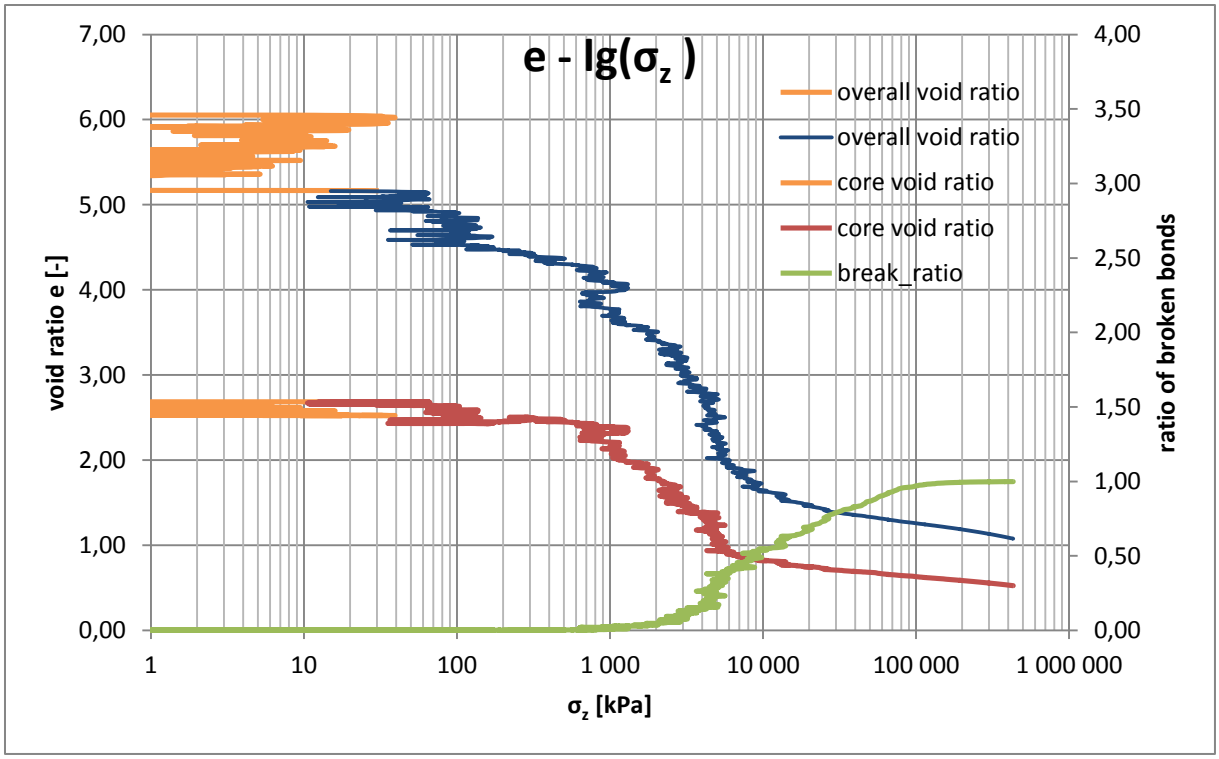


44. Fig.: Compression curves of the loose specimen with a single grain trapped on top

For the dense specimen, where the gap below the top platen was filled manually, the dilatancy was negligible. Therefore the decision was made to discard the initial, "penetration" part of the compression curves from the evaluation of the results.

## 5.2 Contact force distributions

An interesting aspect of the compression test was the distribution of contact forces. To investigate this, some characteristic points were selected along the compression curve of the dense specimen consisting of "reference" grains. These points are shown in 45. Fig., with the main characteristics listed in 15. Table. Here, only those contact forces were regarded, where a parallel bond was not present in the contact, i.e. mainly between different macrograins and fragments. (Contact forces in cracks inside the grains are also contained. – *The solution for this drawback is currently in development.*)

The contact force histograms are presented in 46. Fig. - 52. Fig., on a logarithmic horizontal axis. It is noteworthy that all the histograms are self-similar. During the "elastic stiffening" phase – Points 1-3 – , the histogram's peak moves to the right, which indicates an overall increase in contact forces. However, following clastic yielding between Points 3-5, the histograms "stay in place", meaning that both magnitude and distribution of the contact forces stays constant. After clastic hardening, Points 5-6, the contact forces increase again, shifting the histogram to the right, see 52. Fig.

(Marketos & Bolton, 2007) also found self-similar contact force distributions, in a model without grain crushing. Their shape was different to those presented here, but there are significant differences not only in grain geometry, but also in the applied material/contact models.

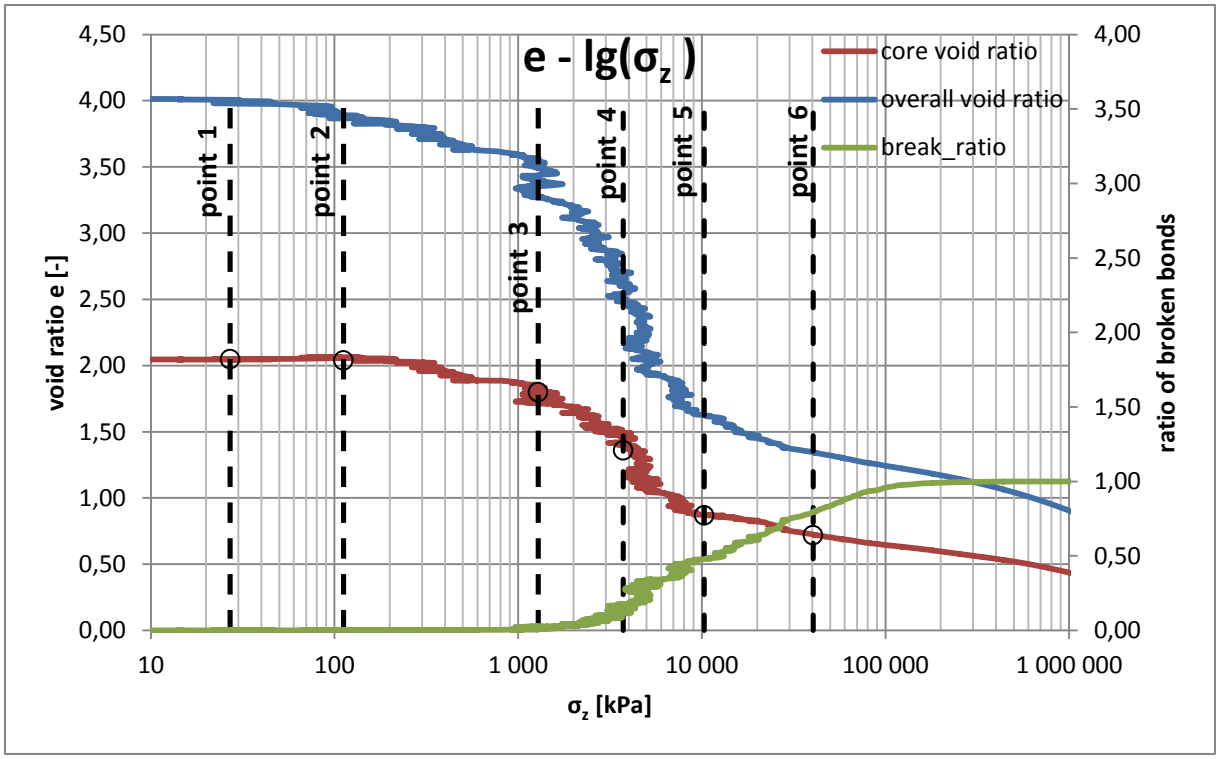


45. Fig.: selected points along the compression curve of the dense specimen, with "reference" macrograins

15. Table: selected points along the compression curve, with main characteristics

| **Point** | **1** | **2** | **3** | **4** | **5** | **6** |
|---|---|---|---|---|---|---|
| At end of loadstep nr. | 2 | 6 | 15 | 41 | 62 | 69 |
| $\sigma_z$ [kPa] | 27 | 112 | 1 286 | 3 733 | 10 304 | 40 412 |
| Core void ratio [-] | 2.05 | 2.03 | 1.80 | 1.36 | 0.87 | 0.72 |
| Ratio of broken bonds [%] | 0.014 | 0.077 | 1.35 | 18.5 | 48.4 | 80.3 |
| Nr. of contact forces | 567 | 720 | 1 811 | 5 582 | 21 057 | 48 630 |
| Mode of distribution [N] | 0.02 | 0.65 | 5 | 3.5 | 4 | 10 |
| Figure Nr. | 46. Fig. | 47. Fig. | 48. Fig. | 49. Fig. | 50. Fig. | 51. Fig. |

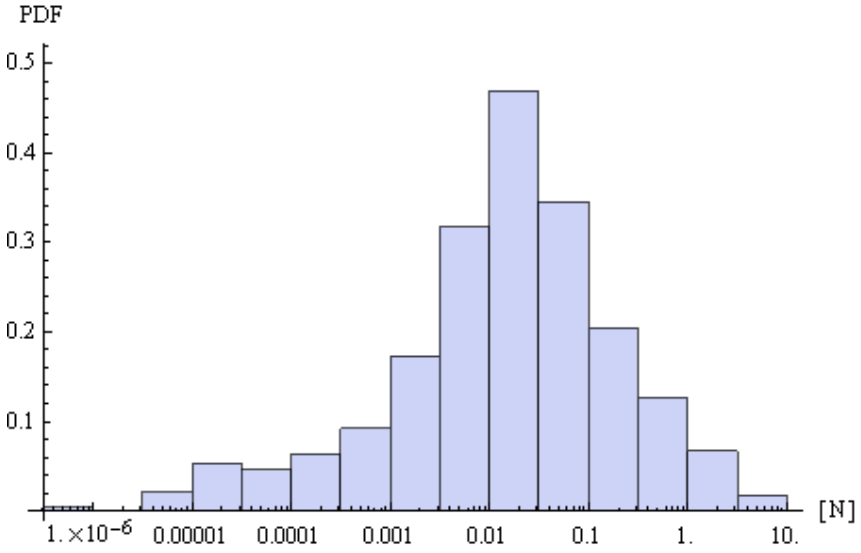


46. Fig.: Contact force histogram at Point 1.

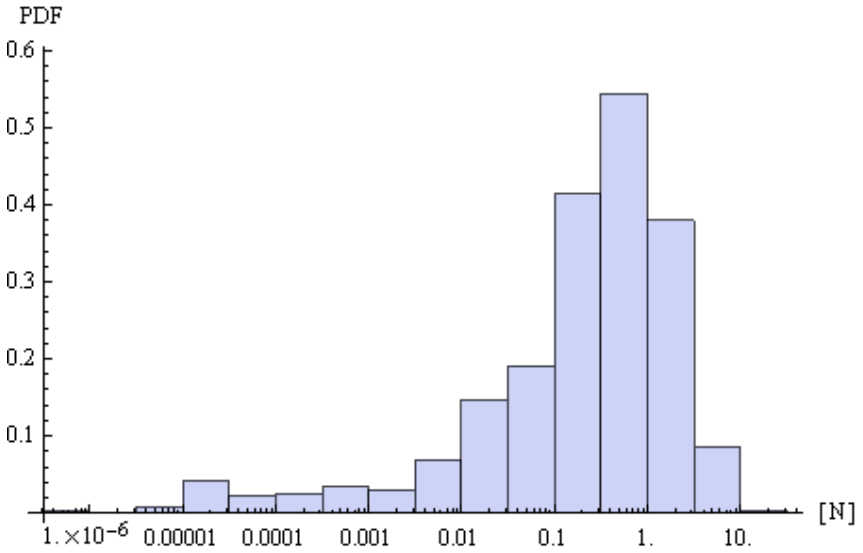


47. Fig.: Contact force histogram at Point 2.

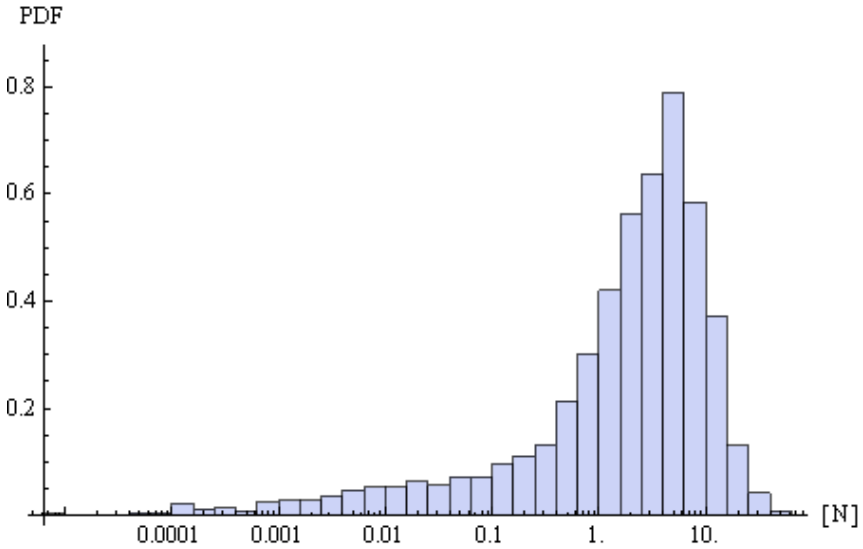


48. Fig.: Contact force histogram at Point 3.

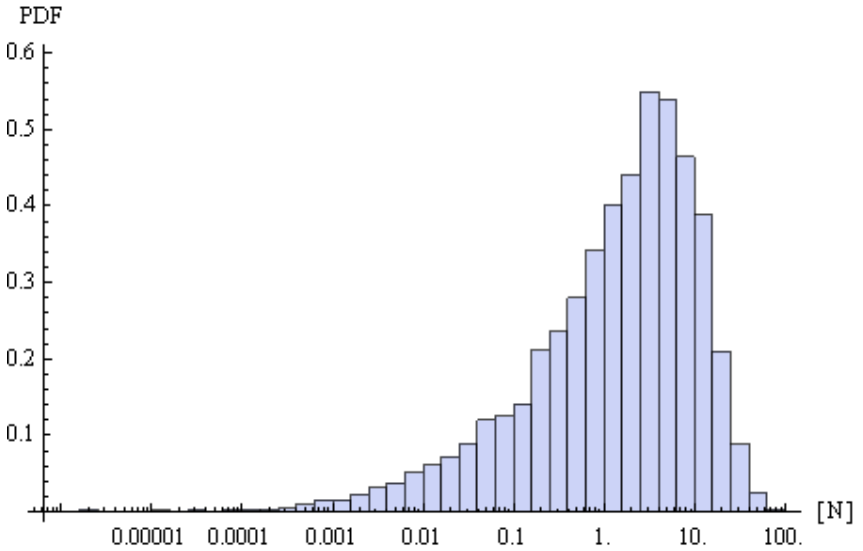


49. Fig.: Contact force histogram at Point 4.

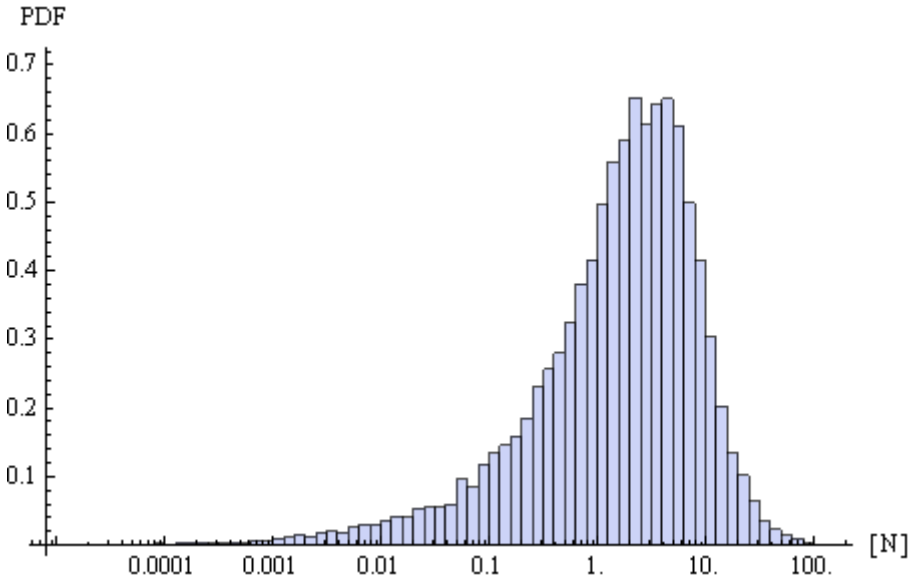


50. Fig.: Contact force histogram at Point 5.

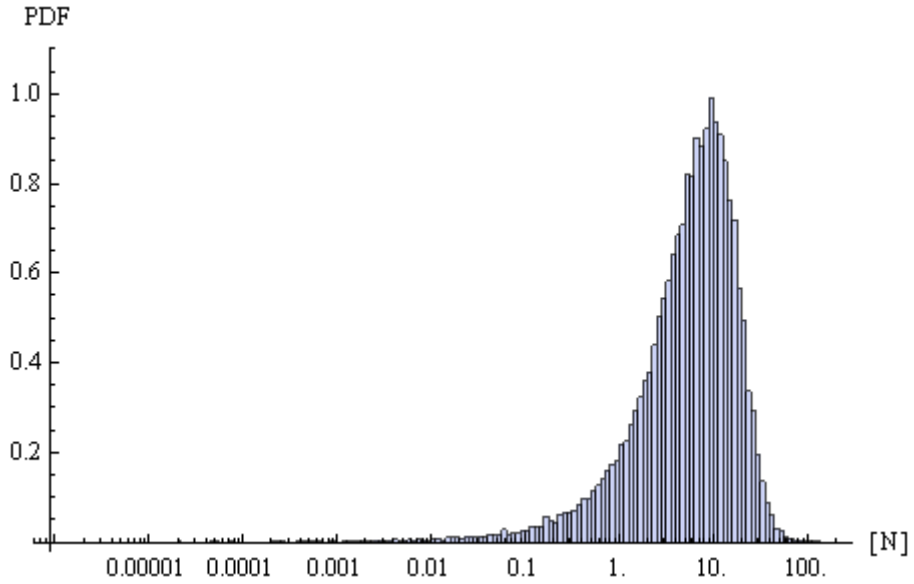


51. Fig.: Contact force histogram at Point 6.

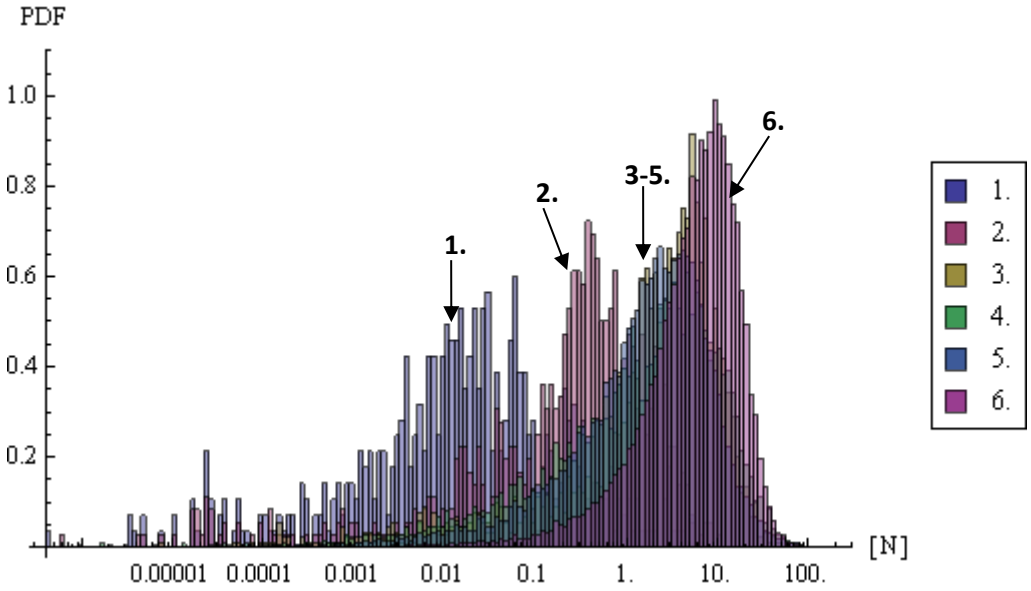


52. Fig.: Contact force histograms at Points 1-6.

## 5.3 Grain size distribution

One of the toughest tasks in real compression tests is to track the evolution of the grain size distribution (GSD): for sieving, the sample is disintegrated, and if the compression test is continued after refilling the grains into the oedometer, the test conditions are different. One major advantage of the DEM is that information about the sample – including the GSD – may be gathered in "real time", without disturbing the compression process.

For tracking the grain size distribution during the compression phase, we have developed an algorithm that identifies particle clusters – that is groups of micrograins that are connected by parallel bonds. That enables the identification of intact macrograins, as well as detached fragments.

After the cluster identification is complete, the grain diameter can be assigned to the particular cluster. The choice of a suitable diameter is not quite straightforward, and many different approaches are known in the literature. The main difficulty is to assign a single number (the grain diameter) to a 3-dimensional body, to capture both its size and shape. Since the fragments in the oedometer model are expected to deviate strongly from a spherical shape, the following – simplified – approach was applied to calculate the grain diameter:

$$D = \sqrt[3]{d_x \cdot d_y \cdot d_z} \qquad (9)$$

where $d_x$, $d_y$ and $d_z$ are the lengths of the particle along the x, y and z axes, respectively. Since the initial macrograins aren't completely round, their diameters will show a slight variation according to Eq. (9). Therefore the calculated grain size distributions will not produce a complete match even for the initial and the limiting GSDs.

The grain size distributions were recorded for Points 1-6 along the compression curve for the dense specimen with "reference" macrograins. The grain size distributions are shown in 53. Fig., while the positions of Points 1-6 are displayed in 45. Fig. The number of individual grains and fragments is given in 16. Table.

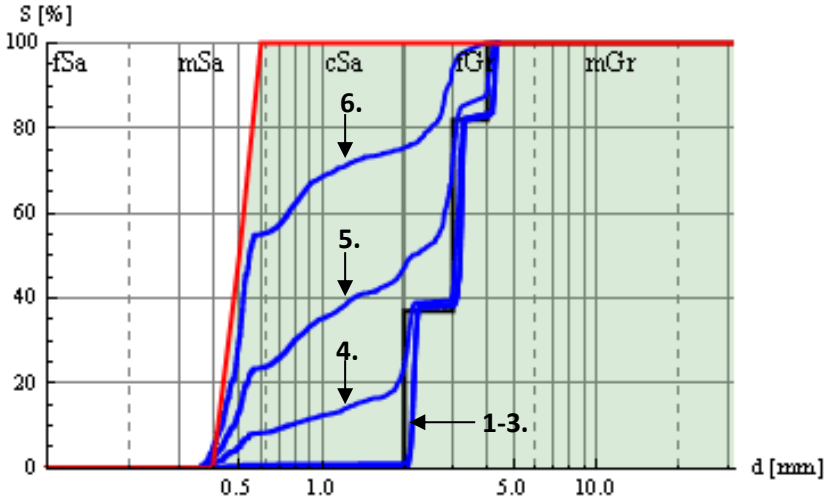


53. Fig.: Grain size distributions for the dense specimen with „reference" macrograins

In 53. Fig., the calculated initial grain size distribution is represented by the black curve, while the limiting grain size distribution of the micrograins is shown in red. The blue curves represent the GSDs from the model, calculated by Eq. (9). As it can be expected from the ratio of broken bonds in 45. Fig., there is no significant change in the GSD up to Point 3. After clastic yielding, the GSD approaches the limiting distributions, and – as expected – the smaller grains are crushed first, and the larger grains remain intact until higher pressures. Such behaviour was both experienced in real tests (Chuhan, Kjeldstad, Bjørlykke, & Høeg, 2002), and explained by theoretical considerations (McDowell & Bolton, 1998, old.: 674).

During and after clastic hardening, the grain size distribution approaches a limiting distribution. (McDowell, Bolton, & Robertson, 1996) argue that this limiting GSD is a fractal distribution, it was also proved experimentally e.g. by (Nakata, Hyodo, Hyde, Kato, & Murata, 2001) and (Lőrincz, és mtsai., 2005). One major drawback of the current model is that the limiting GSD is given by the size distribution of the micrograins, which is far from fractal, and permits a rather narrow range for possible GSDs. As seen in 53. Fig., the GSDs for Points 4-6 gradually approach this limiting GSD by "climbing up" on it. In contrast, they approach the fractal distribution in real tests by gradually "shifting to the left", while retaining their starting point at S=100%.

16. Table: Number of grains at the characteristic points (Points 1-6) along the compression curves

| **Reference grains, Point** | **1** | **2** | **3** | **4** | **5** | **6** |
|---|---|---|---|---|---|---|
| At end of loadstep nr. | 2 | 6 | 15 | 41 | 62 | 69 |
| $\sigma_z$ [kPa] | 27 | 112 | 1 286 | 3 733 | 10 304 | 40 412 |
| Core void ratio [-] | 2.05 | 2.03 | 1.80 | 1.36 | 0.87 | 0.72 |
| Ratio of broken bonds [%] | 0.014 | 0.077 | 1.35 | 18.5 | 48.4 | 80.3 |
| Nr. of grains | 285 | 313 | 775 | 5007 | 11 610 | 19 179 |
| | | | | | | |
| **Proper size effect, Point** | **1** | **2** | **3** | **4** | **5** | **6** |
| At end of loadstep nr. | 2 | 7 | 24 | 36 | 53 | 68 |
| $\sigma_z$ [kPa] | 18 | 159 | 1 841 | 2 751 | 3 834 | 26 981 |
| Core void ratio [-] | 2.04 | 2.01 | 1.74 | 1.32 | 0.88 | 0.71 |
| Ratio of broken bonds [%] | 1.26 | 9.88 | 20.9 | 30.3 | 47.1 | 85.0 |
| Nr. of grains | 314 | 476 | 2 039 | 4 608 | 8 913 | 19 497 |

It' known that the crushing strength of the individual grains has a major influence on the clastic yield stress. In section 3.5.6 it was found that using the same bond properties (bond strength, ratio of depleted bonds, etc.) for all grain sizes leads to a wrong size effect on grain strength: the smaller grains become weaker instead of getting stronger. (22. Fig.) To reach the proper size effect on strength for the initial grains, 0% of the bonds were depleted for the $D_{macro}$=2mm grains, while 10% and 20% were depleted for the $D_{macro}$=3mm and $D_{macro}$=4mm grains, respectively. (32. Fig.) This results in a proper size effect on strength for the initial grains, but it is not clear how the strength of the fragments evolves. (Probably they get weaker, as in the "reference" case.) The oedometric compression test on the dense specimen, with the latter grains will be referred to as the "proper grain strength /PS" case.

54. Fig. shows the compression curves and the ratio of broken bonds for the "proper grain strength" case. The dotted lines represent the corresponding curves from the compression test on the dense specimen with "reference" grains. The Points 1-6 along the compression curve were chosen similarly to those on 45. Fig. The number of individual grains and fragments is given in 16. Table, along with the main state characteristics of the specimen.

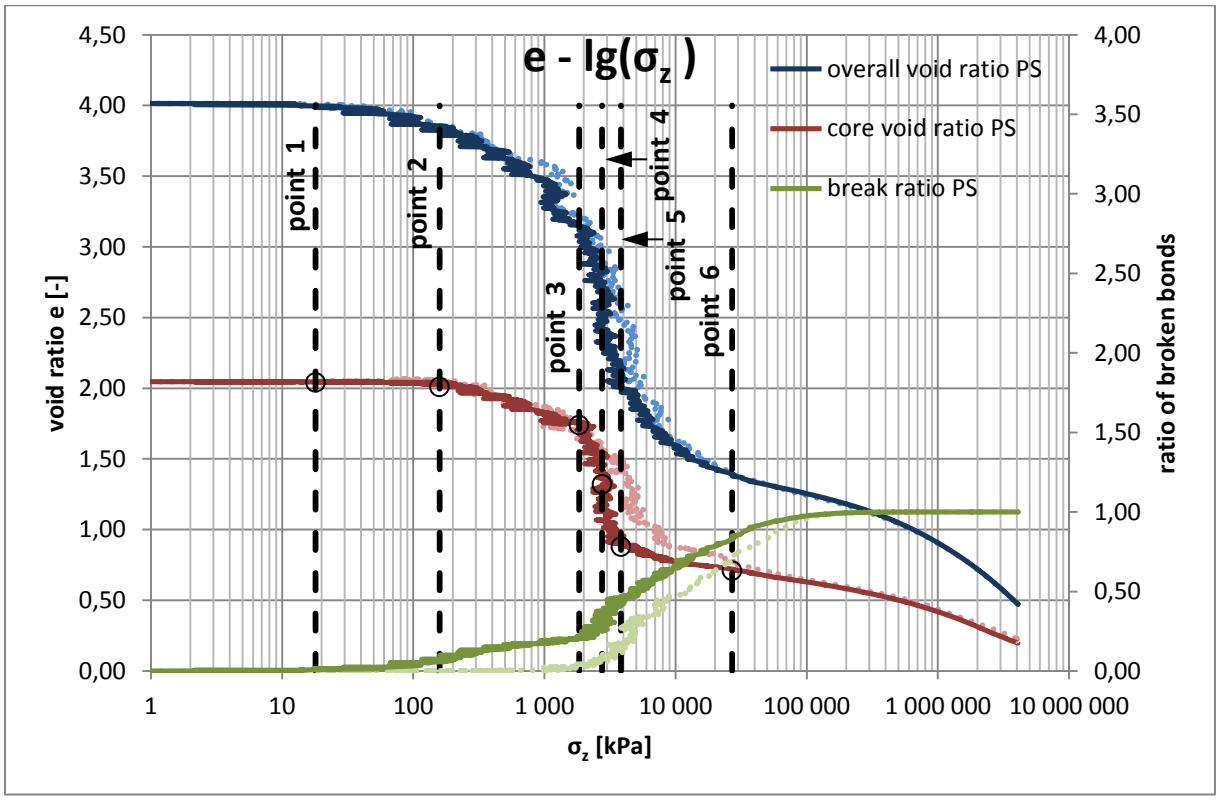


54. Fig.: Compression curves for the dense specimen with „proper grain strength"

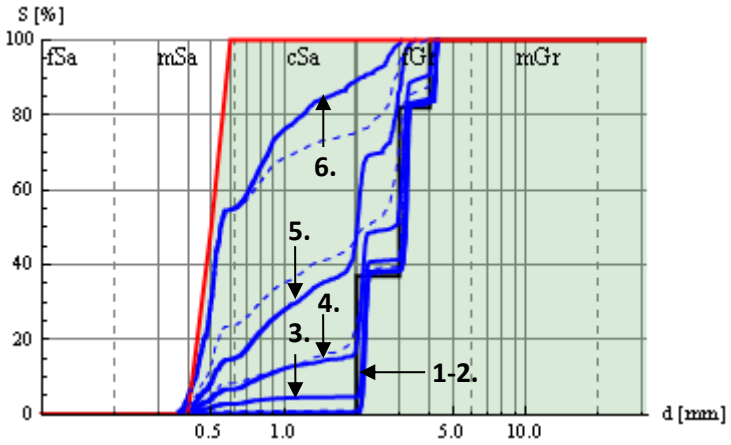


55. Fig.: Grain size distributions for the dense specimen with „proper grain strength"

55. Fig. shows the grain size distributions for Points 1-6 of the "proper grain strength" model. The Corresponding curves from the "reference" model are included as thin, dashed lines. Damage to the grains starts earlier, the GSD at Point 3 already contains some fragments from the $D_{macro}$=2mm and 3mm grains. At Point 4, the damage to $D_{macro}$=3mm grains increases, and 4mm grains also experience damage – in contrast to the "reference" case. At Point 5, some 4mm macrograins are still intact, but the majority of the grains have undergone some splitting. Finally, at Point 6, the only difference between the "reference" and the "proper grain strength" cases is the damage to the $D_{macro}$=4mm grains. Generally, the decreasing strength with increasing grain size is also evident from the GSD curves.

## 5.4 Lower and higher bond strength, normal distribution of bond strength

In section 3.4.3 it was found that the crushing strength of the individual macrograins is almost linearly dependent on the strength of the parallel bonds. Compression tests were also conducted on the dense specimen, with grains of double and half bond strengths, given in 6. Table. The compression curves are shown in 56. Fig., where "ref" denotes "reference" parallel bond strength, while HS and LS stand for "high bond strength" and "low bond strength", respectively.

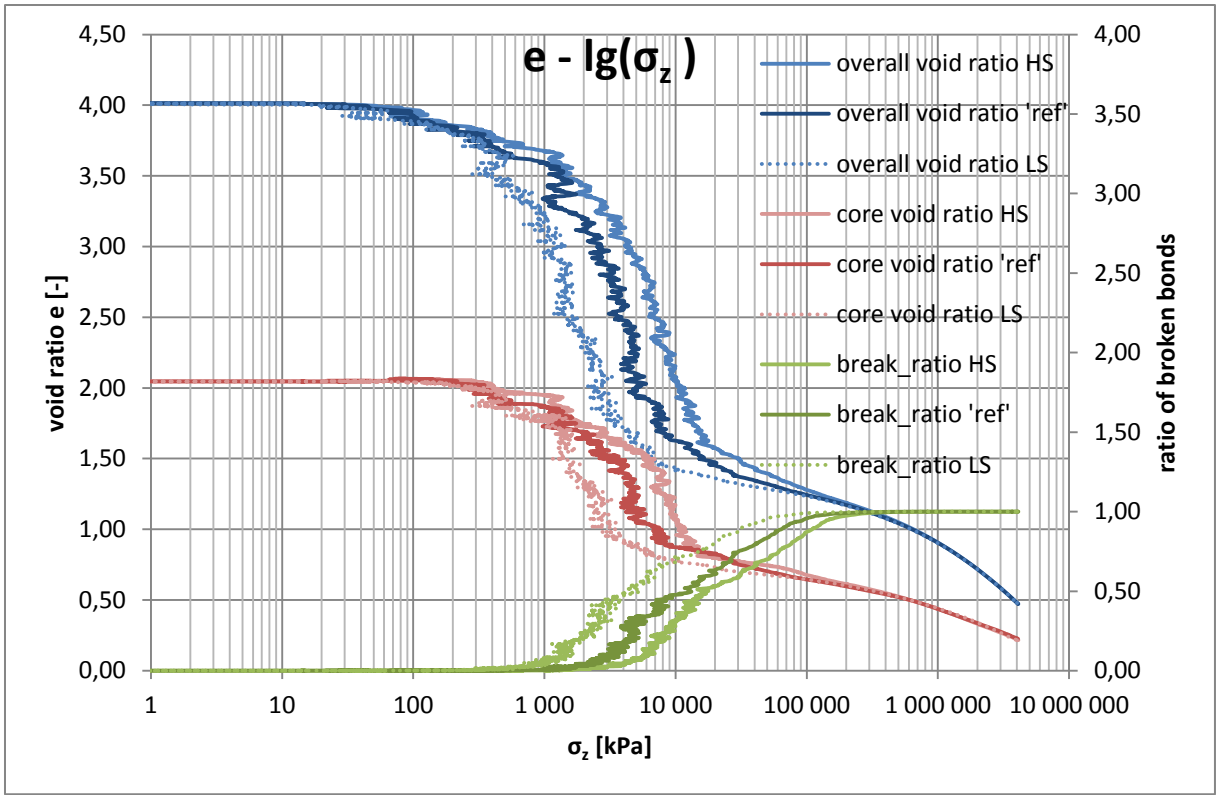


56. Fig.: Compression curves for the dense specimen, with grains of reference, high and low bond strengths

The compression curves reflect the relation of the grain strengths: the “clastic hardening” parts of the curves are practically parallel, and the vertical stress for a given void ratio (overall or core) approximately follows the relation of grain strengths, i.e. it is approx. one half for the LS specimen and the double for the HS specimen, compared to the “reference” grains. The linearity is less clear due to considerable oscillation of the curves, caused by stress relaxation. This applies for the clastic yield stress as well, a smoothing procedure (e.g. fitting Bauer’s compression law) would provide clearer results. The initial parts – without grain crushing – are the same, and the 3 curves asymptotically approach the same limiting compression curve.

The normal distribution of bond strengths was already examined at the level of single macrograin crushing tests in section 3.4.1, and it has been continued on the oedometric compression test-level. Normal distributions with ν=0.25 and ν=0.50 were applied to the bond strengths, to be compared with the ν=0 (uniform strengths, reference) case. The procedure is presented in detail in section 3.4.1. The compression tests with the normally distributed bond strengths were carried out on both the loose and the dense specimen. The compression curves are shown in 57. Fig. - 59. Fig.

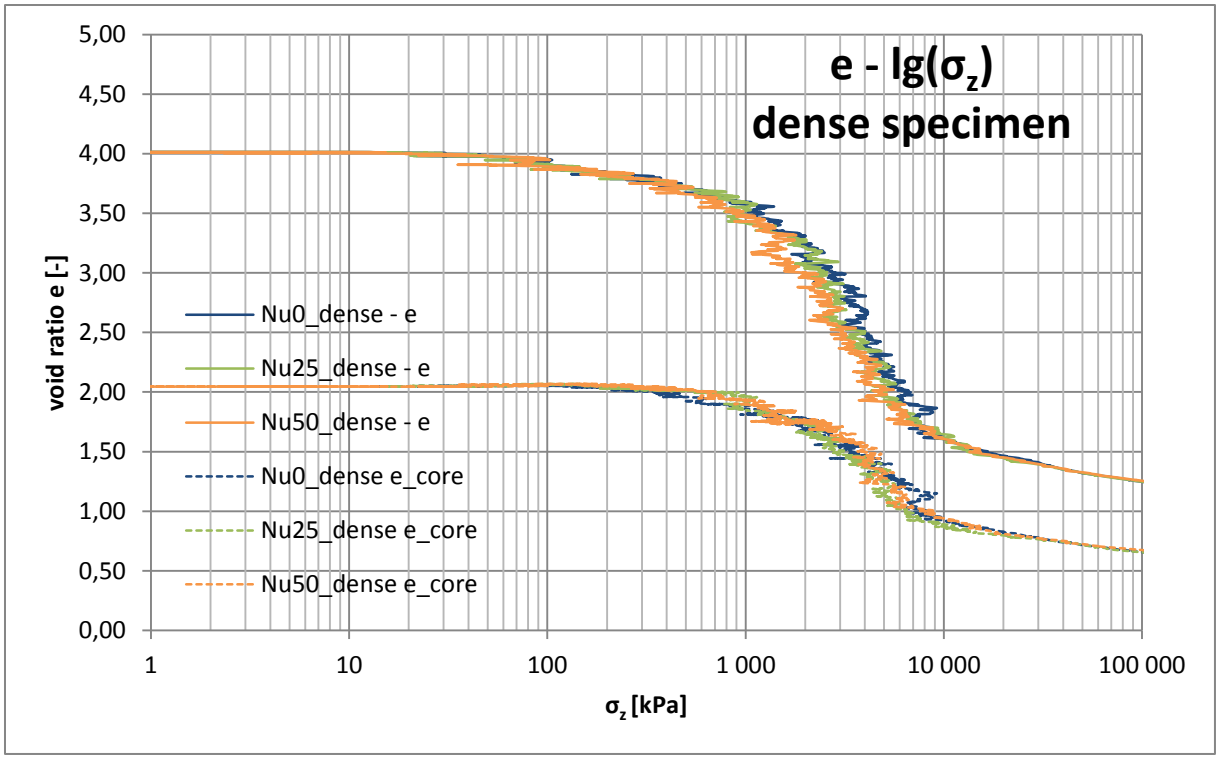


57. Fig.: Compression curves for the dense specimen, v=0.25, v=0.25, v=0.50

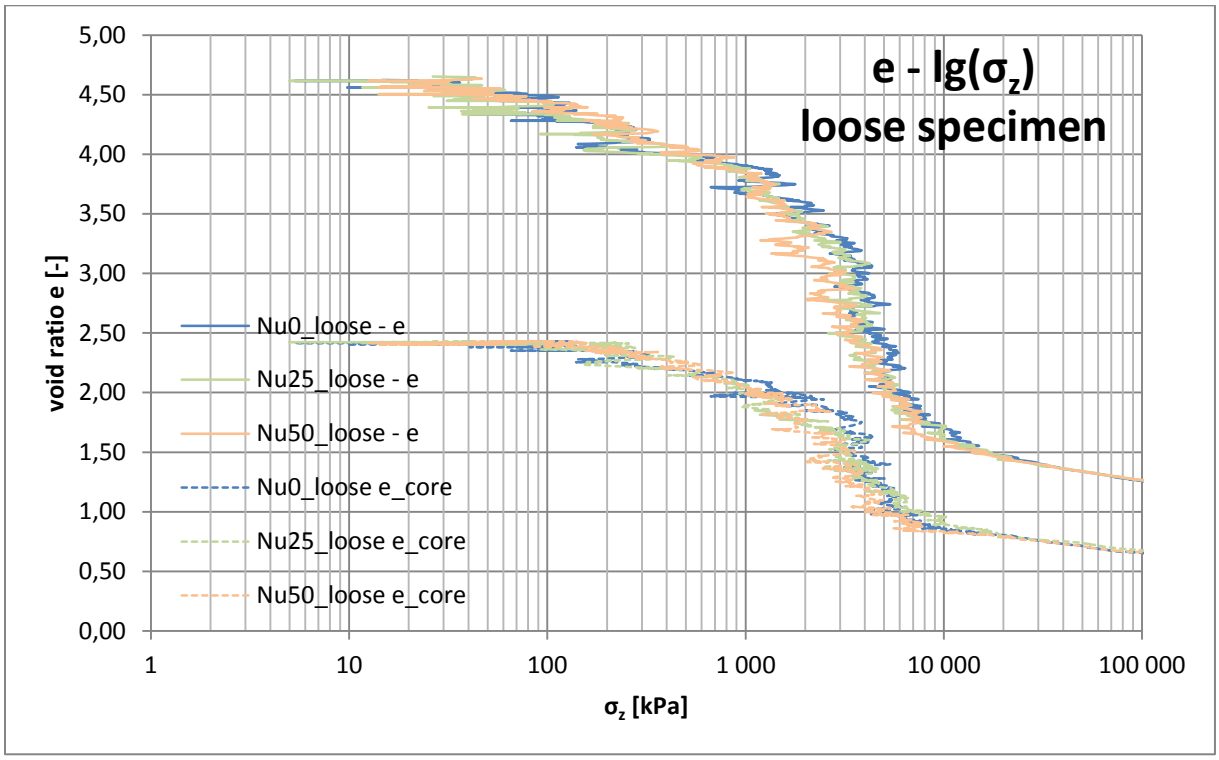


58. Fig.: Compression curves for the loose specimen, v=0.25, v=0.25, v=0.50

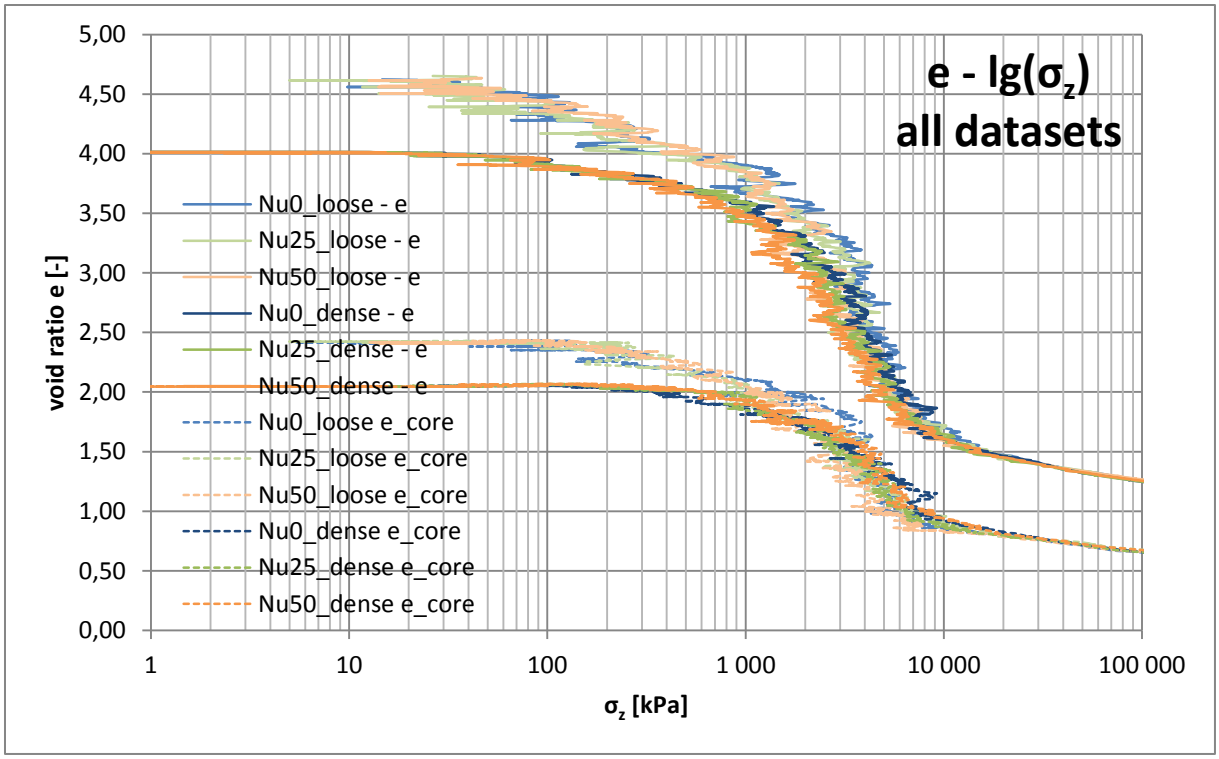


59. Fig.: Compression curves of the "normal distribution" tests , v=0.25, v=0.25, v=0.50

When examining the datasets for the loose and the dense specimen separately, it can be seen that the compression curves share the same trace before clastic yielding and after the clastic hardening part. It was seen in section 3.4.1 that the normal distribution of bond strengths decreases the mean grain strength, the drop is roughly equal to the coefficient of variation v. The same trend may be observed in 57. Fig. and 58. Fig.: the clastic hardening parts of the compression curves are parallel (share the same slope), but are shifted along the horizontal axis. They appear in ascending order with ascending mean grain strength. Although the curves show considerable oscillation, the trend is obvious both for the loose and the dense specimen.

59. Fig. shows that the corresponding curves of the dense and loose specimen converge after clastic hardening, sharing the same limiting compression curve. Furthermore the slope of the clastic hardening part is steeper for higher initial void ratios.

Similar results were obtained e.g. by (Nakata, Kato, Hyodo, Hyde, & Murata, 2001) in oedometric tests and by (Uygar & Doven, 2006) in cyclic triaxial tests on sand.

## 5.5 Lateral stresses

The lateral stresses – both $\sigma_x$ and $\sigma_y$ – were recorded throughout the compression phase for each specimen. It has been found that – within a small margin – $\sigma_x = \sigma_y$, and they are linearly dependent on $\sigma_z$. Hence the relation

$$\sigma_x = \sigma_y = K_0 \cdot \sigma_z \qquad (10)$$

applies, where $K_0$ is the well-known at-rest earth pressure coefficient, it can be estimated as the slope of the $\sigma_x(\sigma_z)$ plot. For the dense and loose specimen with "reference" grains, these are shown in 60. Fig. and 61. Fig. With linear regression, the following values were derived for the lateral stress coefficient: $K_0$=0.42 for the dense specimen, and $K_0$=0.46 for the loose specimen. Both curves are

bilinear, with the slight kink around 70 000 kPa. Notwithstanding this slight deviation from linearity, the coefficients of determination was $R^2$>0.995 for each linear regression.

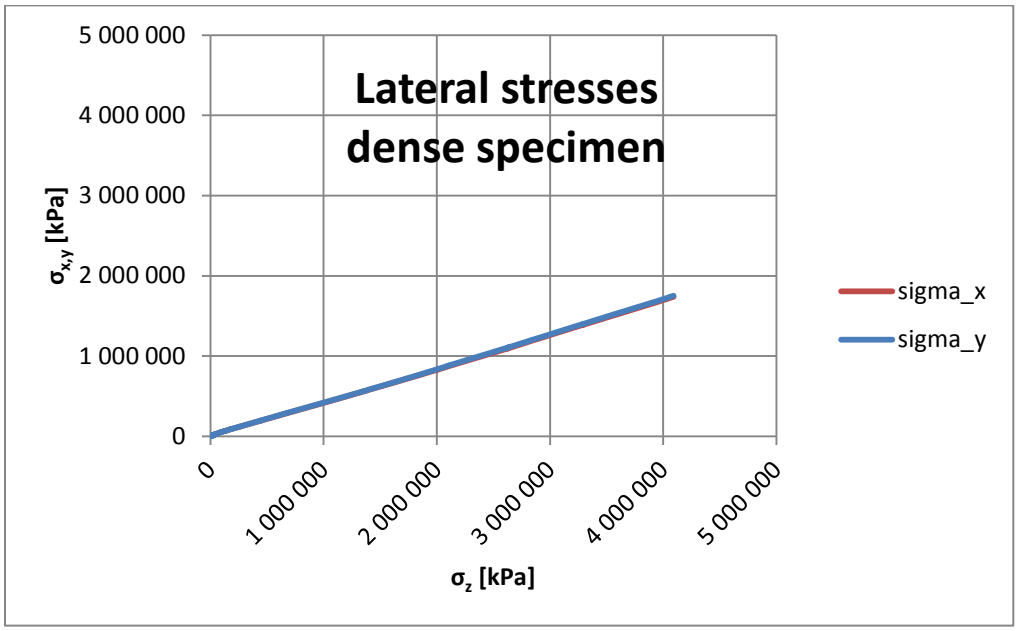


60. Fig.: Lateral stresses against vertical stress, for the dense specimen with reference macrograins

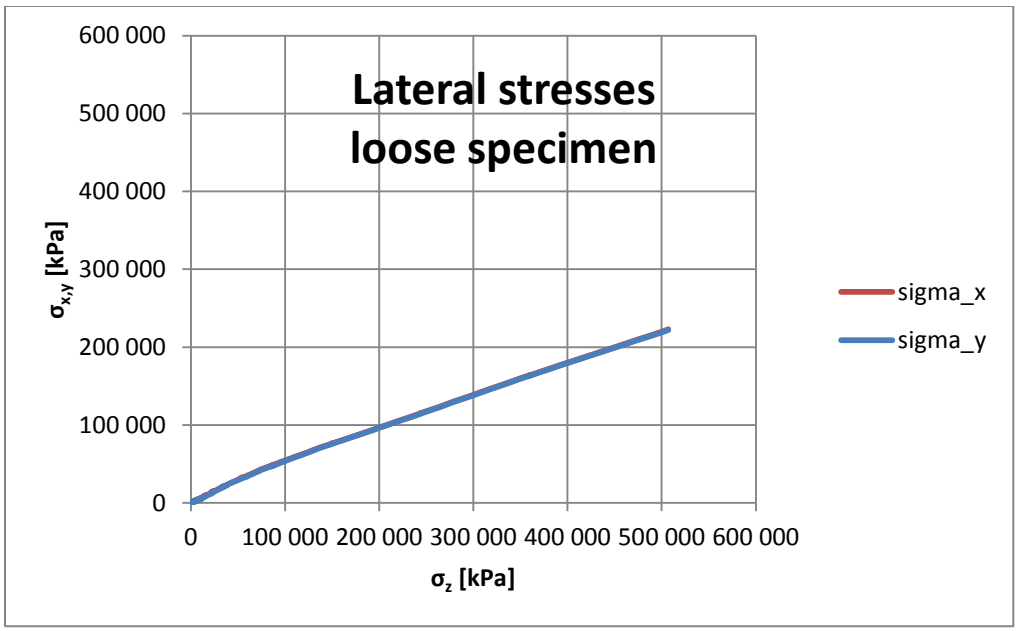


61. Fig.: Lateral stresses against vertical stress, for the loose specimen with reference macrograins

Given the linear relationship between vertical and lateral stresses, the stress argument $3p_s$ in Bauer's compression law may be expressed as

$$3 \cdot p_s = \sigma_x + \sigma_y + \sigma_z = (1 + 2 \cdot K_0) \cdot \sigma_z \qquad (11)$$

That means that the difference between the e-lg($\sigma_z$) and the e-lg($3p_s$) compression curves is only a shift along the horizontal axis by ($1+2K_0$). 62. Fig.

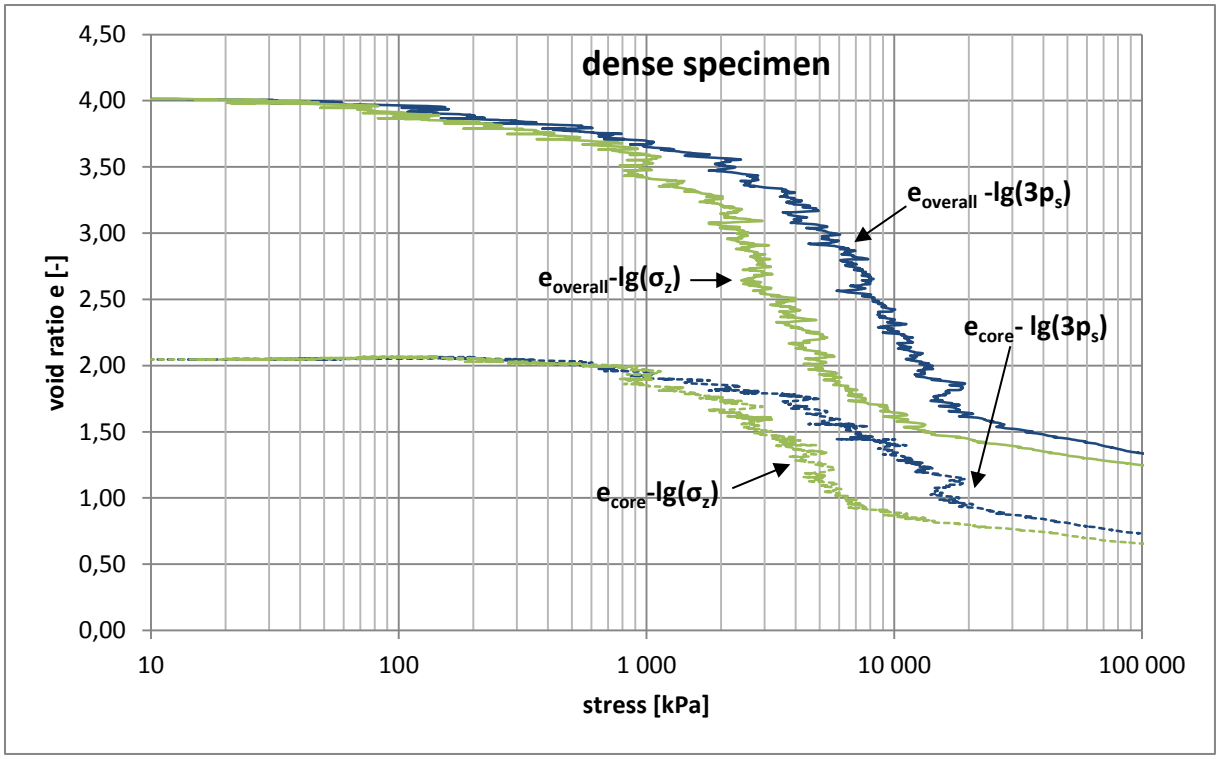


62. Fig.: Compression curves for the dense specimen, void ratio against $\sigma_z$ and $3p_s$